2011

PHOTOIONIZATION STUDIES OF O2 AND H2

Arathi Padmanabhan
University of Windsor

PHOTOIONIZATION STUDIES OF O_2 and H_2

By
Arathi Padmanabhan

A Dissertation
submitted to the Faculty of Graduate Studies
through the Department of Physics
in Partial Fulfillment of the Requirements for
the Degree of Doctor of Philosophy at the
University of Windsor

Windsor, Ontario, Canada
2011

Declaration of Co-Authorship / Previous Publication

I. Co-Authorship Declaration

I hereby declare that this thesis incorporates material that is result of joint research, as follows:
The concept and design of experiments in Chapter 4 and 5 were original ideas of the author. Data acquisition and subsequent data analysis of the experiments were performed by the author. Theoretical aspects of photoionization study of H_2 presented in Chapter 5 were results of collaboration with Drs. J. Fernández, A. Palacios and F. Martín. Portion of the data analysis software in Chapter 5 was written by Dr. Peter Hammond. The experimental work in this thesis was conducted at the Canadian Light Source (CLS), Saskatoon and the experimental work is the outcome of collaboration with Drs. Mike MacDonald and Lucia Zuin of CLS. Details on the spectrometer design, operational modes and data acquisition software presented in Chapter 2 and 3 are the work of Dr. Timothy J. Reddish and his graduate students prior to my start date of September 2007. The spectrometer was aligned at the VLS PGM beamline and successfully commissioned for experimental work performed in this thesis by the author.

I am aware of the University of Windsor Senate Policy on Authorship and I certify that I have properly acknowledged the contribution of other researchers to my thesis, and have obtained written permission from each of the co-author(s) to include the above material(s) in my thesis.

I certify that, with the above qualification, this thesis, and the research to which it refers, is the product of my own work.

II. Declaration of Previous Publication

This thesis includes two original papers that have been previously published/submitted for publication in peer reviewed journals, as follows:

Thesis Chapter	Publication title/full citation	Publication status
Chapter 4	A. Padmanabhan *et al.*, An angle-resolved dissociative photoionization study of the $c^4\Sigma_u^-$ state in O_2^+ using the TPEPICO technique. *J. Phys. B: At. Mol. Opt. Phys*. **43** (2010) 165204	Published
Chapter 5	T. J. Reddish *et al,* Observation of interference between two distinct autoionizing states in dissociative photoionization of H_2.	Submitted to Physical Review Letters (PRL)

I declare that, to the best of my knowledge, my thesis does not infringe upon anyone's copyright nor violate any proprietary rights and that any ideas, techniques, quotations, or any other material from the work of other people included in my thesis, published or otherwise, are fully acknowledged in accordance with the standard referencing practices. Furthermore, to the extent that I have included copyrighted material that surpasses the bounds of fair dealing within the meaning of the Canada Copyright Act, I certify that I have obtained a written permission from the copyright owner(s) to include such material(s) in my thesis.

I declare that this is a true copy of my thesis, including any final revisions, as approved by my thesis committee and the Graduate Studies office, and that this thesis has not been submitted for a higher degree to any other University or Institution.

ABSTRACT

A toroidal spectrometer designed to perform (γ, 2e) studies, was for the first time employed for Threshold Photoelectron Photoion Coincidence (TPEPICO) study. The angular distributions of $O^+(^4S)$ ions produced from dissociative photoionization (DPI) of O_2^+ $c^4\Sigma_u^-$ (ν=0,1) using the TPEPICO technique, i.e. by measuring the coincidence yield between threshold photoelectrons and photoions have been investigated. The results for lifetimes, τ_v, corresponding to the vibrational levels ν = 0,1, along with the value obtained for inherent anisotropic photoion angular distribution β_{O^+}, are presented.

Recently, Fernández and Martín (*New J Phys* **11** 34 (2009)), have performed an extensive *ab initio* study of DPI in H_2, in which large oscillatory behaviour in the electron angular distribution, as a function of electron energy, has been predicted. The result of their ab anitio calculations reveal that the electron angular, θ, distributions oscillate between a $\cos^2\theta$ pattern and isotropic with less than a 1 eV.change in electron energy Due to the very low cross section and the requirement for high energy resolution in the electron detection system, these measurements require sensitive instrumentation that is now available at the Canadian Light Source. For this particular H_2 study, the electron angular distributions as a function of electron energy are the signature of quantum mechanical interference between, essentially, two specific doubly excited states (namely, $1Q_1{}^1\Sigma_u^+$ and $1Q_2{}^1\Pi_u$) decaying at *different* inter-nuclear distances. While interference between 'direct' photoionization and autoionization is well-known, the first unambiguous observation of interference between two autoionization processes, occurring on the femtosecond timescale is presented.

A simple semi-classical model captures the essence of both our experimental observations and the results of full *ab initio* calculations. It does this through explicitly linking the *electron* angular distributions with the *nuclear* motion of the dissociating diatomic molecule

I dedicate this thesis to
my family

ACKNOWLEDGEMENTS

I would like to thank Dr. Timothy J. Reddish for giving me the opportunity to be a part of his research group and for being a dedicated teacher. I am deeply grateful for his support and guidance throughout. I am honored and grateful to have worked with Dr. Mike MacDonald, I thank him for our successful collaboration and for sharing his knowledge with me. I would like to thank Dr. Lucia Zuin for her warm hospitality in making my Saskatoon visits comfortable. I am also thankful for her expertise on the beamline, which has been instrumental in making every synchrotron run a success. I would like to thank Dr. Peter Hammond for his counsel and encouragement during my PhD and for his timely support during the last synchrotron run. I would like to thank Dr. Penny Thorn for her invaluable contribution during the commissioning of the spectrometer at CLS.

I acknowledge the receipt of support from the CLS Graduate Student Travel Program.

My thanks to Dr. David Tessier for insightful conversations and for sharing his experiences as a graduate student. I would like to thank Michael Sullivan for his assistance during the transport of the spectrometer to Saskatoon and for proof reading this thesis. The graduate student community here has been has been a great pillar of support and in particular I would like to thank: Paul Moffatt, Behnam Javanparast, Ghazal Ghodsi, Michael Sullivan and Theresa Spanjers. I am thankful to all the faculty and staff members of Department of Physics at the University of Windsor for their support and encouragement.

I am immensely grateful to my parents R. A. Padmanabhan and Rajalakshmi Padmanabhan for all their support and relentless encouragement. My special thanks to Suma for her friendship and for being a constant source of support. Thanks to my brother Anand for his encouragement and moral support. I would like to thank my in laws Mr and Mrs. Ramaswamy and my extended family for all their support. My husband Karthik, who has showered me with unconditional support and without whom this would have been an impossible dream, thank you for everything.

TABLE OF CONTENTS

CHAPTER 3: DATA ACQUISITION AND PROCESSING

CHAPTER 4: PHOTOIONIZATION STUDIES OF O_2

CHAPTER 5: DISSOCIATIVE PHOTOIONIZATION STUDIES OF H_2

LIST OF TABLES

LIST OF FIGURES

CHAPTER 1 - THIRD GENERATION LIGHT SOURCE

1.1 INTRODUCTION

1.2 THIRD GENERATION SYNCHROTRON RADIATION

1.2.1 SYNCHROTRON RADIATION

1.2.2 CANADIAN LIGHT SOURCE – A THIRD GENERATION SYNCHROTRON

1.2.3 INSERTION DEVICES

1.3 VLS PGM BEAMLINE

1.4 LINEARLY POLARIZED SYNCHROTRON RADIATION

1.4.1 ELLIPTICAL POLARIZATION

1.4.2 STOKES PARAMETER

1.4.3 PHOTOIONIZATION CROSS SECTION

1.4.4 ANGULAR DISTRIBUTION

1.5 REFERENCES

1.1 INTRODUCTION

The experimental work in this thesis was performed at the VLS PGM (Variable Line Spacing Plane Grating Monochromator) beamline at the Canadian Light Source (CLS) in Saskatoon, SK using linearly polarized light. The VLS-PGM beamline [1] covers soft x-ray energy region of 5.2–250 eV by using three variable line spacing plane gratings. The CLS is a third generation synchrotron facility where the electrons reach upto 2.9 GeV in energy in the booster ring and an injection system transfers the electrons to the storage ring with a diameter of 54.43 m. The improved brightness in this third generation synchrotron facility is achieved by using insertion devices called undulators.

In this chapter, the different stages involved in generating and storing synchrotron light in a third generation light source is presented. Third generation light sources employ insertion devices, such as undulators and wigglers. Insertion devices are present in straight sections of the storage ring. An undulator is the source for the VLS PGM beamline, which operates out of a straight section. Technical details on the operation of VLS PGM along with the optical layout of the beamline are presented. Also presented are Stokes parameters which are a standard set of parameters that characterize electromagnetic radiation in terms of polarization state. In this case, since angular distributions are measured using linearly polarized light, the Stokes parameter for this particular polarization state is given. Subsequently, standard equation used to measure the photoionization cross section from which one can eventually derive the angular distribution is presented.

1.2. THIRD GENERATION SYNCHROTRON RADIATION

1.2.1 SYNCHROTRON RADIATION

When electrons are accelerated close to the speed of light, they produce a forward peaked radiation distribution [2]. The electrons are accelerated in a radio frequency (RF) powered cavity and when moving at relativistic speeds, forward peaked radiation is emitted tangentially to the path of the electrons (much like a search light effect-Fig 1 a).

The force in the RF cavity is given by the Lorentz Force $\vec{F} = q\vec{E} + q\left(\vec{v} \times \vec{B}\right)$. Here q is the charge of the electron, $\vec{E}$ is the electric field, $\vec{B}$ is the magnetic field and $\vec{v}$ is the velocity of the relativistic electrons. The force $\vec{F} = \frac{d\vec{p}}{dt}$; where the relativistic momentum $\vec{p} = \gamma m\vec{v}$ and the Lorentz transformation in the laboratory frame of reference is given by $\gamma = \frac{1}{\sqrt{1 - \frac{v^2}{c^2}}}$. Electric fields are used to accelerate the electrons and magnetic fields to maintain and control the trajectory of the electrons. Magnetic fields produced by using dipole magnets cause the electrons to experience centripetal acceleration and the electrons when accelerated in a circular path at high speed produce electromagnetic radiation(as seen in Fig 1 a).

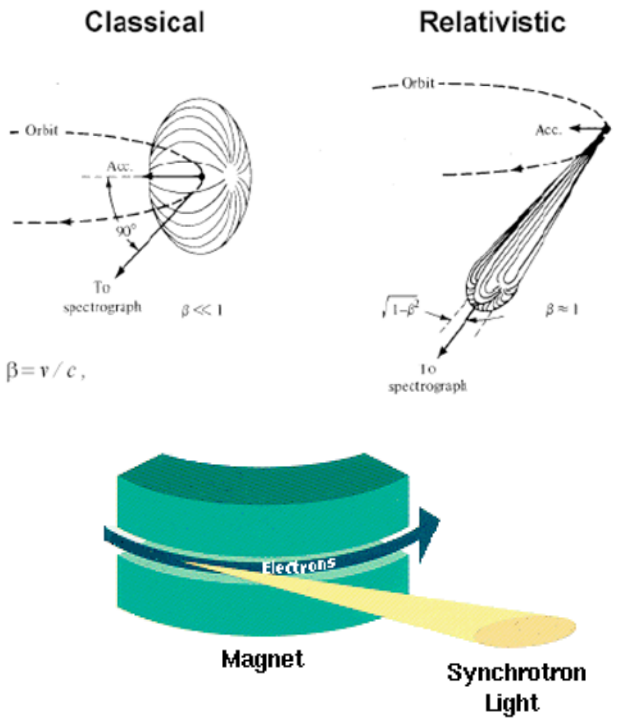

Fig 1 a (Top): Emission pattern of an electron circulating with a classical velocity v ($v/c << 1$) and relativistic velocity ($v/c \approx 1$) (Bottom) Schematic of a dipole magnet or a bending magnet that changes the direction of the electrons, resulting in a forward peaked radiation.

1.2.2 CANADIAN LIGHT SOURCE – A THIRD GENERATION SYNCHROTRON

Linearly polarized (100%) synchrotron radiation was the photon source for all the photoionization experiments presented in this thesis conducted at the CLS synchrotron facility. The synchrotron operation can be designated to four sections as seen in Fig 1 b [3].

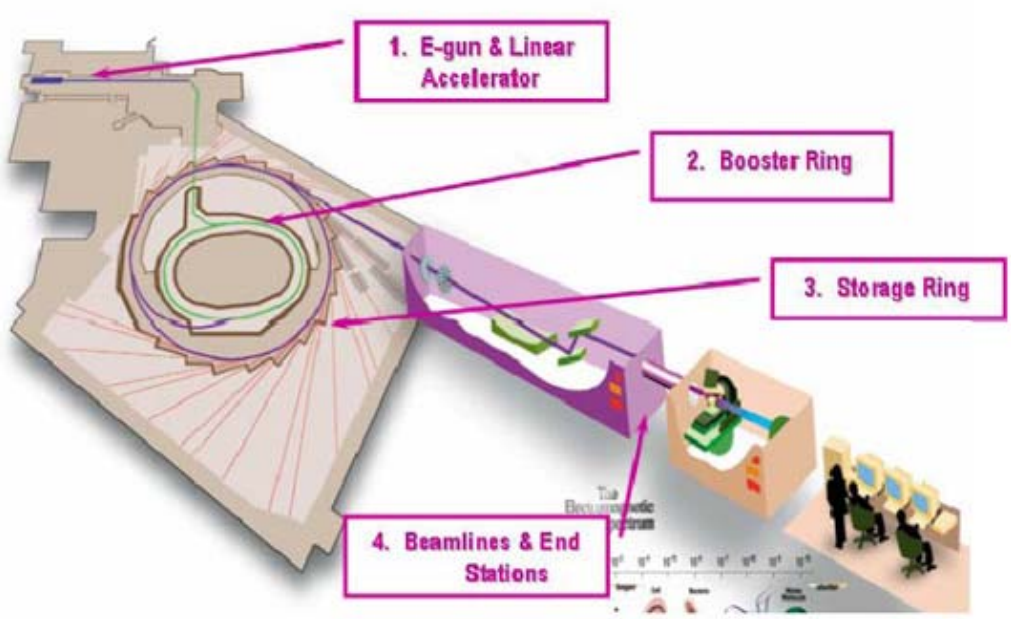

Fig 1 b: Schematic of the CLS synchrotron operation from generation of electrons to the end stations. [Picture Courtesy: Canadian Light Source]

1. Firstly, an electron gun supplies electrons to the Linear Accelerator (LINAC). The LINAC is a radio frequency (RF) cavity where microwave RF fields (2856 MHz) accelerate the electrons to an energy of 250 MeV. At this energy the electrons are travelling at 99.9998% of the speed of light. The LINAC produces electrons in pulses from 2 ns up to 140 ns for injection into the storage ring. The short pulses of electrons can be used to fill a single "bunch" in the storage ring and are used in time-sensitive measurement studies. The long pulses (multi-bunch) are used to produce a (3x140=) 420 ns pulse train in the storage ring.

Electrons are supplied once per second by the LINAC. Once sufficient current is accumulated in the storage ring and the LINAC is turned off until it is required to refill the ring typically 8-12 hours later.

2. The electrons are then directed to a "booster" ring which is again an RF cavity where the microwave fields (~2856 MHz) boost the electron energy from 250 MeV to 2900 MeV. There are two types of electro-magnets in the booster ring. In Fig 1 c, there is the dipole magnet (blue colored) where the magnetic field created by the magnets is used to direct the electrons around the booster ring. Then, there are quadrupole magnets (green colored) whose fields are used to focus the bunches of electrons into a fine beam within the ultra high vacuum chamber.

Fig 1 c: Bending magnets are blue colored dipole magnets that are used to guide the electrons around the ring and the green quadrupole magnets are used to force the electron bunches into a fine beam. [Picture Courtesy: Canadian Light Source]

3. When the electrons reach high energy of 2900 GeV they are then transferred to the storage ring via an injection system. The electrons in the storage ring will circulate for eight to twelve hours, and as they accelerate around the ring with relativistic velocities, they emit radiation on a tangent. The storage "ring" is a series of 12 straight sections each with 2 dipole magnets, and a series of quadrupole and sextupole magnets to control and narrow the electron beam. The photons exit at tangential points to the ring and specially built photon ports allow light to be guided down to each beamline (as seen in Fig 1 d). Over time, the number of electrons stored in the ring will decline, as with time the electrons will collide with the residual gas that are present and will be lost. As a result, the ring is then emptied and re-injected with electrons, or more electrons are added to maintain the necessary circulating current.

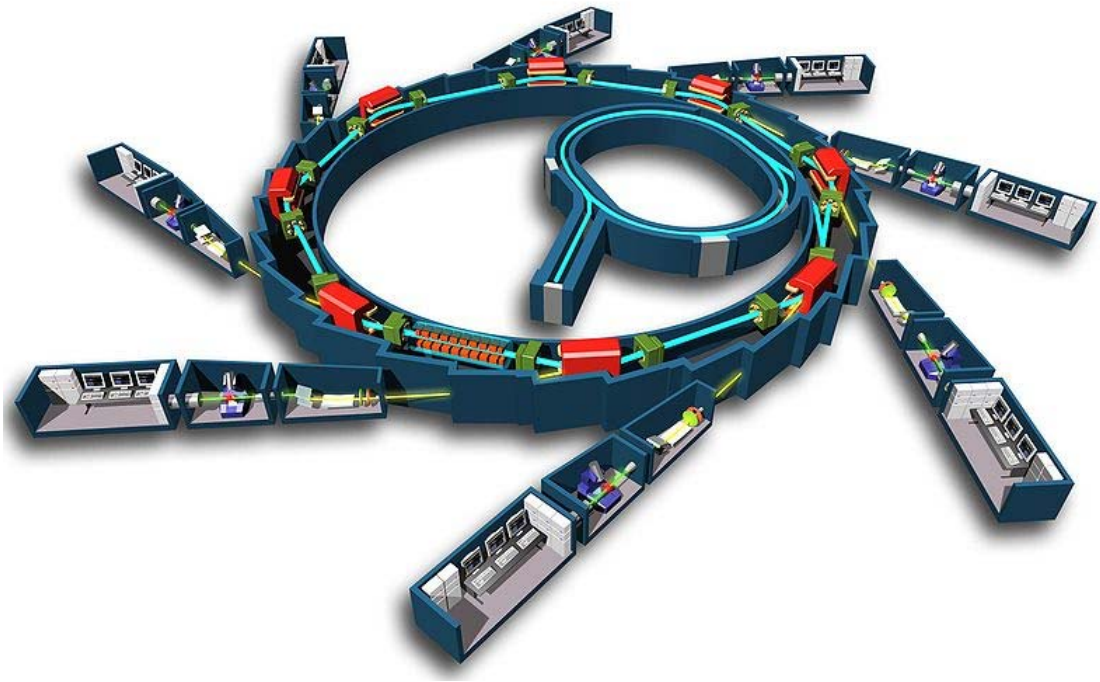

Fig 1 d: Synchrotron layout scheme of Soleil, a third generation synchrotron facility in France, showing the beamlines branching out at tangential points to the ring.

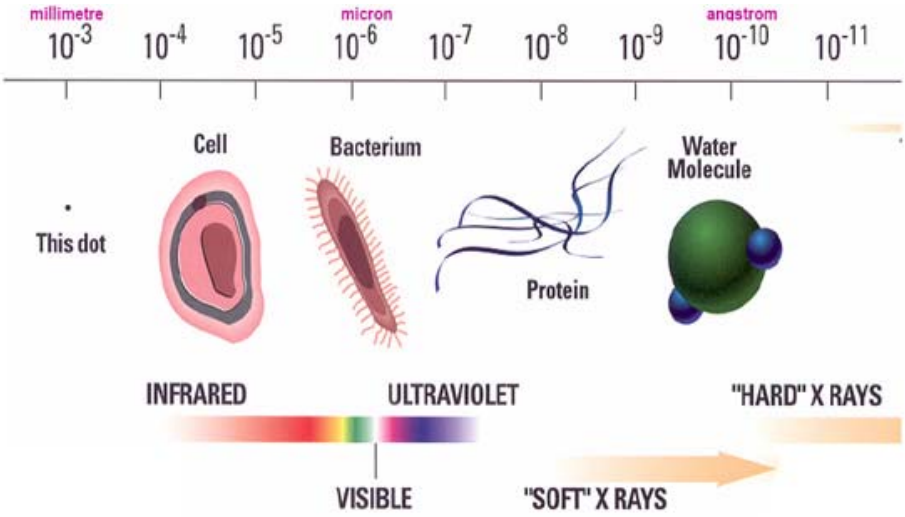

Fig 1 e: The electromagnetic spectrum, going from higher wavelength (far left) to shorter wavelength (far right). The wavelength of light used by a synchrotron scientist correlates to the size of the matter that is of research interest.

4. Each beamline at CLS uses a different monochromator that has a unique energy range and will have markedly different optics specific to their design. Fig 1 e shows the wavelength ranges in the electromagnetic spectrum that relate to the size of the matter that applies to one's research. The synchrotron light is produced at tangential points to the ring that then passes through a monochromator before reaching the "sample". The monochromator is used to choose the wavelength of light required to conduct a particular experiment. The required wavelength is selected using a monochromator that operates either by the principle of Bragg refraction, or by diffraction gratings. Both methods spatially separate the wavelengths of light and filters out the light that isn't required. The chosen wavelengths of synchrotron light are then optically guided using various planar and focusing mirrors to an experimental endstation.

1.2.3 INSERTION DEVICES

Third generation synchrotrons such as the CLS offer improved brightness and this is achieved by the use of insertion devices. Insertion devices are magnetic devices that are inserted at various places in the storage ring and incorporating these devices leads to the necessity of "straight sections" in the ring. The magnetic fields from the dipole magnets change the directions of the electrons that eventually lead to electromagnetic radiation. Undulators and wigglers are multi-magnet insertion devices that make the light more intense and bright [2].

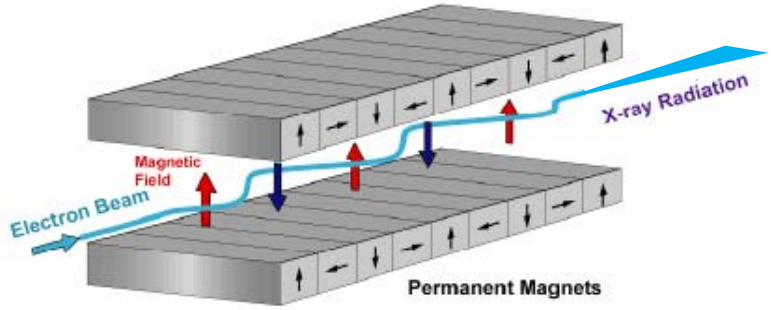

a)

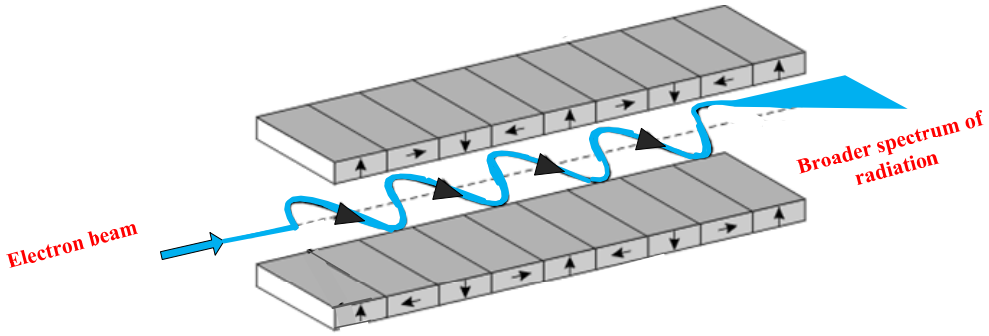

b)

Fig 1 f: Schematics of a) Undulator Magnet, with a narrower/highly collimated beam output b) Wiggler magnet with a wider beam output

Both the undulator and wiggler consist of a series of magnetic devices. In the case of an undulator (Fig 1 f a), electron beam enters into a series of magnets longitudinally, where weak fields (relatively) cause the radiation cones emitted at each bend in a trajectory overlap to interfere constructively. Hence, resulting in single or few spectral narrow peaks. Highly collimated beam (horizontally and vertically) results in high brightness. On the other hand (Fig 1 f b), wigglers have fewer dipoles that produce higher fields that generate a continuous spectrum (lower wavelengths) and this results in a high photon flux.

The magnetic fields force the electrons to 'wiggle' around the straight path. While a wiggler produces a wide range of high energy x-rays, an undulator produces even higher intensity x-rays with a narrower range of energies. Fig 1 g shows the difference in using a dipole magnet or a bending magnet to using insertion devices such as undulators or wigglers. Insertion devices thus provide improved brightness and efficiency in the radiation. Furthermore, in the case of (linear) undulators, the electrons are constrained to a planar trajectory and so the radiation produced is highly polarized (virtually 100% linear).

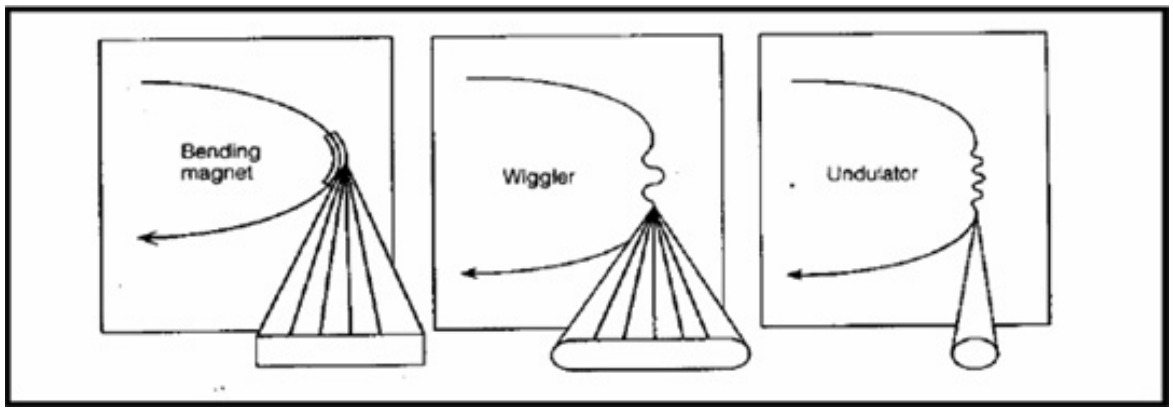

Fig 1 g: Schematic diagram showing the difference in beam widths between the various sources of radiation that utilize different types of magnets.

1.3 VLS PGM BEAMLINE

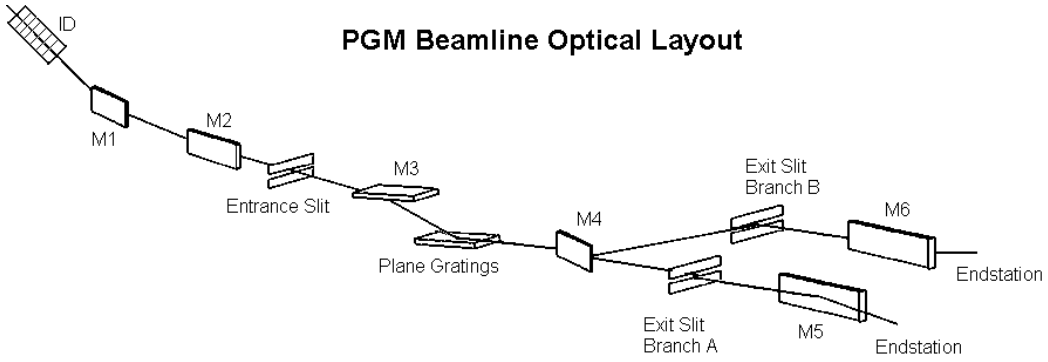

Fig 1 h: Layout of the VLS-PGM beamline. FM, fixed mask; M1, plane mirror; M2, toroidal mirror; M3, spherical mirror; M4, plane mirror; M5 and M6, toroidal refocusing mirrors [1].

An undulator is used as an insertion device (ID) [4] which is the photon source for this particular beamline. VLS PGM beamline shares the straight section of the undulator with the neighboring spherical grating monochromator (SGM) beamline. The fixed masks, which are shared by both the VLS-PGM and SGM beamlines, are used to define the angular acceptance of the VLS-PGM (0.7 x 0.7 $mrad^2$). The first optical component seen in Fig 1 h is a plane mirror M1 which is used to separate a portion of the beam and deflect the beam horizontally by 3º from the SGM beamline [1]. The next optical component is a toroidal mirror M2 which then further deflects the beam horizontally by 9º. Besides its optical function in collimating the beam horizontally and demagnifying the source by a factor of 4 in the vertical direction onto the entrance slit, this mirror absorbs most of the photons with photon energies above ~ 0.5 keV.

To cover the energy range between 5 and 250 eV, the monochromator uses three pairs of spherical mirrors and three VLS gratings. These combined are used to cover different sections of the complete energy range. The M3*L*-Low Energy Grating (LEG)

covers the energy range 5–38 eV, the *M*3*M*-medium energy grating (MEG) the range 25–120 eV, and the *M*3*H*-high energy grating (HEG) the range 98–250 eV.

The latest flux measurements are shown in fig 1 i for the three gratings. A plane mirror can be inserted before the exit slit to divert the photon beam horizontally to a second exit slit. After each one of the slits a vertically oriented toroidal mirror focuses the beam to a spot with a diameter of less than 200 μm to either one of the two experimental stations (station A or station B) as depicted in Fig. 1 h. Fig 1 j shows the toroidal spectrometer aligned at the VLS beamline endstation A.

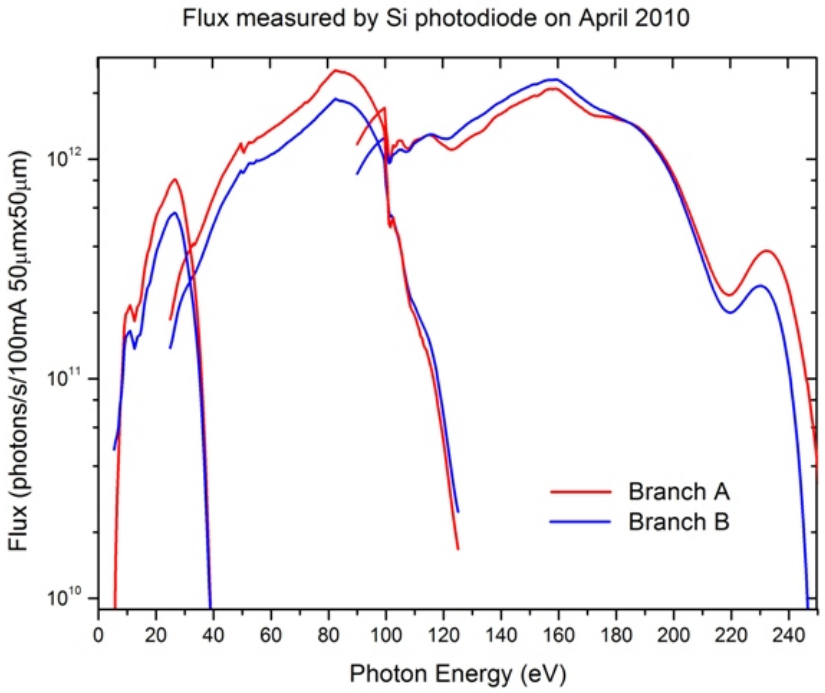

Fig 1 i: The flux measurement as of April 2010 shows the flux for low energy, medium energy and high energy grating.

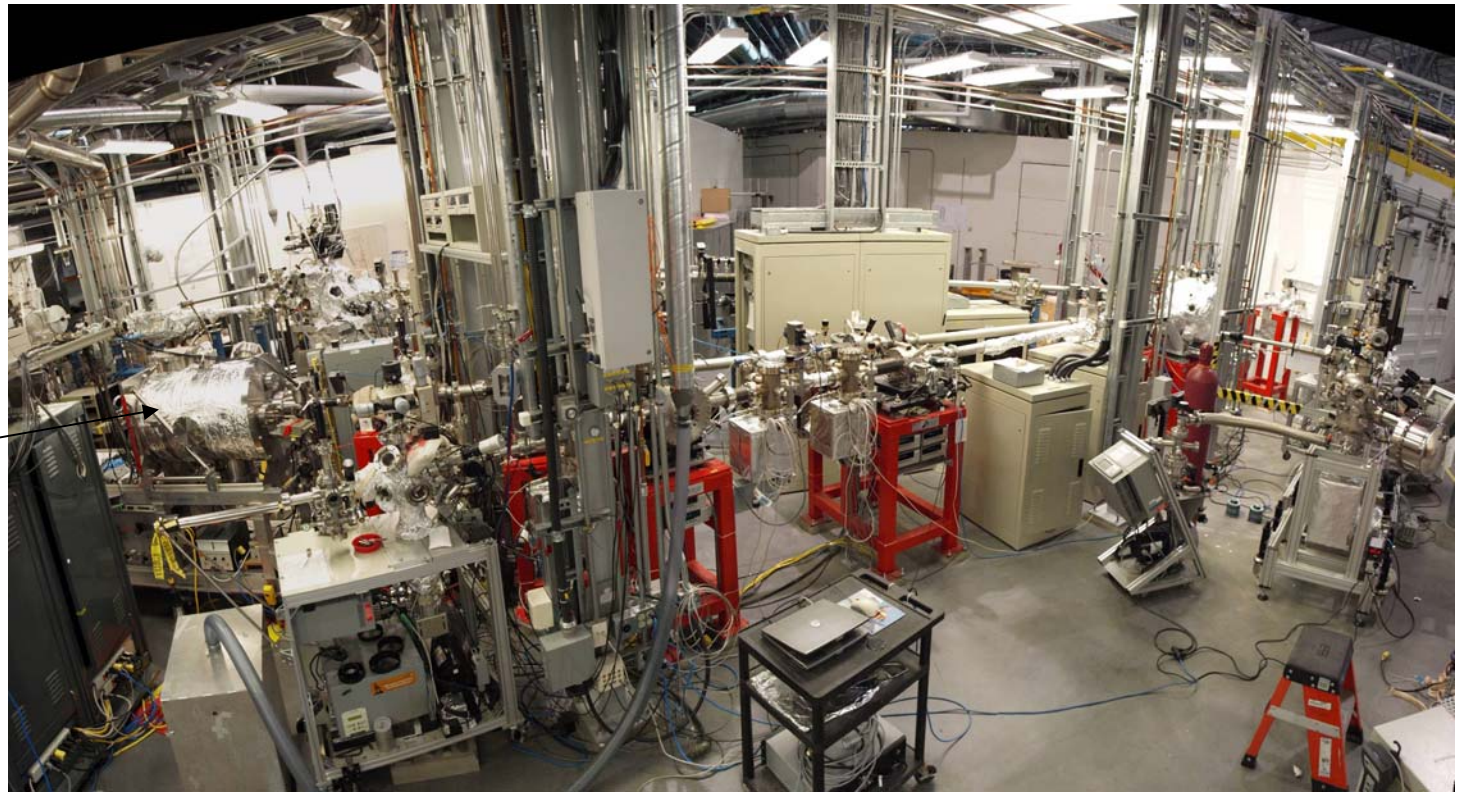

Fig 1 j: Panoramic view of the VLS PGM beamline at the Canadian Light Source (CLS), where all the experiments in this thesis were performed. Also, seen is the toroidal spectrometer that is aligned with the branch A of the beamline.

1.4 LINEARLY POLARIZED SYNCHROTRON RADIATION

1.4.1 ELLIPTICAL POLARIZATION

The plane that contains the electric field vector $\vec{E}$ and the direction of propagation is known as the plane of polarization [5]. For an atom interacting with light, such as monochromatized synchrotron radiation, the plane monochromatic external field can simply be described by the vector potential [6].

$$A(x,t) = \frac{1}{2}\left\{A_o e^{i(k.x-\omega t)} + A_o e^{-i(k.x+\omega t)}\right\} \qquad (1.1)$$

A_o is a complex quantity that contains field intensity and polarization, k is the wavenumber vector and x is the position of the wave and ω is the angular frequency.

The electric field $\vec{E}$ can then be given by

$$E(x,t) = -\frac{dA}{dt} = \frac{1}{2}\left\{E_o e^{i(k.x-\omega t)} + E_o e^{-i(k.x+\omega t)}\right\} \qquad (1.2)$$

where $E_o = i\omega A_o = PE_o$; P is the polarization vector

A plane wave is considered to be in the *(x,y)* coordinate system [5].

$$E_x = a_1 \cos(\omega t - kx + \delta_1) \qquad (1.3a)$$

$$E_y = a_2 \cos(\omega t - kx + \delta_2) \qquad (1.3b)$$

Here, a_1 and a_2 are the amplitudes of the wave in x and y direction and are proportional to a and b in Fig 1 k, respectively. δ_i relates to the phase shift. The expressions are written in a more general form of, an elliptically polarized wave, from which the equations for a linearly polarized light can be derived.

However, in the case of elliptically polarized light the axes are defined in terms of the major and minor axes (as seen in Fig 1 k). The E_x and E_y are rewritten to suit the elliptical coordinate system.

The electric field vector can then be written as:

$$E_\xi = E_x \cos\psi + E_y \sin\psi \quad (1.4a)$$

$$E_\eta = -E_x \sin\psi + E_y \cos\psi \quad (1.4b)$$

For linearly polarized light, i.e. for the ellipse to reduce to a straight line:
$\delta = \delta_2 - \delta_1 = m\pi \ (m = 0, \pm1, \pm2, \ldots)$

In which case ratio of Eqn (1.3a & 1.3b) reduces to

$$\frac{E_y}{E_x} = \frac{a_2}{a_1}(-1)^m \quad (1.5)$$

Depending on the reference coordinate E is then said to be polarized in the y- direction (only E_y would remain) or the x- direction (only E_x would remain). The polarization of the ellipse depends on change in phase difference δ.

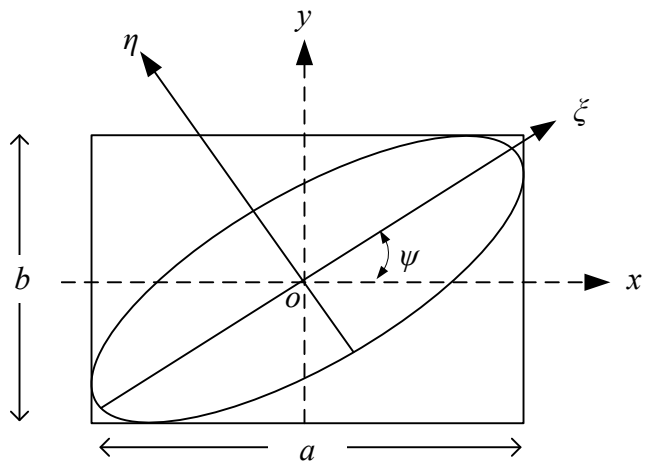

Fig 1 k: Elliptically polarized wave with ψ being the angle between the elliptical axis ξ (major axis) and the x direction and η defines the minor axis [6].

1.4.2 STOKES PARAMETER

The polarization ellipse is characterized by three independent quantities, the major axis *a* and minor axis *b* of the ellipse and the angle that specifies the orientation of the ellipse, χ (see Fig 1l) [6]. G. G. Stokes in 1852 proposed that the state of polarization of partially polarized light be characterized by parameters that were of the same dimensions for practical purposes. The Stokes vector or parameters are four quantities and are as follows:

$$S_{Stokes} = I\begin{pmatrix} 1 \\ S_1 \\ S_2 \\ S_3 \end{pmatrix}$$

I is the total intensity of the wave, while, S_1 , S_2 , and S_3 are related to the angle that specifies the orientation of the ellipse ($0 \leq \psi < \pi$) and the angle that characterizes the ellipcity of the ellipse ($-\pi/4 \leq \chi \leq \pi/4$) (see Fig 1 l). The four measurement quantities refer to three different basis systems $(\hat{e}_x, \hat{e}_y)$, $(\hat{e}_1, \hat{e}_2)$ and $(\hat{e}_r, \hat{e}_l)$.

The total intensity as measured with a polarization insensitive detector is given by *I,* which should equal to the sum of the intensities as measured with polarization sensitive detectors [6].

$$I = I_1 + I_2 = I_x + I_y = I_r + I_l$$

Measurement of excess intensity using a detector which is sensitive to linear polarization along the two orthogonal axes $(\hat{e}_x, \hat{e}_y)$ gives the Stoke's parameter $S_1 = \frac{I_x - I_y}{I}$. S_2 refers to measurement of excess intensity using a detector which is sensitive to linear polarization along the two orthogonal axes $(\hat{e}_1, \hat{e}_2)$ oriented at 45º to the right with respect to $(\hat{e}_x, \hat{e}_y)$, then $S_2 = \frac{I_1 - I_2}{I}$. S_3 refers to the measurement of excess intensity

using a detector which is sensitive to right and left circurlar polarization defined by basis states , $(\hat{e}_r, \hat{e}_l)$ which yields $S_3 = \frac{I_r - I_l}{I}$ (Schmidt [6]).

The Stoke's parameters can vary between + 1 and -1, $S_1 = +1$ and $S_1 = -1$ describe 100% linearly polarized light with the electric field oscillating along the x and y directions, respectively. The degree of polarization P is given by : $P = \sqrt{S_1^2 + S_2^2 + S_3^2}$. For horizontally linearly polarized light $S_1 = 1$, $S_2 = 0$, and $S_3 = 0$, therefore $P = 1$.

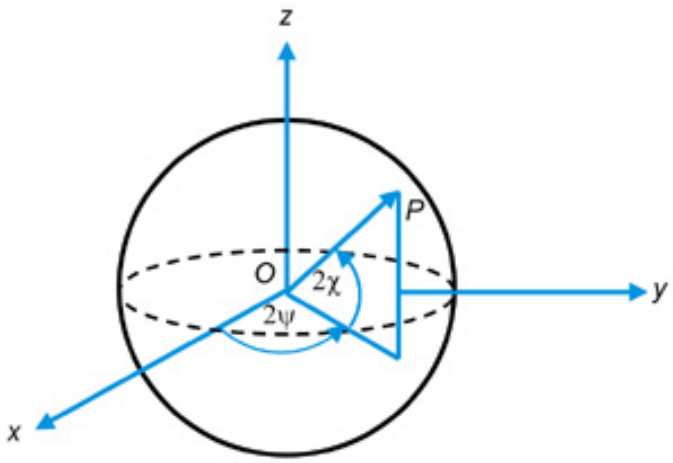

Fig 1 l: Poincaré sphere to represent polarized light [5]. Here x, y, and z are Cartesian coordinate axes, ψ and χ are the spherical orientation and ellipticity angles (of the polarization ellipse), and P is a point on the surface of the sphere. Note that on the sphere the angles are expressed as 2ψ and 2χ. For a unit sphere the Cartesian coordinates are related to the spherical coordinates by the equation. $x = cos(2\chi)\ cos(2\psi),\ 0 \leq \psi < \pi,$ $y = cos(2\chi)\ sin(2\psi),\ -\pi/4 < \chi \leq \pi/4,\ z = sin(2\chi)$

1.4.3 PHOTOIONIZATION CROSS SECTION:

The cross-section σ for a certain type of event in a given collision is the ratio of the number of events of this type per unit time per unit scatterer, to the flux of incident particles with respect to the target [6].

$$\sigma_A = \frac{(number\ of\ A\ events)}{(unit\ time)(unit\ scatterer)(flux\ of\ incident\ particles)}$$

The cross-section can also be defined as the probability of the incident particle to undergo a specified event as being proportional (transition probability) to the total number of target particles per unit target area.

While the cross-section σ provides the number of particles that undergo a specified event with respect to the target, it does not provide information of the direction of the scattered particles. The differential cross-section dσ/dΩ gives information on the number of particles scattered into a solid angle. Suppose that the laboratory coordinate system is referred to as (θ, φ) and that the particles that are scattered off from an element of a ds^2 to a subtended solid angle $d\Omega$, the fraction of particles incident into the solid angle $d\Omega$ around the laboratory reference frame (θ, φ) for n target scatterers per unit volume with target of thickness w is given by:

$$nw\left(\frac{d\sigma(\theta,\varphi)}{d\Omega}\right)d\Omega$$

$\left(\frac{d\sigma(\theta,\varphi)}{d\Omega}\right)$; gives the differential cross section.

In Fig 1 m, the detector which the emitted electrons strike is referenced by angles (θ,φ). For all the particles that are scattered out of the event, the total cross section σ_T is given by :

$$\sigma_T = \int\left(\frac{d\sigma(\theta,\varphi)}{d\Omega}\right)d\Omega = \int_0^{2\pi}\int_0^{\pi}\left(\frac{d\sigma(\theta,\varphi)}{d\Omega}\right)\sin\theta\, d\theta\, d\varphi \qquad (1.6)$$

The differential cross section for photoionization for randomly oriented atoms, with a partially elliptically polarized incident light is given by :

$$\frac{d\sigma(\theta,\varphi)}{d\Omega} = \frac{\sigma}{4\pi}\left\{1-\frac{\beta}{2}\left[P_2(\cos\theta) - \frac{3}{2}A\sin^2\theta\right]\right\} \qquad (1.7)$$

Here $A = S_1 \cos 2\phi + S_2 \sin 2\phi$ and the Legendre polynomial $P_2(\cos\theta) = (3/2\cos^2\theta - 1/2)$, β is the angular distribution or anisotropy parameter.

As mentioned previously the total cross section σ_T follows from integrating the differential cross over full solid angle. Following integration σ_T, as expected is independent of polarization of incident light, this being a result of random distribution of atoms in the initial state. Hence, the need to determine cross section that is sensitive to the polarization, which is the partial cross section. σ_T, is a function of photon energy and as such is the total cross section that sums over all photoabsorption/ionization processes involved in reaching a final state. Of more interest is the cross section into a particular final state via a *particular* process; each of the mechanisms will have a completely different cross section [7].

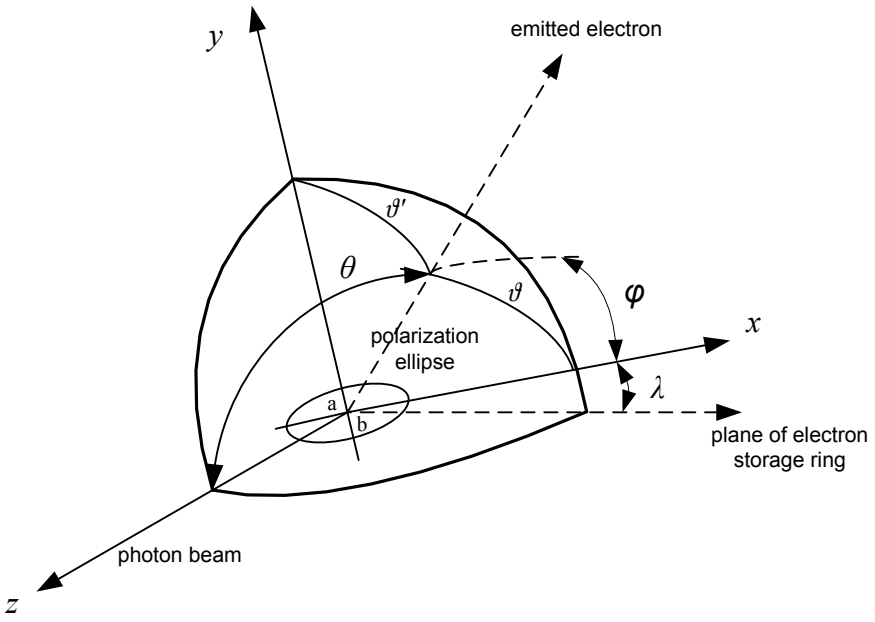

Fig 1 m : Geometrical representation of a "tilted" collision frame where the coordinate system is centered in the middle of an interaction region that is defined by the direction of the photon beam (z –axis) and two orthogonal axes where the x-axis defines the plane of the storage ring. The direction of the emitted electron is described by the angles (θ, φ). It should be noted that the major (a) and minor (b) axes of the polarization ellipse (the ellipse lies in the plane perpendicular to the direction of the photon beam) are aligned with the x- and y- axes respectively. λ is the tilt angle between the x-axis and the plane of the storage ring. In practice, $\lambda = 0^{\circ}$ is a well aligned optical arrangement.

For linear polarization, as mentioned previously the Stokes parameter $S_1 = \frac{I_x - I_y}{I}$ and $S_2 = 0$. Then Eqn 1.7 becomes

$$\frac{d\sigma(\theta,\varphi)}{d\Omega} = \frac{\sigma_T}{4\pi}\left\{1 - \frac{\beta}{2}\left[P_2(\cos\theta) - \frac{3}{2}\cos 2\varphi \sin^2\theta\right]\right\} \qquad (1.8)$$

where ; $P_2(\cos\theta) = 3/2\cos^2\theta - ½$, $\cos 2\varphi = 2\cos^2\varphi - 1$

Applying spherical trigonometry as seen in Fig 1m , $\cos\vartheta = \cos(90 - \theta)\cos\varphi$

Eqn 1.8 simplifies to the well known following expression for a 100% linearly polarized light:

$$\frac{d\sigma(\theta,\varphi)}{d\Omega} = \frac{\sigma_T}{4\pi}\left\{1 + \frac{\beta}{2}\left(3\cos^2\vartheta - 1\right)\right\} \qquad (1.9)$$

Note that the angle ϑ is referenced with respect to the major axis of the polarization ellipse (see Fig 1 m) and *not* the laboratory frame. However, every effort is made to control the physical and optical alignment so that the two frames are identical in the case of a "horizontal" linear undulator radiation.

1.4.4 ANGULAR DISTRIBUTION

The emission pattern of photoelectrons has characteristic angular distributions and is not isotropic in space. In the electric dipole approximation, the electric field $\vec{E}$ vector of the incident light is relevant. The electric field vector $\vec{E}$ causes forced oscillations of the photoelectrons and this leads to directionality in the electron emission. Eqn 1.9 is the expression for differential partial cross section for a photoionization process with 100% linearly polarized light, which is a function of the characteristic angular distribution parameter β. Measurement at any angle yields information on β if σ_T is known , except at the magic angle of 54.7° where the legendre polynomial reduces to zero, which implies that the result is insensitive to β .

The numerical value of β determines the actual shape of the angular distribution pattern. For the special case of an *s*-electron and for negligible spin-orbit effects, β parameter has an *energy independent* value of $\beta = 2$ [6]. This is the case for the 1*s* photoionization in helium (i.e. He^+ *(n=1)*) that has the characteristic angular distribution pattern as shown in Fig 1 n.

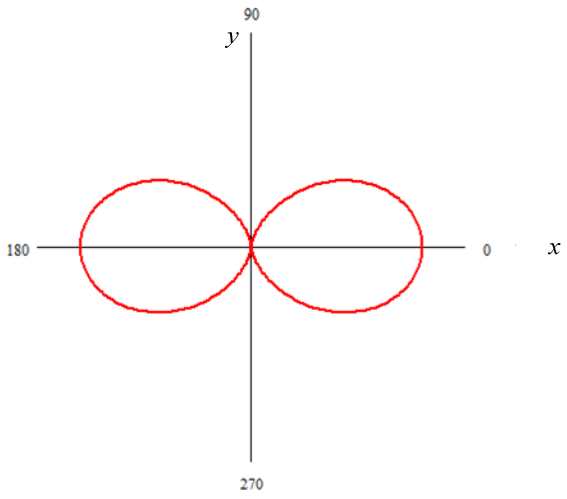

Fig 1 n: Photoelectron emission leads to a spatial intensity distribution with axial symmetry around the electric field $\vec{E}$. Shown is the characteristic angular distribution for the ejection of *ns* electron ($\beta = 2$) given by a $\cos^2\vartheta$ distribution [6] in case of linearly polarized light in the *x* direction; the electric field $\vec{E}$ lies along the *x*-axis.

In general the asymmetry parameter depends on the partial wave matrix elements and the phase shift between the two partial waves (according to the dipole selection rules) of the outgoing electron. The β parameter can vary between 2 and -1 depending on the different amplitudes that contribute to the photoionization process and interfere [7]. Hence, the β parameter yields information on the angular momenta involved in a photoionization process and varies with both photoelectron and photon energies.

1.5 REFERENCES

[1] Y F Hu *et al* 2007 Rev Sci Instrum **78** 083109

[2] Attwood D. 1999 Soft X-Rays and Extreme Ultraviolet Radiation *Cambridge University Press* pp 124-137.

[3] Canadian Light Source (http://www.lightsource.ca/education/whatis.php)

[4] Reininger R., Tan K and Coulthard I. 2002 Rev Sci Instrum **73** 3

[5] Born M and Wolf M 1999 Principles of Optics *Cambridge University Press* pp 25-31

[6] Schmidt V 1997 Electron Spectrometry of Atoms using Synchrotron Radiation, *Cambridge University Press* pp 25-29,318, 41-45,19-20,52

[7] Becker U and Sherley D.1996 A. VUV and Soft X-Ray *Photoionization Plenum Press* pp 137-138

CHAPTER 2: EXPERIMENTAL APPARATUS

2.1 INTRODUCTION

2.2 TOROIDAL SPECTROMETER

2.2.1 TOROIDAL GEOMETRY

2.2.2 TOROIDAL ANALYZERS

2.2.3 INTERACTION REGION

2.2.4 ENTRANCE LENS

2.2.5 EXIT LENS

2.2.6 EDGE EFFECTS AND FIELD DISTORTIONS

2.2.7 POSITION SENSITIVE DETECTORS (PSDs)

2.3 REFERENCES

2.1. INTRODUCTION

Experiments in this work were performed at the CLS using a dual toroidal spectrometer [1] that was designed by Reddish *et al* primarily to perform (γ,2e) coincidence studies. The versatility of this spectrometer will be described in this chapter. The spectrometer properties are ideal for detecting low energy electrons (1-50 eV) and ions (< 10 eV).

The spectrometer consists of two toroidal analyzers that can detect two outgoing charged particles simultaneously, after an ionization event. It has the capability of preserving the angle of emission and energy resolving the outgoing charged particles. The energy-resolved and angle-dispersed charged particle images are recorded using two-dimensional position-sensitive detectors.

Discussed in this chapter are the constituents of the toroidal spectrometer and design details of the apparatus. The focusing properties of the analyzers that are based on toroidal geometry will be presented in this chapter. Various improvisations made in the past for effective performance of the toroidal spectrometer to perform multi-coincidence studies are also presented.

2.2 TOROIDAL SPECTROMETER

2.2.1 TOROIDAL GEOMETRY

Toroidal analyzers are the topological link between a cylindrical analyzer (127º deflectors), and a hemispherical analyzer (180º deflectors) [2]. Fig 2 a and b show a cylindrical (127º) analyzer and a hemispherical (180º) analyzer respectively. The energy dispersive refocusing in a hemispherical analyzer is after a deflection of 180º and for the 127º analyzer the refocusing is after a deflection of 127º. The outer surface, inner surface and the centre are designated by potential V_2, V_1 and V_o. In the Table 2.1, r_s is the radius of the entrance aperture and E_p is the 'pass energy' or the energy of the charged particles that traverse through the analyzer. The energy resolution at full width half maximum

(FWHM) for each analyzer is given in Table 2.1. It can be seen that the 180º analyzer has a superior energy resolution, for the same r_s, R_o and α.

The hemispherical analyzer has the property of "parallel to point" focusing, where parallel rays enter the hemisphere in the axial (non-energy dispersive) plane and are brought to a focus after only 90° (fig 2 d). The rays then diverge and leave the hemisphere after deflecting through 180° as parallel rays resulting in lateral image inversion. Focusing in the energy dispersive plane has been described as "point to point" focusing. Exit slits and entrance slits have been introduced for this purpose; i.e where one can constrain the image to points in a given radial plane. In a cylindrical analyzer, the rays refocus in the energy dispersive plane after deflecting through 127°.

Table 2.1: Table comparing the properties of 127º and 180º analyzers.

Analyzer Type	Outer Potential	Inner Potential	Energy Resolution (FWHM)
127º Analyzer	$V_2 = V_0\left(1+2\ln\frac{R_2}{R_0}\right)$	$V_1 = V_0\left(1+2\ln\frac{R_2}{R_0}\right)$	$\frac{\Delta E_{FWHM}}{E_P} \approx \frac{2r_s}{R_0} + 0.33\alpha^2$
180º Analyzer	$V_2 = V_0\left(\frac{2R_0}{R_2}-1\right)$	$V_1 = V_0\left(\frac{2R_0}{R_1}-1\right)$	$\frac{\Delta E_{FWHM}}{E_P} \approx \frac{r_s}{R_0} + 0.25\alpha^2$

In Fig 2 d, the potentials at the inner and outer surfaces are designated by V_1 and V_2 respectively. The inner and outer radii are denoted by R_1 and R_2 respectively. The mean radius is denoted by R_o. The central trajectories and the outer trajectories of the charged particles are denoted by dashed lines and straight lines respectively. The entrance and exit slit widths are denoted by w and the launch angular range is denoted by $2\Delta\alpha$, α is the beam half angle.

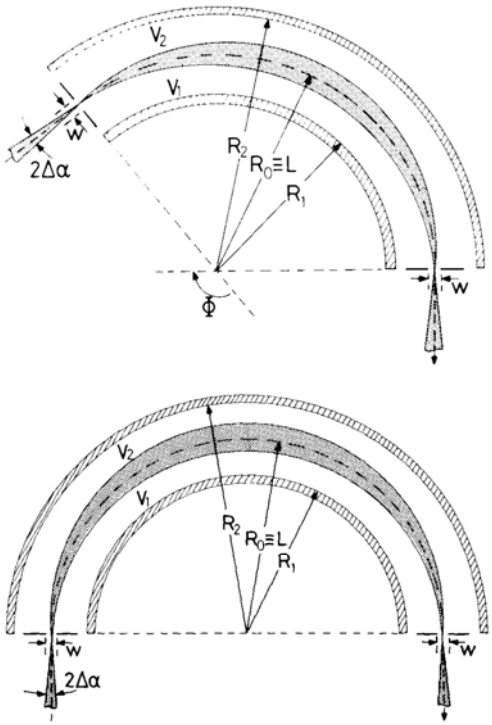

Fig 2 *a*: Schematic of a Cylindrical (θ = 127º deflectors) analyzer (Top).These analyzers consist of two cylinders where the charged particles are deflected by 127º, denoted by θ. 2 *b*: Schematic of hemispherical (θ = 180º deflectors) analyzer (Bottom). The analyzers consist of two concentric hemispheres.

Toroidal analyzers have the capability of energy selecting the charged particles while preserving the initial angle of emission. This property is essential for angle resolved studies where one needs to study the angular information in the axial plane while maintaining the focusing conditions in the energy dispersive plane. The study by Toffoletto *et al.* [3] shows that the focusing properties of toroids can be determined as a function of the sector angle, θ, the ‘‘cylindrical-to-spherical radius ratio’’ ($c = a/b$) as shown in Figs. 2 c and 2 d. The ‘‘cylindrical’’ radius, a is the distance from the interaction region to the toroidal deflector entrance and the ‘‘spherical’’ radius, b is the radius of the central path through the deflector as seen in Fig. 2 c. Consequently, a traditional 180° hemispherical analyzer, ($c = 0$) and 127° cylindrical analyzer ($c = \infty$) have “point to point” focusing properties in their respective energy dispersive planes.

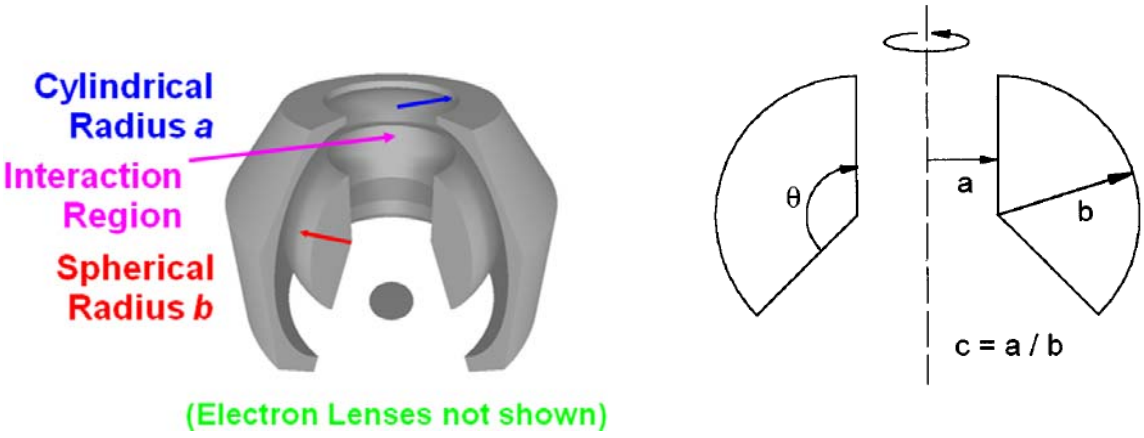

Fig 2 c: A toroidal analyzer is characterized by cylindrical radius *a* and spherical radius *b* and sector angle θ (*Left:* three dimensional view of the toroidal analyzer; *Right*: geometrical schematic of the toroidal analyzer)

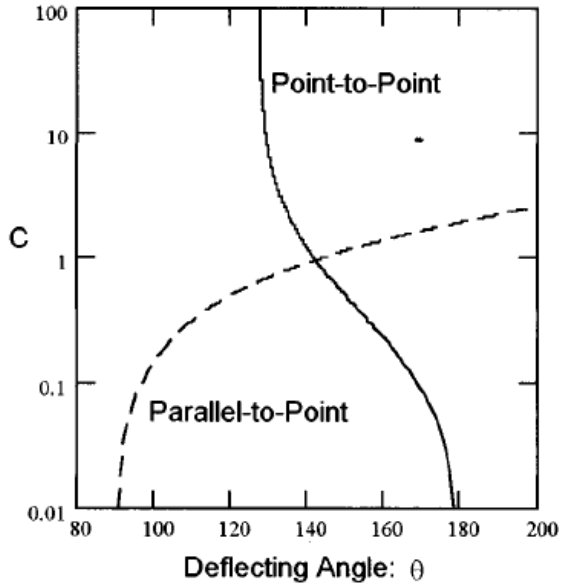

Fig 2 d: A plot of the point-to-point (solid) and parallel-to-point (dashed) focusing conditions as a function of the toroidal parameter *c* .The point-to-point curve has asymptotic limits of 127° and 180° with the object and image positions at the entrance and exit surfaces of the toroids, respectively. In the case of parallel-to-point focusing, the object position is on the axis of symmetry due to the very weak focusing effects of the entrance lens in the axial plane.

For a toroidal analyzer *c*, needs to be chosen so that the deflection angle , θ , i.e., for point-to-point focusing also satisfies the condition for parallel-to-point focusing. It can be seen in Fig 2 d the point-to-point imaging conditions lie on a curve between the limits correspond to cylindrical and hemispherical analyzers. Hence, the design parameters were chosen and are as follows [see [1] for further details]:

Cylindrical radius "*a*" = 95mm

Spherical radius "*b*" =100mm

Inner toroidal radius "R_1" = 75 mm

Outer toroidal radius "R_2" = 125mm

From matrix formalism given by Toffoletto *et al* [3]: *c* = 0.95; Sector angle θ = 142°

The theoretical potentials *V(r)* on the inner and outer toroidal surfaces, determined by Toffoletto *et al* [3] are:

$$V(r) = V_o\left[1+\left(2+\frac{4}{c\pi}\right)\ln\left(\frac{2br+\pi ab}{2br+\pi ar}\right)\right] \qquad (2.1)$$

Here, eV_o is the "pass" energy, *r* is the spherical radius of the toroidal surface.

From the studies of Toffoletto *et al* [3] and Read *et al* [4], the theoretical energy resolving capability of the toroidal analyzer is modeled as:

$$\frac{\Delta E_{FWHM}}{eVo} = \frac{\omega}{D.b} + \kappa\alpha^2 \qquad (2.2)$$

; ω is the width of the toroidal entrance and exit slits, here ω = 1mm

Dispersion "*D*" is given by $D = \frac{c\pi+2}{c\pi+1}$, with *D*= 1.25 for this spectrometer

κ is a constant that is specific to the analyzer geometry , κ = 0.3 is assumed for this particular toroidal geometry

α the maximum half angle entrance in the axial or energy dispersive plane, α=5º in this case.

The theoretical energy resolution (FWHM) for this spectrometer is:

$$\frac{\Delta E_{FWHM}}{eVo} = \frac{1}{100} \qquad (2.3)$$

Thus, for pass energy of 5 eV, the energy resolution is predicted to be 50 meV, sufficient to resolve vibrational levels in diatomic molecules (100 - 300 meV). Expression 2.1 and 2.3 correlate very well with what we observe experimentally.

2.2.2 TOROIDAL ANALYZERS

The spectrometer consists of two analyzers (partial toroids) that are based on the toroidal geometry as described in section 2.2.1. The larger analyzer has a mechanical angular range of 180º and the smaller analyzer has an angular range of 100º. A schematic of the apparatus seen in Fig 2 e shows the relative orientation of the toroidal analyzers with respect to each other and with respect to incoming photon beam.

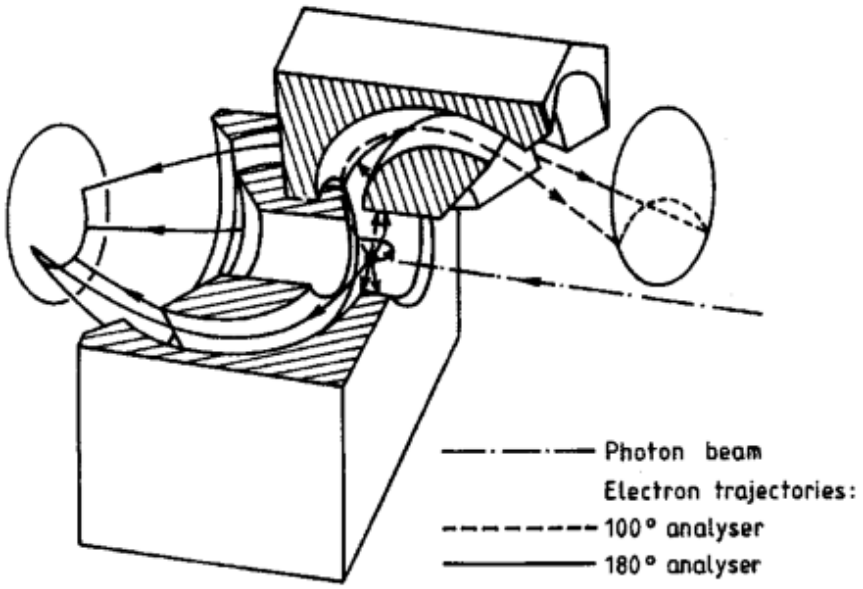

Fig 2 e: A schematic diagram showing the configuration of the two partial toroids along with lines indicating central trajectories of charged particles with a selection of emission angles, as discussed in the text. The entrance and exit lenses are not shown for reasons of clarity. The mechanical angular acceptances of the two analyzers in the plane orthogonal to the photon beam are 100° and 180°.

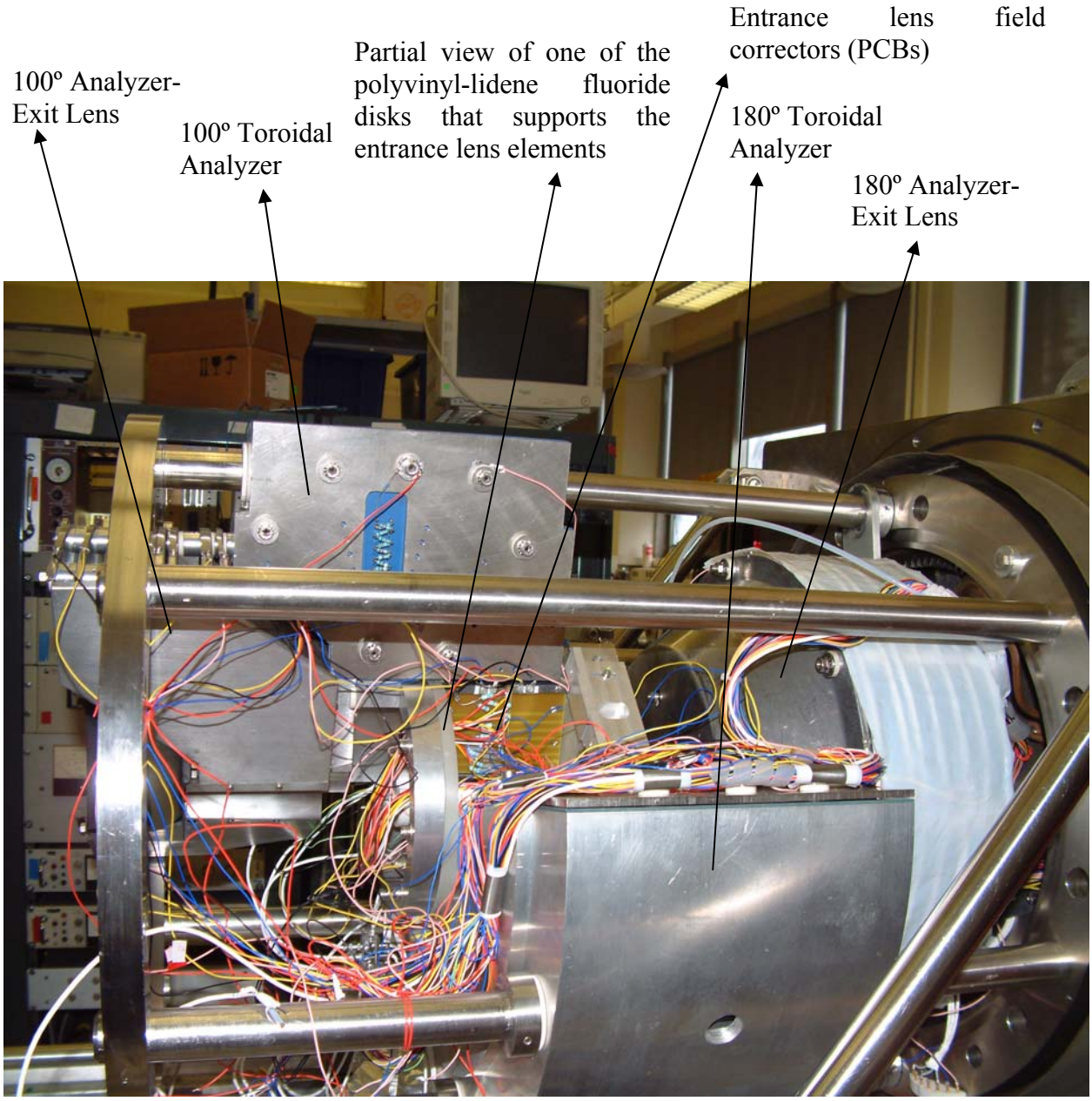

Fig 2 f: A picture of the toroidal spectrometer with a partial view of the assembled entrance lens, exit lens and the toroids. The position sensitive detectors (PSDs) are not shown.

The region in space where the photon beam and the target gas intersect is defined as the interaction region. Subsequent to the photoionization event, the charged particles (photoions and/or photoelectrons) that are emitted in the plane orthogonal to the photon beam, are accelerated and then focused at the toroidal entrance slit by a series of entrance lens elements. The spectrometer is positioned in a cylindrical stainless-steel chamber, lined internally with two coaxial mumetal cylinders. The inner and outer toroids are made from aluminum alloy and are surface coated with aerosol graphite to curb emission of secondary electrons and to avoid field perturbations produced due to surface oxidation.

Electrons/ions of specific energy traverse the gap between two toroidal surfaces to the exit slits of each analyzer. The electrostatic exit lenses accelerate and refocus the energy resolved charged particles to their respective two-dimensional position-sensitive detectors. The final images are hence energy resolved and angle dispersed and are shaped in the form of circular arcs (with circle centers on the photon axis), in which the position around the perimeter is directly related to the initial azimuthal photoelectron emission angle defined with respect to the major axis of the light polarization ellipse. Fig 2 f shows a picture of the spectrometer with a partial view of the toroidal analyzers, their mutual orientation and relative positioning of the entrance and exit lens.

2.2.3 INTERACTION REGION:

The interaction region is defined by the intersection of the photon beam and of gas emanating from a copper hypodermic needle positioned orthogonal to the photon beam (see Fig 2 g). The toroidal spectrometer has a perpendicular plane geometry where the electrons/ions are detected in the plane perpendicular to the photon beam direction. The size of the interaction beam in the axial plane is defined by the diameter of the photon beam and by the electron optics properties of the entrance lenses.

The spectrometer is connected to the VLS PGM beamline with the aid of a differential pumping system. Photons enter the interaction region via an insulated photon

tube that has an internal diameter of 8 mm. Close to the interaction region, the converging photon beam passes through two collimating apertures of diameters 1 mm and 1.5 mm, separated by several cm; situated within the photon tube. This arrangement serves to define the optical axis of the spectrometer and when aligning the spectrometer with the beamline, the whole apparatus is moved so that the photon beam and the spectrometer axes are co-linear. This collimator is suitably biased such that none of the metal scattered photoelectrons leave the endpiece, the geometry is also designed to prevent the electric field from penetrating into the target vicinity. The interaction region is surrounded by a 40 mm diameter cylindrical molybdenum foil (coaxial with the photon beam) which screens the photon beam path from the electric fields emanating from the toroid entrance lenses. An aluminum photodiode (biased) is used as a beam dump and also to monitor the photon flux.

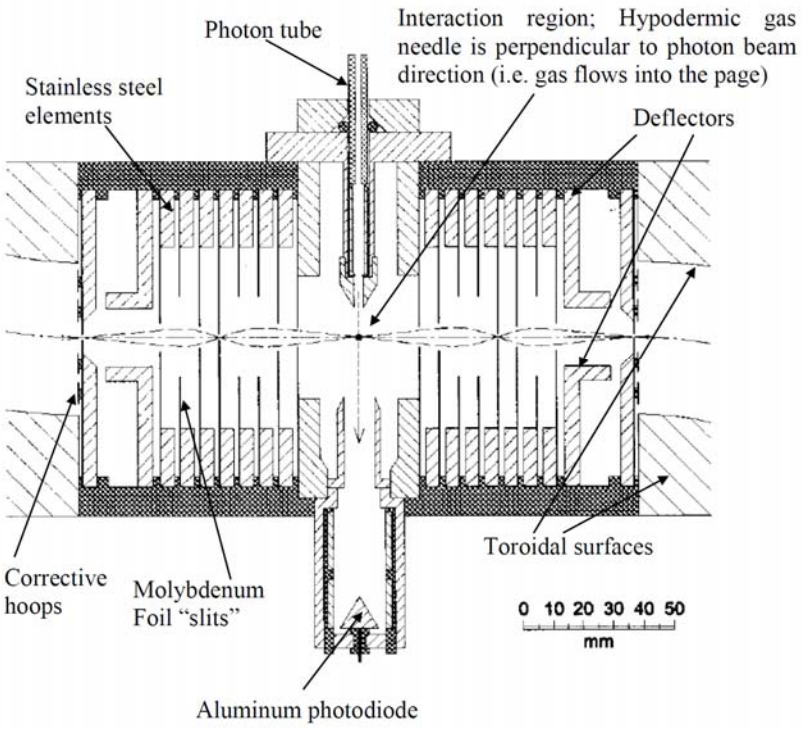

Fig 2 g: A diagram of the interaction region along with entrance lenses shown in the radial or energy dispersive plane. A series of coaxial cylindrical surfaces of increasing radii form slits that represent the entrance lenses. The acceptance angle in radial plane is ± 5 º and varying slit widths on the lens elements is shown in the above figure. The flux from the photon beam is monitored by an aluminum photodiode.

2.2.4 ENTRANCE LENS:

A series of coaxial cylinders (made from nonmagnetic 304 LN stainless steel) of increasing diameters with slits on their curved surfaces form the entrance lens elements on the two analyzers. The cylinders support curved molybdenum foil that fit into each groove of the increasing diameter of the coaxial cylinders. The cylinders are mounted on a rigid polyvinyl-lidene fluoride disk to provide mutual insulation and mechanical alignment. The lens is split into two halves with each disc attached to the individual partial toroidal analyzers. As seen in Fig 2 h, when the lenses are mounted on the toroids, the mechanical positioning of the lenses leads to the actual slits (i.e. the gap) between the two halves.

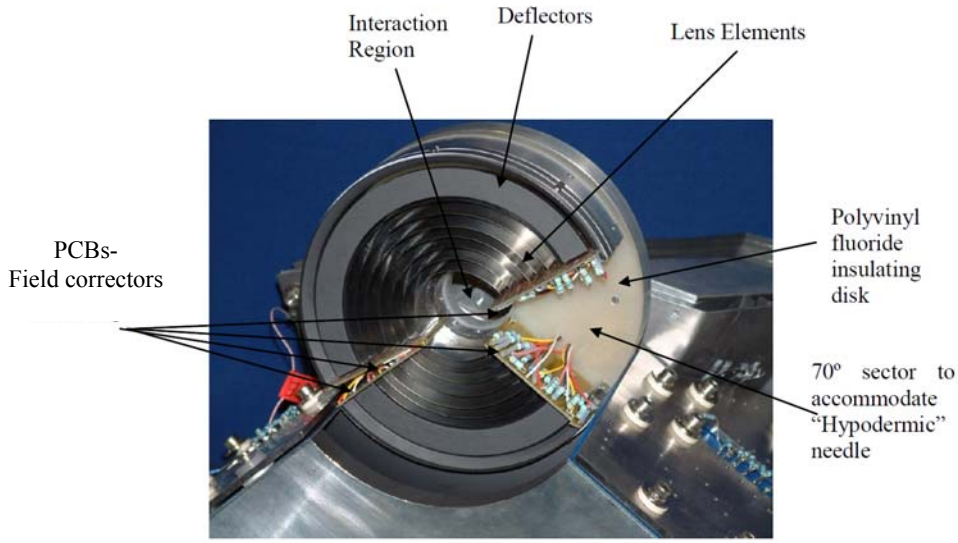

Fig 2 h: Seen is one half of the cylindrical entrance lens mounted on one of the toroidal analyzers. The other half is mounted on the other toroidal analyzer and upon mechanical assembly (i.e. when the two analyzers are brought together) they form a complete lens.

The lens system comprises of seven elements and a deflector (see Fig 2 g). They behave like two multi-element lenses providing an intermediate crossover in the vicinity of the central electrode. In the middle of lens elements is a 2 mm slit that reduces the

transmission of background electrons. The voltages on the entrance lens elements of each analyzer are tuned for the best possible detection efficiency and optimum focusing.

Each lens element is controlled by an external power supply. The analyzers are connected via electrical feed throughs from the chamber to separate power supplies. All the lens power supplies float on a "local" or virtual" earth, which corresponds to "0 eV" of electron/ion energy and its potential with respect to real earth corresponds to the energy of the transmitted electron or ion. This implies that to detect a 5 eV electron emerging from the interaction region, the first lens element is set to 5 eV and changing this virtual earth potential will change all the other lens potentials with respect to the real earth. This maintains the focusing of the electrons through the system to first order. Fig 2 i shows an overview of the wiring schematic of the entrance lens with respect to "virtual" earth.

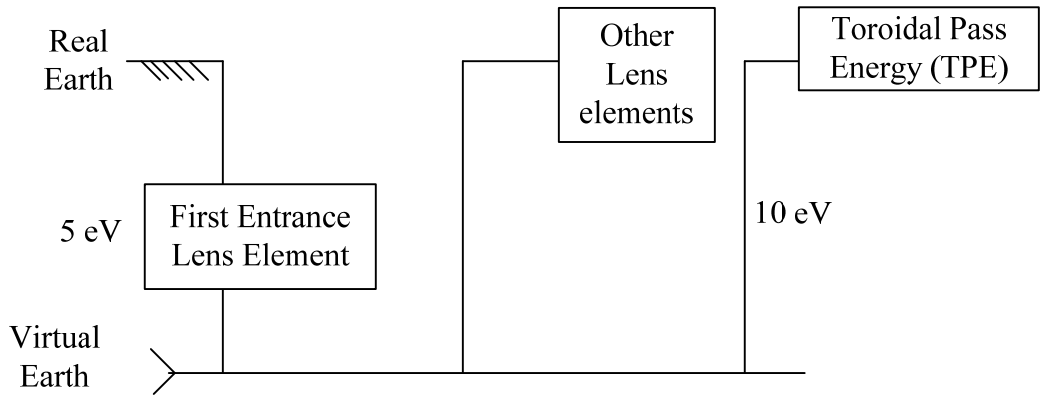

Fig 2 i: Shown is the wiring schematic of the electron-optics. The first entrance lens element which is the extraction potential is termed as the "virtual" earth potential and all other lens elements (except second and third entrance lens elements) are wired with respect to this virtual earth. For further details, please refer to the text.

In this work, the second and third entrance lens elements are wired separately from the other lens elements via a high voltage (HV) power supply. For a chosen toroidal pass energy, the voltages for the outer toroid, inner toroid are derived from Eqn 2.1, 2.2 and 2.3 (using the mechanical radii). The voltages for the field termination correctors in the toroids are empirically scaled with respect to the voltages of the inner and outer

toroids. However, all the above voltages can be altered slightly to obtain the best results. The field termination correctors in the entrance lens and the gas needle are controlled through a different external supply.

2.2.5 EXIT LENS

Fig 2 j shows a lateral view of the exit lens assembly for the smaller toroid and Fig 2 k shows a scaled schematic of the exit lens. Slits on series of eight concentric aluminum cones form the exit lens assembly. The first, third and fourth conical surfaces are maintained at the pass energy of the toroid. The second conical surface is split into two sections that act as deflectors for the exit lens. The next four conical surfaces form the exit lens elements and are designed to act like a standard three element lens with a moveable central position for improved focusing ability.

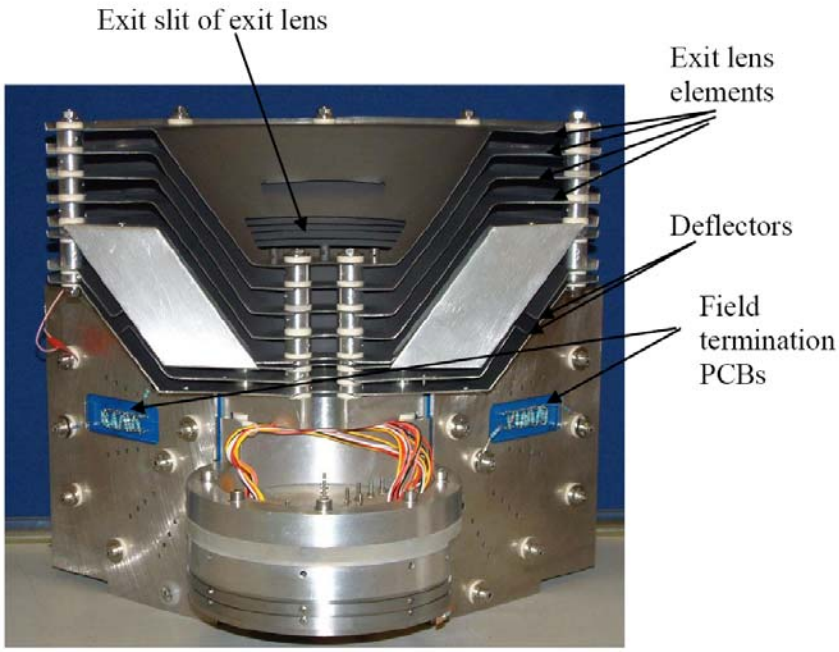

Fig 2 j: Shown in this figure is a side view of the exit lens assembly of the 100º toroid. The detector is mounted just above the exit slit of the lens. It should be noted that the exit lens elements on the 180º toroid are complete (i.e. have a 360º symmetry).

The charged particles from the exit slit are transported through the lens to the detection plane. The planar slit approximation was again adapted for this lens system [5], however, due to the conical geometry this adaption results in the trajectories varying below and above the optic axis. To correct for this effect, a magnification of 0.5 was built into the lens design, in order to restrict the image size. The final image is energy resolved and angle dispersed.

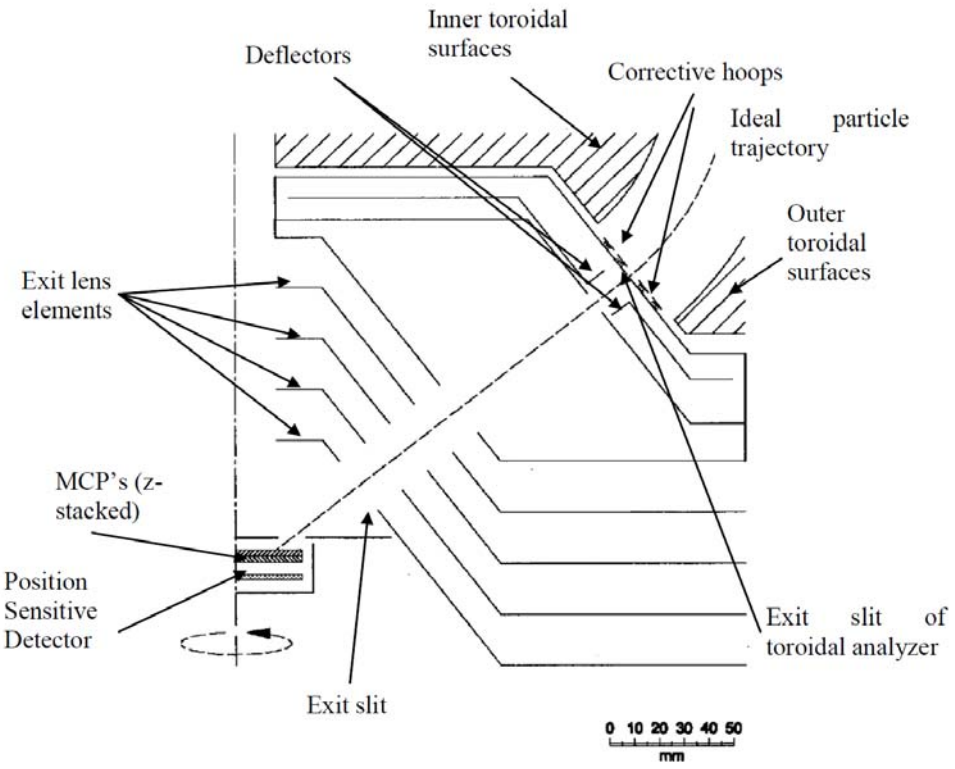

Fig 2 k: A scale diagram of the exit lens assembly, which transports angle and energy dispersed charged particles from the exit slit of the toroidal analyzer to the position sensitive detectors. The elements are formed from slits cuts into curved surfaces of a series of coaxial cones. The charged particles are finally incident on the uppermost MCP at an angle of 52º to the normal.

2.2.6 EDGE EFFECTS AND FIELD DISTORTIONS:

ENTRANCE LENS-FIELD CORRECTORS

The curved lens system design was adapted from the Harting and Read [5] planar slit geometry, conditional to $h/2r << 1$, as shown by Leckey [6]; h being the slit width and r the radius of curvature of the element. However, this lens model was designed in an older version of SIMION that assumed axial symmetry, which is not strictly applicable in case of partial toroids. Hence, there were issues with end effects with the lenses that caused field penetration between the two analyzers, which one would not consider while assuming a full axial symmetry. These effects limited the angular acceptance range of the larger toroid from 180º to 160º. Hence, to control these end effects field correctors, i.e. PCBs (printed circuit board), were incorporated. The PCBs contain copper tracks where the inter-element gaps are relatively large. The arc shaped copper tracks are controlled by external voltages whose potentials can be altered empirically to optimize the termination of the end effects.

TOROIDAL FIELD CORRECTORS

Due to the lack of cylindrical symmetry, the partial toroids cause edge effects which result in electric field distortions that curb the maximum possible angular range and alter the focusing properties of the analyzers, as they do in the lenses. Similar to the concept of inserting corrective ‘hoops’’ in the end plane of hemispherical analyzers to terminate the electric field, two similar corrective strips have been placed on both sides of the toroid entrance and exit slits. Fig 2 l shows the schematic of the exit lens, with the field correcting strips seen near the exit slit.

Strips etched on seperate PCBs have been implemented to terminate the field at the edge planes of the partial toroids are controlled by voltages supplied through external power supplies. The copper pads act like a potential divider circuit where the voltages scale empirically. Fig 2 k shows the field termination PCBs on the sides on the toroid. Careful use of field correction methods minimizes field distortion and generally works well in practice.

2.2.7 POSITION SENSITIVE DETECTORS (PSDs)

Two dimensional Position Sensitive Detectors (PSDs) situated after each of the exit lens consist of "chevron" configured microchannel plates (MCPs) and a resistive anode encoder (shown in Fig 2 m). Electric field caused by the voltage applied across the MCP drives the secondary electrons to the channel surface. The repetition of this process creates a cascade of electrons along the channel that results in a cloud of electrons to the order of 10^3, which arrive at the rear of the plate. Since each electron pulse is restricted in a single channel, the spatial pattern of electron pulses that are formed at the rear of the plate preserve the pattern (image) of the particles that were incident on the front surface.

A standard chevron configuration suppresses ion feedback, consists of two MCPs, whose "channels" are aligned at ~ 10 º to their surfaces, producing a "v" like shape [8] (seen in Fig 2 l). Individual glass capillaries that form a single "channel" are to the order of 10 μm and are arranged in grid like format on a thin plate.

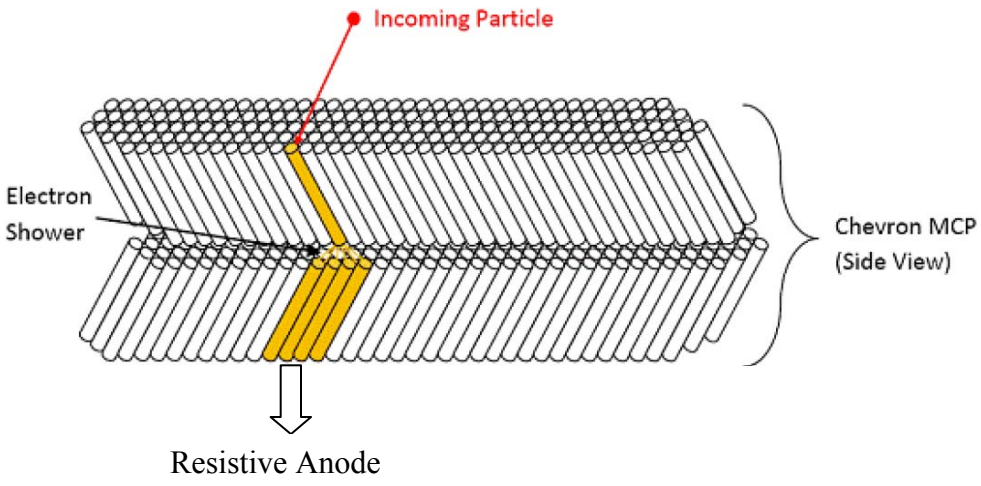

Fig 2 l: A diagram of chevron configured MCP plates that show the incoming particle is transiting through a channel (glass capillary). Upon collision with the walls of the capillary, the incidence signal multiplies and then transits through the channels in the second plate eventually arriving at rear end of the detector surface. Image courtesy [7].

Fig 2 m: A picture of chevron configured 40mm MCP plates manufactured by Quantar Technologies along with the resistive anode encoder. Image courtesy [8].

The MCPs are placed over commercial two-dimensional resistive anode encoders manufactured by Quantar Technology Inc (model QT3394). The charge cloud from the MCP is divided into four linear portions among the four corners of the resistive anode. The pulses from the anode are fed into capacitatively coupled charge sensitive preamplifiers that lie outside the vacuum chamber and are connected to "position" computers (model QT2401). The position computers derive the incident position in terms of 0.5-4 V analog (*x,y*) pulses. The *x,y* images from each detector are displayed on their respective oscilloscopes. Fig 2 n and 2 o shows the angle dispersed and energy resolved images obtained for the 180º and 100º analyzers respectively. For coincidence experiments along with the (*x,y*) images, timing pulses in the form of TTL pulses are obtained. The spectrometer is controlled by a dedicated 120 MHz Pentium PC via a CAMAC interface. The data acquisition details and experimental techniques are explained in Chapter 3.

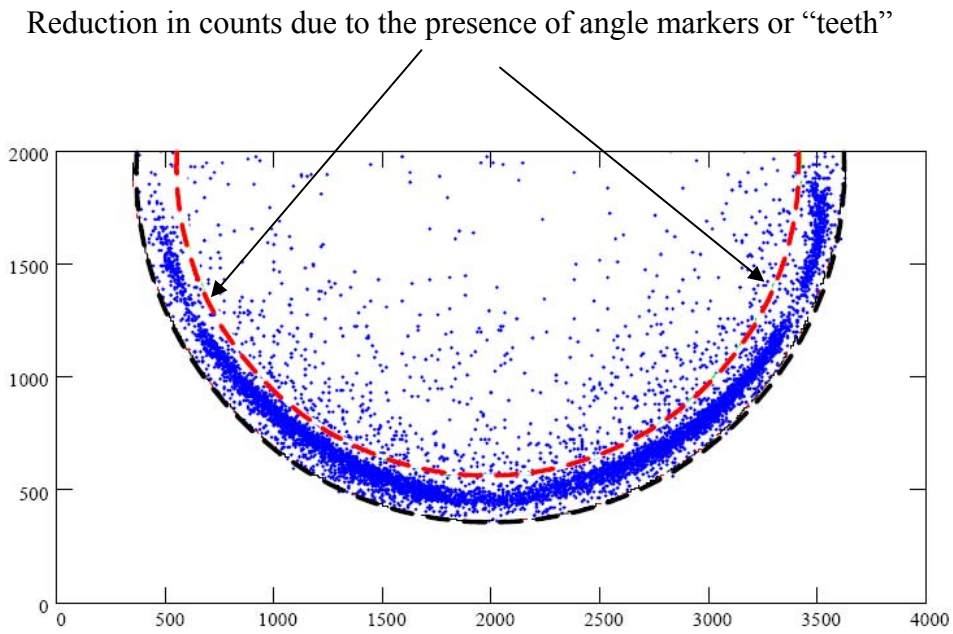

Fig 2 n: Typical images accumulated on the 180º detector over a short period of time. Two thin strips bridge (in the vicinity of 20º and 160º) the annular slit near the edges of the analyzer angular acceptance ranges. These serve as angle markers; their shadows are evident in the detected images

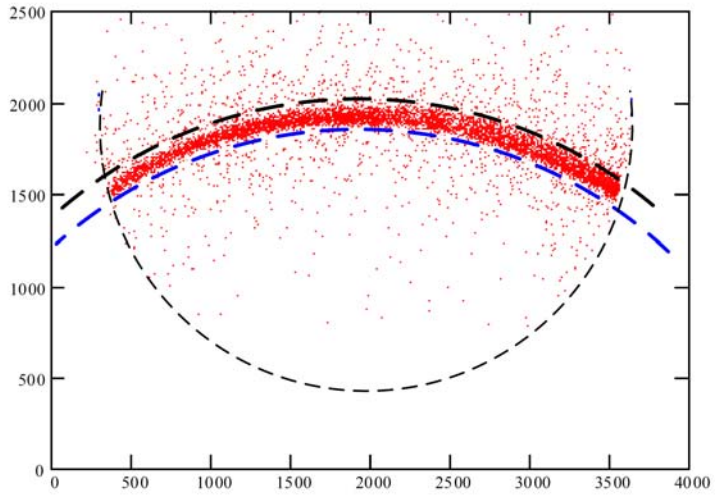

Fig 2 o: Typical images accumulated on the 100º detector over a short period of time. The sharp image within the annular ring (shown by dashed lines) is radially filtered. Due to mechanical restrictions, the smaller dimensions of the MCP limit the angular range of the images to ~ 60º.

2.3 REFERENCES

[1] Reddish T J, Richmond G, Bagley G W, Wightman J P and Cvejanović S 1997 *Rev. Sci. Instrum*. **68** 2685-92

[2] Hufner S 2003 *Photoelectron Spectroscopy: Principles and Applications* (Springer)

[3] Toffoletto F, Leckey R C G and Riley J D 1985 *Nucl Instrum Methods Phys Res* B **12** 282

[4] Read F H, Comer J, Imhof R E, Brunt J N H and Harting E, 1974 *J. Electron Spectrosc Relat Phenom* **4** 293

[5] Harting E and Read F H 1976 *Electrostatic Lenses* Elsevier

[6] Leckey R C G 1987 *J. Electron Spectrosc Relat Phenom* **43** 183

[7] http://www.phys.ksu.edu/personal/sroland/Detector.htm

[8] http://www.sciner.com/MCP/MCP.htm

CHAPTER 3: DATA ACQUISITION AND PROCESSING

3.1 INTRODUCTION

3.2 COMPUTER AUTOMATED MEASUREMENT AND CONTROL (CAMAC)

3.3 DATA COLLECTION MODES

3.3.1 NON COINCIDENCE DATA COLLECTION MODE

i. ANGLE INTEGRATED MAESUREMENTS

ii. IMAGES

3.3.2 COINCIDENCE DATA COLLECTION MODE

i. DATA ACQUISITION

ii. DATA PROCESSING

iii. COINCIDENCE STUDIES IN THIS WORK

3.4 CONCLUSION

3.5 REFERENCES

3.1 INTRODUCTION:

In this chapter the data acquisition system is described. Since, the apparatus was designed to be operated at the Daresbury Synchrotron Radiation Source (SRS),(UK) the interface between the hardware and the software is based around CAMAC interface (Computer Automated Measurement and Control) [1]. The data acquisition PC, a Pentium 120 MHz is based on Windows 95 operating system. The hardware functions adequately but requires an upgrade.

The spectrometer is a versatile apparatus that can be operated in either coincidence mode or non coincidence mode. Hence, the functionality and design of the data acquisition electronics has been set-up to support the wide range of possible experimental scenarios. Data acquisition details and subsequently data processing for various experimental scenarios involved in this work are presented. Non-trivial details on the processing of coincidence data briefly outlined.

3.2 COMPUTER AUTOMATED MEASUREMENT AND CONTROL (CAMAC):

CAMAC, a standard 24-bit data bus acts as an interface between the hardware and software. A number of electronic modules can be inserted into various slots (called a station) of the CAMAC crate such as ADC's (Analogue to Digital Convertors), DAC's (Digital to Analogue Convertors) and counters to be used simultaneously.

The CAMAC crate used here holds 25 stations, 24 of which are normal stations and one is a controller module. They are all connected to a common dataway or a back plane via edge connectors. Slots 24 (normal station) and 25 (controller station) are used for the controller module. A SI-8255 Singular Board was installed in the PC for CAMAC-PC communications and it communicates with the CAMAC Controller Module via 40-way ribbon cable. The controller module acts as an interface between the other modules in the crate and the PC and addresses a module or modules based on the commands given from

the computer. Further details of the CAMAC system can be found in the thesis of Wightman, 2002 [2]. The schematic mapping the spectrometer between the data acquisition electronics and software is shown in Fig 3 a.

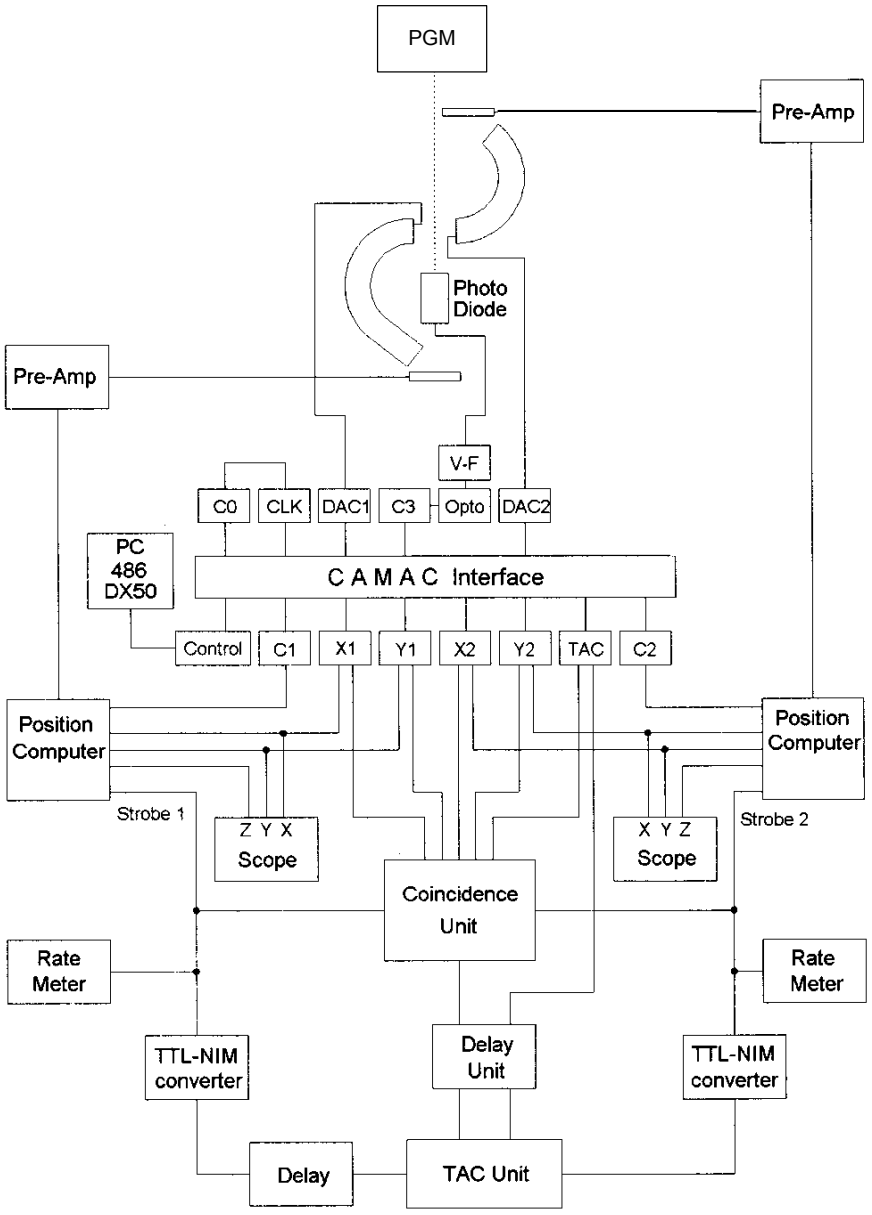

Fig 3 a: A current schematic of the processing electronics and computer interfacing operational at the Canadian Light Source (CLS) VLS-PGM end station. C*n* = counters, CLK=clock pulse, V-F + Opto = floating electrometer, voltage-to-frequency converter, and opto-isolator photon flux monitoring system.

3.3 DATA COLLECTION MODES:

As mentioned in Chapter 2, Sec 2.2.7, each analyzer has a dedicated position sensitive detector (PSD). The detectors can be used to collect data individually (non-coincident) or simultaneously. Using them simultaneously can be either for a single coincidence study or for two individual non-coincident measurements. In this section, the experimental scope of the apparatus and various possible data collection modes will be discussed.

3.3.1. NON COINCIDENCE DATA COLLECTION MODE:

i. ANGLE INTEGRATED MAESUREMENTS:

For angle-integrated measurements, the positional information is neglected as one only needs count rates or angle integrated measurements. The TTL "strobe" pulse from each detector is fed into the Kinetic Systems 3640 CAMAC counter input named C1 and C2 in Fig 3 a.

This mode is used for spectroscopy studies where one is interested in the count rates from a particular event, one can exclude the positional (*x,y*) information and only use the TTL pulses from the detector. Spectra can be collected individually using one detector only or simultaneously using both the detectors. During this work, the non-coincident spectra that was collected using this spectrometer was, namely:

Photoelectron Spectroscopy (PES) and Photoion Spectroscopy (PIS)

In PES and PIS [3] studies the photon energy is kept fixed and the detection energies of the toroidal analyzers are scanned across the desired energy region. If the analyzers are used to detect electrons, then the study is a PES and if ions are detected it a PIS study. In principle, the analyzers can be used individually or simultaneously for these studies. PES and PIS studies of O_2 can be found in Chapter 4.

Constant Kinetic Energy Spectroscopy (CKES) or Residual Energy Spectroscopy (RES)

For CKES studies, the toroidal analyzer detection energies are kept fixed and the photon energy is scanned across the desired energy region. Two types of CKES can be performed; one is the Constant Ion Kinetic Energy Spectrum (CIKES) where the photon energy is scanned over a fixed ion energy and Constant Electron Kinetic Energy Spectrum (CEKES) where the photon energy is scanned over fixed electron energy. The details about this study are presented in Chapter 5. TTL pulses from the TTL strobe unit for each detector is fed to the timing unit of the VLS PGM endstation that is connected to a LINUX based computer which displays the count rates and photon flux as a function of photon energy. Here again, one can perform these studies using either one or both the analyzers.

Threshold Photoelectron Spectroscopy (TPES)

In the TPES mode, one of the analyzers is tuned to detect near-zero energy photoelectrons, while the photon energy is scanned. The analyzers can be tuned to detect virtually "0 eV" (< 5 meV) electrons using field penetration technique [4]. Since electrons of "0 eV" are detected as the photon energy is scanned, each ionic state is being excited at its "threshold", hence the name TPES. Details about this experimental technique are given in Chapter 4, sec 4.2.1. In this mode, although the *x,y* information from the detectors is not used, it is useful however to use the live images on the scope for effecting tuning. The spectrometer has been successfully used to perform TPES studies of Ar, He, Kr and Xe [5, 6, 7].

ii. IMAGES

The images when recorded are shaped in the form of circular arcs, where in each positional point displayed on the oscilloscope corresponds directly to the initial angle of emission. The data acquisition set up for this mode is given under the section titled angle-

resolved counting. The energy resolution is determined to be 1% of the toroidal pass energy as per the spectrometer design. The toroidal geometry and the focusing properties of the electron lenses impact the angular resolutions of the images. The helium photodouble ionization (PDI) study by Wightman *et al* [2] determined the angular resolution be $\pm \approx 2.5°$. For calibration purposes in case of single photoionization, the angular distribution for the He^+ $n = 1$ state is well documented and is one of several appropriate standards, as it has a β parameter of 2 for all photoelectron energies.

Angle-resolved counting:

In this mode the detector images are recorded. As seen in Fig 3 b the (x_1, y_1) positional information corresponds to one of the detectors and (x_2, y_2) to another. The position information (x,y) for every count is fed to the Quantar positional computers. The analogue pulses from the positional computer are digitized using the Borer 1245 module, which is a Analogue to Digital Convertor (ADC). The digitized images have a 12-bit resolution per count with a 256 buffer limit.

One could study the angular distribution (i.e. β parameter studies**)** of photoelectrons/ions as a function of photon energy. We demonstrate the use of the spectrometer for the single photoionization study of H_2 in the Chapter 5, where the apparatus has been used for this experimental scenario. Here, only the positional information has been recorded as a function of the charged particle energy while keeping the photon energy fixed.

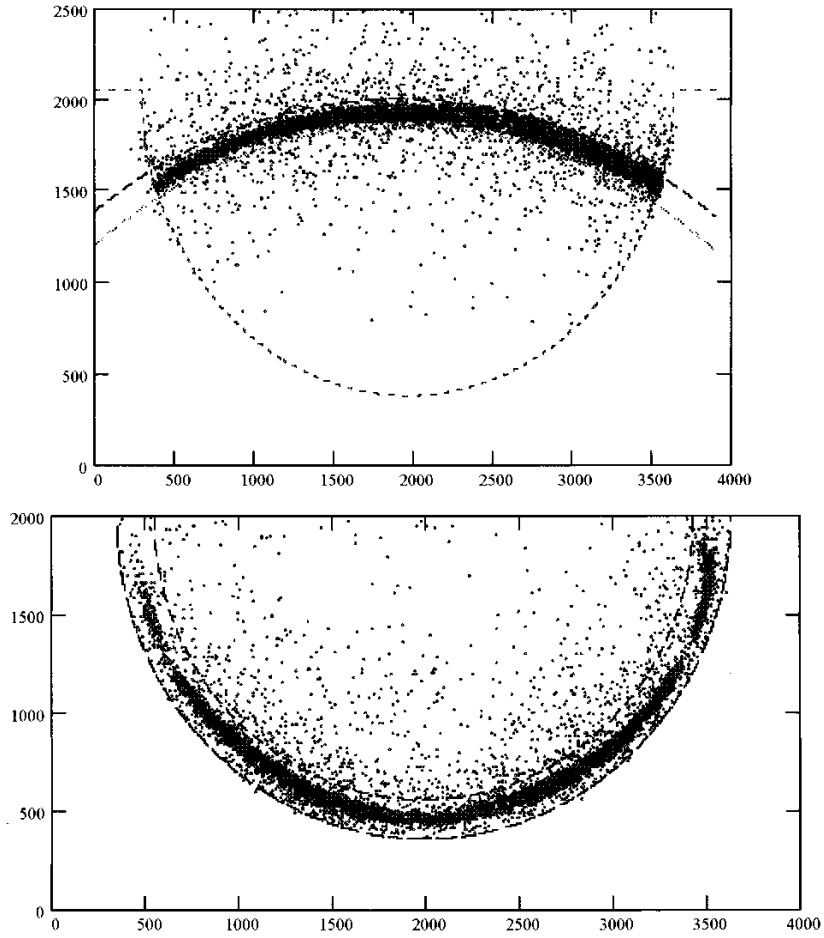

Fig 3 b: Recorded angle dispersed and energy resolved photoelectron images from the 100º analyzer (Top) and the 180º analyzer (bottom). The efficiency on the angular range of the images (minimal edge effects) is checked by the presence of angle markers around 20º and 160º in the 180º analyzer. As seen in the image of the larger analyzer, the lack of intensity in the vicinity of around 20º and 160º is due to the presence of the angle markers.

3.3.2. COINCIDENCE DATA COLLECTION MODE:

In a coincidence event one studies the dynamics of two outgoing charged particles produced by the same ionizing event. In order to achieve this one needs to gather not only the *x,y* positions of the two outgoing particles but also the timing information.

i. DATA ACQUISITION

In this mode, the (*x,y*) information as well as the timing information from the TTL strobe unit is derived from the QT3394 resistive anode encoder unit. As shown in schematic (Fig 3.1), the TTL pulses from the strobe units are fed into the LeCroy 222 module, which is a TTL-to-NIM converter. The converted NIM pulses are then fed into the Tennelec TC862 module, which is a Time to Amplitude Converter (TAC). Each detector has a dedicated NIM and TAC unit. A valid TAC output implies a corresponding (*x,y*) positional information. Since, the timing pulses are processed much sooner than the positional information, delay units are connected to the TAC units. A coincidence unit gates the positional information in correspondence with the TAC signal, filtering out any uncorrelated event. TAC pulses and positional information from the coincidence unit corresponding to a "coincidence" event are then sent to ADC modules. Five modules are required for this, one module each for each coordinate of the positional information from both the detectors i.e. (x_1,y_1) (x_2,y_2) and one unit for the timing information within the preset window(ΔT) for each coincidence event.

ii. DATA PROCESSING

The images obtained are in (*x,y*) coordinates and are converted to polar coordinates (r, θ) in the analysis software. In the subsequent analysis procedure, radial filtering (Fig 3 c) is applied to remove the electrons outside an annular ring that is centered on the sharp image. Time filtering is used to subtract ''random'' events from under the coincidence peak.

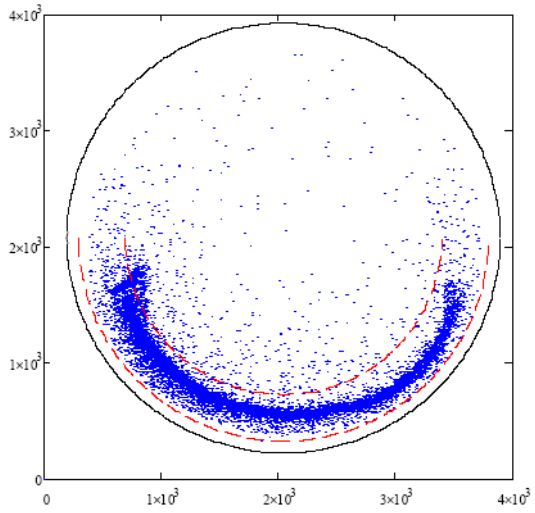

180º Analyzer

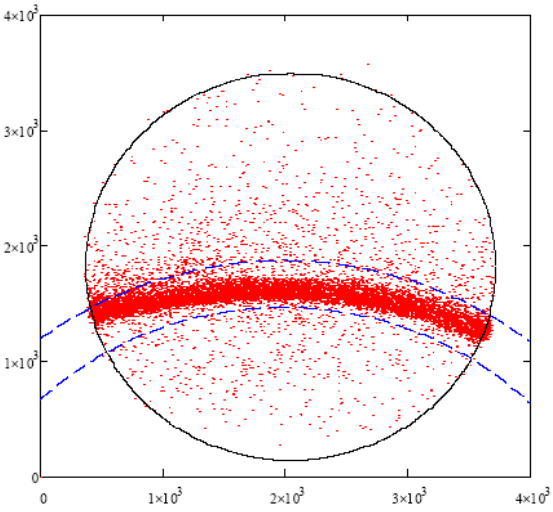

100º Analyzer

Fig 3 c: Angle dispersed photoelectron images that are radially filtered. The inner and outer radii (red dashed lines for the 180º analyzer and blue dashed lines for the 100º analyzer) for radial filtering are chosen to filter out the background.

Seen in Fig 3 d is a TAC spectrum obtained for a preliminary study of helium photodouble ionization where the electrons detected were for equal energy sharing condition of 25 -25 eV.

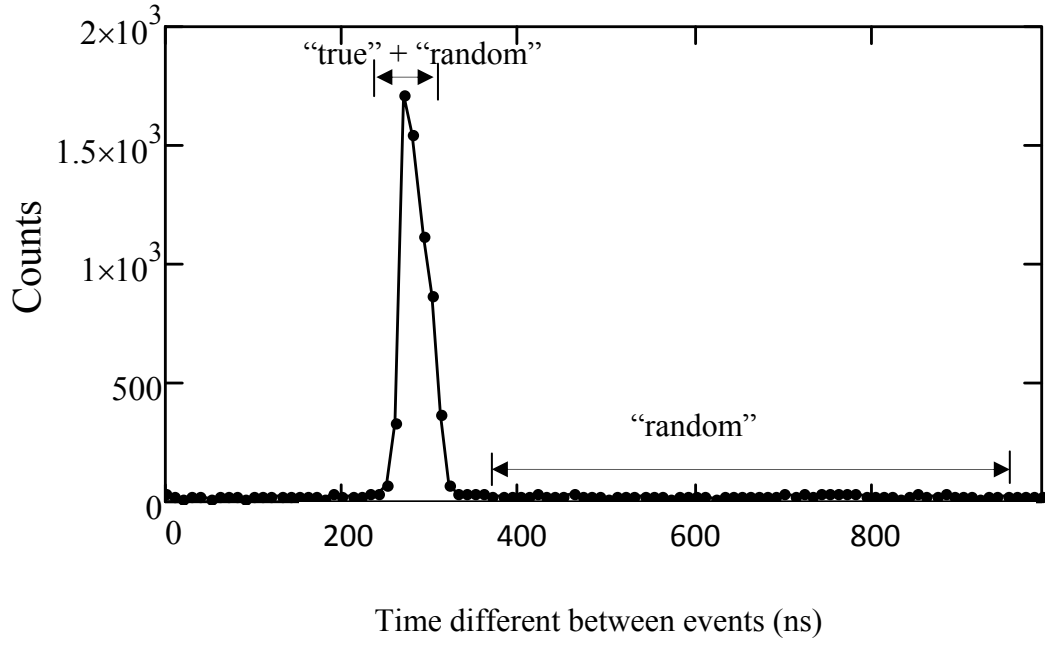

Fig 3 d: A sample TAC spectrum of the time distribution of coincident events for 25 -25 eV electrons in helium, integrated over the acceptance angles of both analyzers. The "true" coincidences and "random" coincidences obtained during the time delay between start and stop inputs on the time to amplitude converter is shown.

The "random" coincidences which are seen in the spectrum presented in Fig 3 d as background, is due to events with random timing i.e. events that are not correlated in time however that occur within the total TAC spectrum. A "true" coincidence signal implies that the electrons detected are correlated in time i.e. arising from the same ionizing event. The peak seen in the Fig 3 c to "true" coincidence signal, however since it is not background subtracted it is referred to as "true" + "random" peak.

A "true" coincidence is where the (x,y) information from both the detectors are correlated in time, hence implying that (x_1,y_1) and (x_2,y_2) are from the same ionization event. The spectrum accumulation time during the experiment is always set to a broader time window to cover the "true" coincidence peak as well as the background region. The

"true" + "random" time window for the obtained spectrum is set in data analysis (as seen in Fig 3 c), the background or the "random" window is also set in the analysis program.

In coincidence experiments the ratio of "true"+"random" to "random" coincidences is considered as the most serious limitation. The time window Δt_{random} corresponds to width the random events in Fig 3 c and $\Delta t_{true\ +random}$ corresponds to the total width of the coincidence peak without the background subtraction. The "random" window is always chosen to be 6-10 times greater than the "true" + "random" window to minimize errors in background subtraction. Hence, $\Delta t_{random} = R^* \Delta t_{true\ +random}$; where R is the ratio of the window widths $\Delta t_{random} / \Delta t_{true\ +random}$. If, N_{random} corresponds to the number of counts within the random window and $N_{true\ +\ random}$ to the number of counts within the "true" +"random" window, then the true coincidence count N_{true} is given by:

$$N_{true} = N_{\ true+random} - \frac{N_{random}}{R}$$

The standard deviation for N_{true} is then given by:

$$\sigma_{N\,true}{}^{2} = \sigma_{N_{true+random}}{}^{2} + \frac{\sigma_{N_{random}}{}^{2}}{R^2}$$

Assuming Poisson statistics, where standard deviation is given by $\sigma = \sqrt{N}$:

$$\sigma_{N\,true}{}^{2} = N_{\ true+random} + \frac{N_{random}}{R^2}$$

Hence,

$$\sigma_{N\,true} = \sqrt{N_{\ true+random} + \frac{N_{random}}{R^2}}$$

Thus, it can be seen the quality of data is better for large values of R. Hence, R is generally chosen to be to the order of 10 to reduce statistical errors. Specific details on the statistical requirements for the time filtering procedure have been discussed by McCarthy and Weigold [6].

Now that the radial filtered images are correlated in time, the data is further processed in angular intervals that is chosen in accordance with the available statistics. Typically one chooses 5º or 10º intervals. By integrating over the specified intervals on the images obtained from the two detectors, angular distributions of the ‘‘true’’ coincidences is created.

The “raw” (uncorrected) coincidence angular distributions can be further processed by efficiency corrections i.e. if a known angular distribution exists for the corresponding energy. This is due to the fact that the electron trajectories responsible for each data point in the measured angular distribution are unique. Variation in the yield as a function of angle arise from, for example, local electric field irregularities, mechanical differences (e.g. mechanical tolerances and minor misalignment), and microchannel plate gain variations. Similar to the measured energy scales in a photoelectron spectrum (PES) needing to be calibrated with a feature of known energy, the angular distributions also need to be calibrated to a reliable standard. For instance, it is common practice to use He^+ *n=1* or *n=2* beta functions as correction functions for suitable electron energies as these are well documented studies [e.g.: 7,8,9 and references there in].

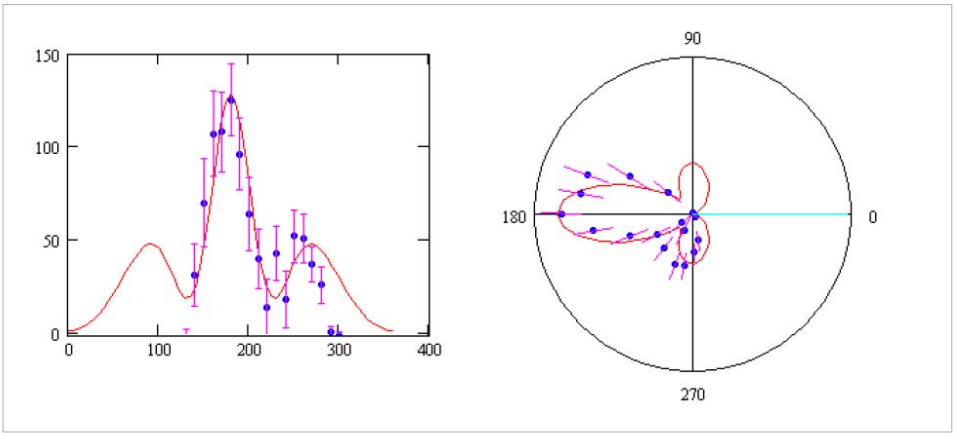

Fig 3 e: Preliminary results of the Triple Differential Cross Section (TDCS) for helium PDI study under asymmetric energy sharing condition with excess energy of 50 eV. The PDI threshold of helium being 79 eV, the 180 º analyzer was chosen to detect 42.5 eV electrons and the 100º analyzer to detect 7.5 eV. The figure shows angular distribution of electrons detected by the 180º analyzer correlated to electrons at 0º of the 100 º analyzer. The experimental data points plotted in 10º intervals are in agreement with the theory (red line) provided by J. Colgan using Time Dependent Close Coupling (TDCC) method [10].

iii. COINCIDENCE STUDIES IN THIS WORK

Angle resolved Photodouble Ionization (PDI) studies:

In a Photodouble Ionization (PDI) process the incoming photon ionizes the target resulting in the ejection of two electrons. Shown below is a process equation of direct PDI in case of an atom:

$$h\nu + A \longrightarrow A^{++} + e^- + e^-$$

The photon energy for such an experiment is kept fixed and the toroidal analyzers are tuned to detect the electrons of various energies within their resolving bandwidth such

that the total available energy is conserved. The apparatus has been previously used to study Photodouble Ionization (PDI) processes in helium, H_2, D_2 [e.g.:7, 8, and 9]. These studies were done under equal energy sharing conditions, the angular distribution of the electrons describe the correlation between the two electrons. Electrons arriving on one detector can be correlated with electrons arriving anywhere on the other detector. Hence, one can measure the independent angular distributions i.e, Triple Differential Cross Sections (TDCS) simultaneously. Although the mutual toroidal orientation is fixed, the toroids can be rotated around the photon beam axis so that the complete TDCS can be mapped as a function of the emission angle of one electron on the other toroid. A PDI study for asymmetric energy sharing conditions in helium was performed during the initial commissioning of the spectrometer at the Canadian Light Source [11] and seen in Fig 3 e are the preliminary results from that study.

Threshold Photoelectron Photoion Coincidence (TPEPICO):

In the **TPEPICO technique** coincidence between a "threshold" photoelectron (zero energy electrons) and a photoion from the same ionizing event is measured. We have used the TPEPICO technique [12] (presented in Chapter 4) where, for a fixed photon energy, one of the toroidal analyzers was tuned to detect photoions and the other analyzer was tuned to detect threshold photoelectrons using field penetration technique [4]. The kinematics of the analyzer and the photon energy was chosen to be able to study the dissociative photoionization (DPI) process of the $c^4\Sigma_u^-$ state in O_2^+. One could also in principle perform ion-electron coincidence studies for molecular systems such as the MFPAD (Molecular Frame Photoelectron/ion Angular Distribution) technique [13], where the electrons are both energy and angle resolved.

3.4 CONCLUSION:

In the past, the toroidal spectrometer has been successfully used for angle resolved PDI studies of He [e.g. 14] and TPES studies of He, Ar, Kr and Xe at the Daresbury SRS (Toroidal Grating Monochromator) [5,6,7]. Notably, Triple Differential Cross Section Measurements (TDCS) for PDI of D_2 were also made at the Daresury SRS [15]. In addition, TDCS studies, of He using left and right circularly polarized light were undertaken at the Photon Factory, Japan [16].

The spectrometer is currently housed at the VLS-PGM (undulator) beamline at the Canadian Light Source, Saskatoon a third generation synchrotron facility. Measurements made in a third generation facility using linearly polarized light have improved photon energy resolution and high flux. With the advantage of linearly polarized light source one can use the angle dispersive and energy-resolving capability of the spectrometer to study photoionization processes in atoms and molecules with improved efficiency. So far, we have employed the TEPIPCO technique to study the DPI process in O_2 $c^4\Sigma_u^-$ state [12] and more recently electron and ion β measurements have been made in H_2 to study the interference effects between Q_1 and Q_2 doubly excited states [17]. Such measurements require a spectrometer with an energy resolution suitable to study the variance in electron/ion angular distribution in closely spaced energy intervals. In future, experiments using techniques such as the MFPAD technique are being proposed.

3.5 REFERENCES:

[1] Scheetz R A and LeVine M J 1987 *IEEE Transactions on Nuclear Science* **34** (4) 1033-1035

[2] Wightman PhD thesis 2002 The University of Newcastle Upon Tyne

[3] K Ellis PhD Thesis 1991 University of Manchester

[4] Cvejanović S and Read F H 1974 *J. Phys. B: At. Mol. Phys.* **7** 1180-92

[5] Slattery A E, Wightman J P, M A MacDonald, Cvejanovic S and Reddish T J 2000 *J. Phys. B: At. Mol. Opt. Phys.* **33** 4833

[6] McCarthy I E and Weigold E 1976 *Phys. Rep*. **27** 275

[7] Wightman J P, Cvejanović S and Reddish T J 1998 *J. Phys. B: At. Mol. Phys.* **31** 1753-64

[8] Briggs J S and Schmidt V 2000 *J. Phys. B: At. Mol. Opt. Phys.* **33** R1

[9] Wehlitz R, Langer B, Berrah N, Whithfield S B, Viefhaus J and Becker U 1993 *J. Phys. B: At. Mol. Opt. Phys.* **26** L783

[10] Colgan J, Pindzola M S, and Robicheaux F 2007 *Phys*. *Rev*. *Lett*. **98**, *153001*

[11] Padmanabhan A, Thorn P, Reddish T J, Ryan C, Zuin L and MacDonald M A 2009 *Canadian Light Source Activity Report*

[12] Padmanabhan A, MacDonald A, Ryan C H, Zuin L and Reddish T J 2010 *J. Phys: B Mol. Opt. Phys*. **43** 165204

[13] Hikosaka Y. and Eland J.H.D. 2000 *Phys. Chem. Chem. Phys.***2**.4663-4668

[14] Cvejanovic S, Wightman J P, Reddish T J, Maulbetsch F, MacDonald M A, Kheifets A S and Bray I 2000 *J. Phys. B: At. Mol. Opt. Phys.* **33** 265

[15] Reddish T J, Wightman J P, MacDonald M A and Cvejanović S. 1997 *Phys Rev Letts* **79** 2438

[16] Collins S *et al* 2002 *Physical Review A* 2002 **65** 052717

[17] Reddish T J, Padmanabhan A, MacDonald M. A, Zuin L, Fernández J, Palacios A. and F. Martín 2011 *Phys*. *Rev*. *Lett* (submitted for publication)

CHAPTER 4: PHOTOIONIZATION STUDIES OF O_2

4.1 INTRODUCTION

In the dissociative photoionization (DPI) process, $h\nu + O_2 \rightarrow O + O^+ + e^-$, ionization and dissociation both occur (either as a direct or indirect process) following photoabsorption. The $c^4\Sigma_u^-$ predissociative state in O_2^+ at ~ 24.56 eV has a shallow minimum in its potential that supports two distinct quasi-bound vibrational levels (v = 0, 1). Dissociation in a molecule is always coupled with rotational effects; the rotational effects are negligible in cases where the ion dissociation is much faster than the rotation. In the $c^4\Sigma_u^-$ predissociative state, the vibrational levels have a finite lifetime before dissociating and these lifetimes τ_v, are distinctly different. The effect of a finite lifetime in a rotating dissociating molecule is a diminishing of the inherent anisotropic photoion angular distribution, characterized by a β parameter. The primary focus of this chapter is our investigation of the angular distributions of the 2 eV $O^+(^4S)$ produced from dissociative photoionization of O_2^+ $c^4\Sigma_u^-(v = 0, 1)$ using the Threshold Photoelectron Photoion Coincidence (TPEPICO) technique [47].

Also, being presented is the Threshold Photoelectron Spectrum (TPES) of O_2^+ between photon energy 20-25 eV. Threshold Photoelectron Spectroscopy of O_2^+ was mainly performed as a preliminary procedure in identifying the energy positions of the vibrational peaks in the $c^4\Sigma_u^-$ state. However, as a measure of completeness the other vibrational structures found between photon energy 20-25 eV are identified in this chapter and compared to earlier studies.

4.2 THRESHOLD PHOTOELECTRON SPECTROSCOPY

4.2. 1. EXPERIMENTAL TECHNIQUE

Threshold Photoelectron Spectroscopy involves photoionization processes where the photons ionize the target gas eventually leading to the production of "zero energy" electrons (< 5 meV). The incident photon energy is varied while the analyzer is tuned to extract zero energy photoelectrons. A TPES spectrum indicates the presence of an ionic state thus mapping out the energy levels of the ion states in the spectrum. Process equation indicating the production of threshold photoelectron for an atom:

$$h\nu + A \rightarrow A^{+} + e^{-} \text{ (direct process)}$$

This type of spectroscopy is generally associated with the field-penetration technique, whereby one uses a static electric field to extract over 4π sr electrons (see Fig 4 a) of energies smaller than a certain value (Cvejanovic and Read 1974). The high efficiency of the method is a great asset in detecting the many excited ionic states that have small cross sections.

The threshold analyzer response function depends critically on:

(i) The strength of the extraction potential

(ii) The 'pass energy' of the energy analyzer that is used to minimize the characteristic high-energy tail.

The extraction potential needs to be high enough to remove the slowest electrons over 4π sr without being too high so that faster electrons are not pulled out over a large solid angle. There will always be some energetic electrons traveling in the direction of the extraction optics and these are eliminated by an energy dispersive device – in this case a toroidal analyzer. The measured energy resolution in the threshold channel is 3.5 meV (FWHM) using He^{+} (n = 1) at 24.586 eV, (see Fig 4 b). To determine the overall energy resolution the photon beam resolution also has to be taken into account. The photon beam resolution was estimated as 1.8 meV (FWHM) by fitting the rising edge of the He^{+} (n = 1) TPES peak to a Lorenzian curve.

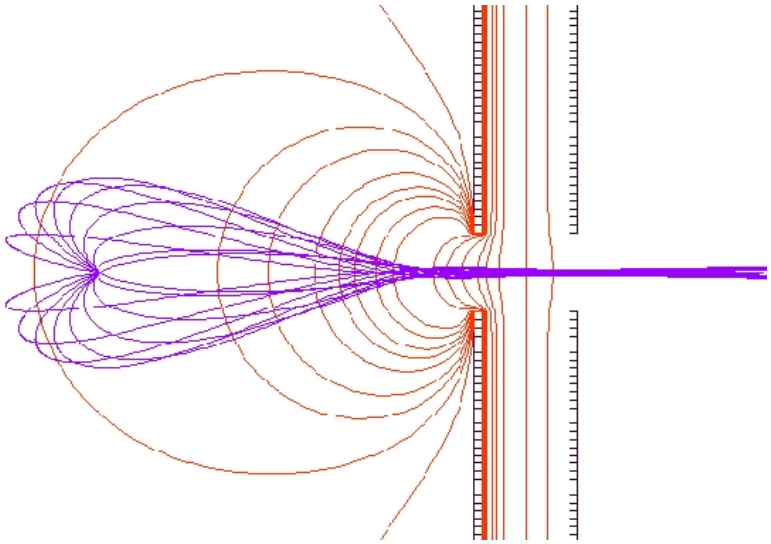

Fig 4 a: Trajectories of 0.001eV electrons emitted over 4-π sr from a point source can be focused and collimated by the *weak* electric field from an "extractor" electrode that penetrates through the 0 Volt aperture. The solid angle of extracted, faster electrons is significantly smaller than for these "threshold" electrons and rapidly diminishes with electron energy. This highly-efficient, energy selective extraction allows one to perform "threshold electron spectroscopy".

The threshold peak as seen in Fig 4 b has a characteristic sharp rise in the lower photon energy end of the peak; the sloping background in the vicinity of the rising edge is attributed to effects from the Blackbody radiation. Room temperature infrared(IR) photons emitted due to the Blackbody effect, lead to the ionization of high *n* Rydberg helium atoms that are photoexcited and long lived, resulting in the production of photoelectrons as seen in Fig 4.c, before reaching the *n*=1 ionization threshold.

$$h\nu\,(\mathrm{IR}) + \mathrm{He}^{++} \rightarrow \mathrm{He}^{+}\,(n{=}1) + \mathrm{e}^{-}$$

The sharp rise in the yield of threshold photoelectrons is directly correlated to the efficiency of the extraction potential, the solid angle of extracted, faster electrons is significantly smaller than for these "threshold" electrons and rapidly diminishes with

electron energy. The "tail" in the higher photon energy part of the peak corresponds to the gradual decrease in cross section of faster photoelectrons as photon energy moves away from the threshold of an ionic state. The "tail" seen in Fig 4 b is suppressed by the toroidal analyzer; it is characteristic of threshold analyzers that the observed peak shapes are asymmetric. Thus the characteristic threshold peak shape is a convolution of the energy profiles of the photon beam and the threshold analyzer.

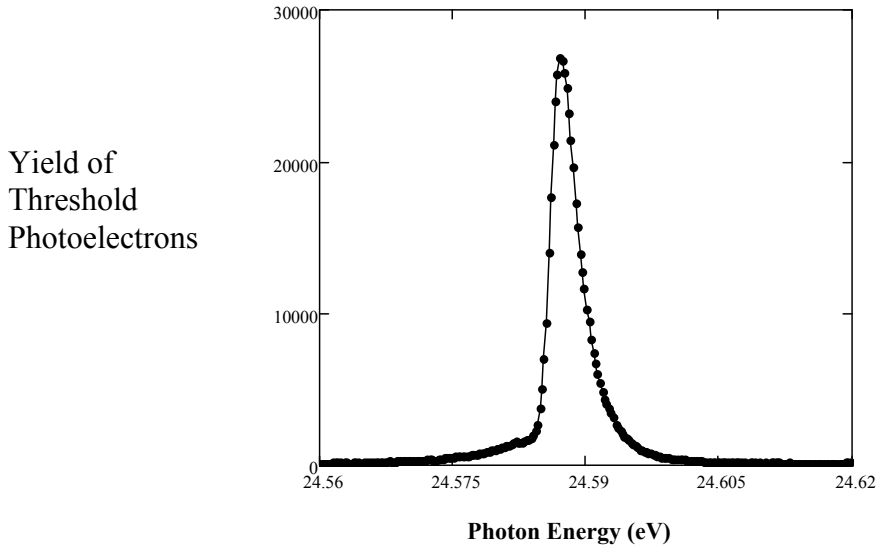

Fig 4 b: TPES of Helium;He^+ n=1 peak at 24.586 eV.

The smaller of the two toroids of the Toroidal Spectrometer was tuned to detect threshold electrons. In order to calibrate the threshold detection efficiency, the toroid was first tuned to detect helium threshold electrons. Fig 4 c shows the TPES of helium ranging between photon energy 77.8 eV and 79.4 eV. Also seen in Fig 4 c is the characteristic "cusp-like" feature at photon energy 79 eV, which is the double ionization threshold for helium. This feature is a well studied signature of helium TPES and was first predicted by the Wannier model (Wannier 1953, Read 1985) [55, 56]. As seen in Fig 4 c, as one approaches the double ionization threshold, there is a slightest but distinct dip in the threshold electron yield at 79 eV. This characteristic cusp is the manifestation of electron-electron correlation that dominates low energy electron yield in this region. At the double ionization threshold two "zero" energy electrons are ejected, however, the

coulomb interaction between the two electrons results in both the electrons not being released.

The double ionization region in helium continues to be the subject of intense interest [48-54], since it is the archetypal electron correlation system. It is noted, in passing, that the ratio of the threshold yield immediately below and above 79 eV is ≈ 1.08, in good agreement with earlier studies [49, 51, 54] obtained with ~ 70 meV resolution and still at variance with the ≈ 1.25 value from [53].

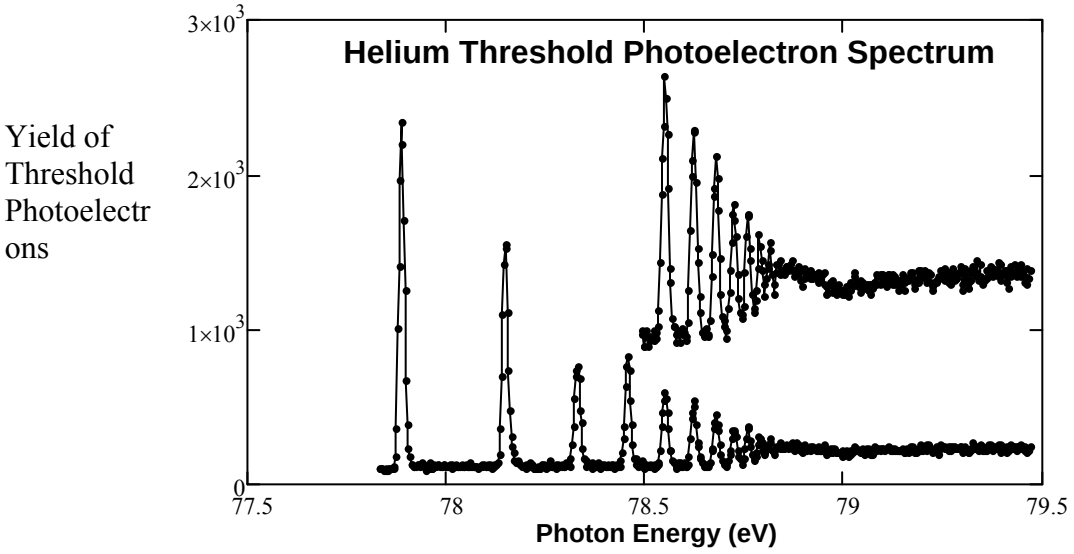

Fig 4 c: Threshold photoelectron spectrum (TPES) of Helium. Insert: The slight dip in the threshold yield at 79.0 eV is the characteristic "cusp" [16,18] at the double ionization threshold energy.

4.2. 2. TPES OF O_2 (20- 25 eV)

Fig 4 d shows an overview of the TPES of O_2 spanning between 12-50 eV from [18]. The orbital configuration of the molecular ground state of O_2 molecule is:

$$(1\sigma_g)^2(1\sigma_u)^2(2\sigma_g)^2(2\sigma_u)^2(3\sigma_g)^2\ (1\pi_u)^4(1\pi_g)^2 X^3\Sigma_g^-$$

The main ionic states between photon energy 20-25 eV are the $B^2\Sigma_g^-$ and $c^4\Sigma_u^-$ states.

The $B^2\Sigma_g^-$ state between photon energy 20-21 eV (see Fig 4 e) is formed by the ejection of a single $3\sigma_g$ electron. We find the weak vibrational structure in the same energy region, which has been assigned as the $^2\Sigma_u^-$ state [33]. The $c^4\Sigma_u^-$ state arises from the ejection of a single $2\sigma_u$ electron. Our finding of the weaker and broader $v = 2$ vibrational level of the $c^4\Sigma_u^-$ state at 24.97eV is in agreement with the Photoelectron Spectroscopy (PES) study of Baltzer [35].

In addition to these two ionic states which dominate this energy region, we also support the findings of Ellis *et al*. [15] in their observations of series of vibrational structure between 21-24 eV. The structure in the first half of this energy region between 21-22 eV remains unassigned. The structure between 22-24 eV has been assigned as the $3^2\Pi_u$ state.

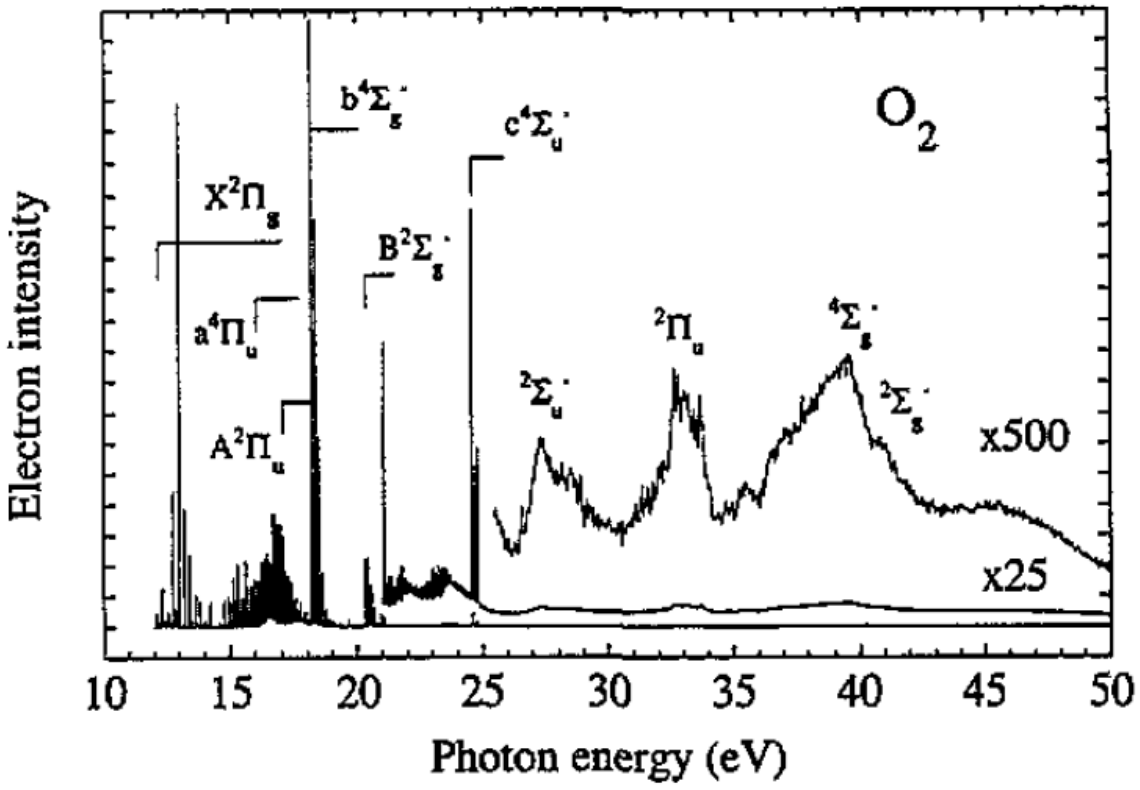

Fig 4 d: Showing the TPES of O_2 by Ellis *et al* [18], providing an overview of the ionic states between a wide energy range 12- 50 eV.

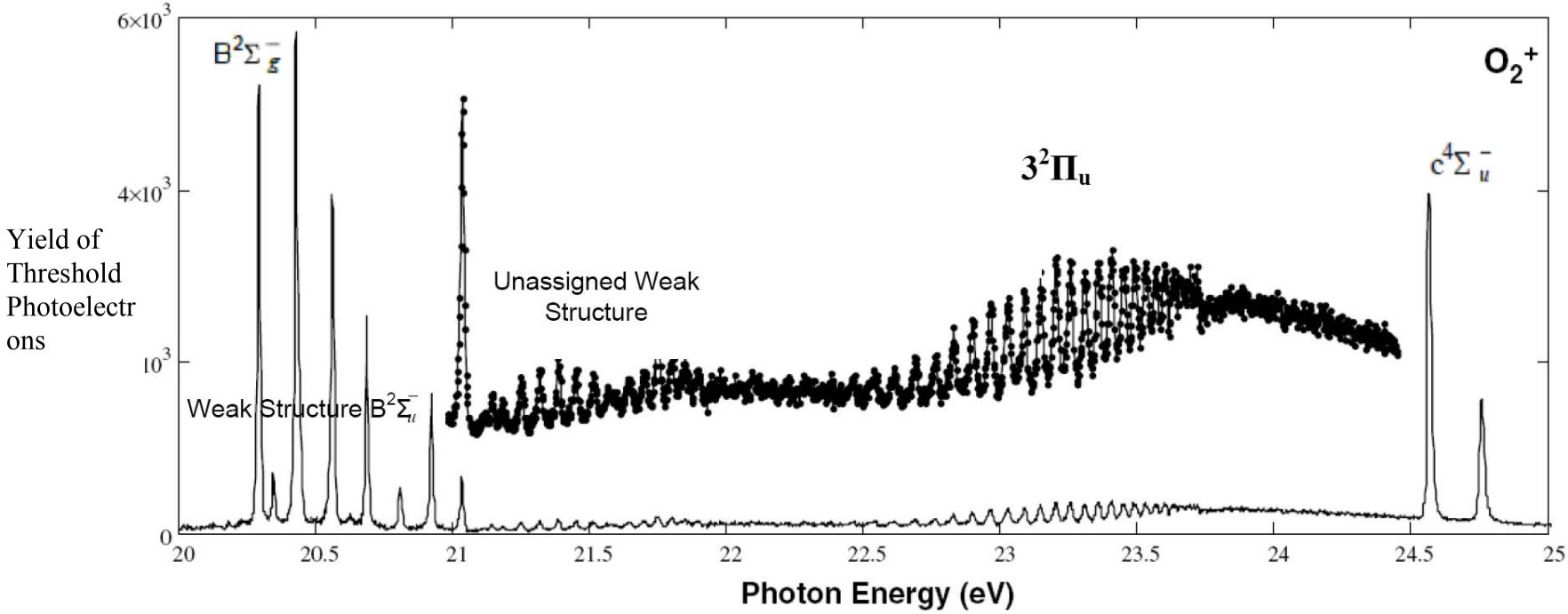

Fig 4 e: Overall Threshold Photoelectron Spectroscopy (TPES) of O_2^+ between photon energy 20-25 eV.

4.2.3. COMPARITIVE STUDY (THEORY AND EXPERIMENT)

$B^2\Sigma_g^-$ state (20- 21.1 eV)

Shown in Fig 4 f is a TPES of the $B^2\Sigma_g^-$ O_2^+ state between 20-21.1 eV. The study by Cafolla *et al* 1990 [42] states that the Rydberg states converging to this state decay mainly to the $b^4\Sigma_g^-$ state (~18.1 eV). Table 4.1 shows our observed values of the energy positions of the vibrational levels belonging to this state in comparison with the Photoelectron Spectrocopy (PES) study of Baltzer *et al* [45] and TPES study of Ellis *et al* [18].

Table 4.1 Vibrational Progression of $B^2\Sigma_g^-$ state

Vibrational quantum number (*v*)	Baltzer *et al (PES)* eV	Ellis *et al (TPES)* eV	This work eV	Vibrational Spacing (meV) Baltzer *et al*	Vibrational Spacing (meV) Ellis *et al*	Vibrational Spacing (meV) This work
0	20.296	20.298	20.294	137	136	136
1	20.433	20.434	20.430	130	134	133
2	20.563	20.568	20.568	127	124	124
3	20.690	20.692	20.692	122	122	123
4	20.812	20.814	20.810	116	116	115
5	20.928	20.930	20.925	112	112	111
6	21.040	21.042	21.036	106	108	108
7	21.146	21.150	21.144	103	-	108
8	21.249	-	21.252	99	-	95
9	21.348	-	21.347	-	-	-

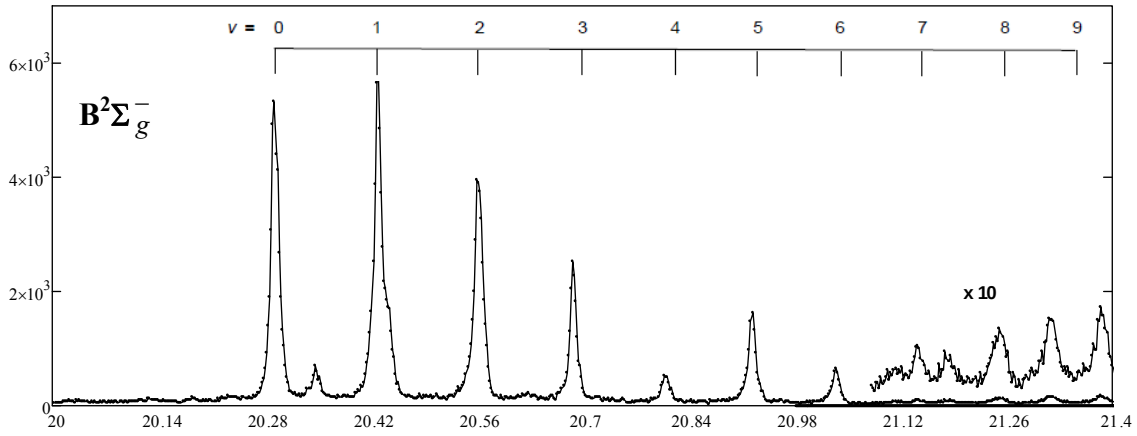

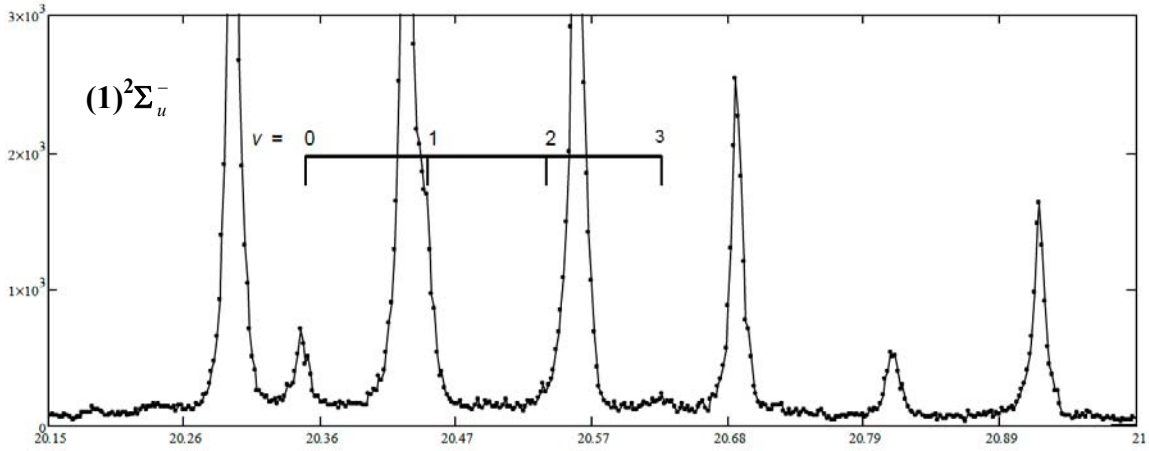

Fig 4 f: TPES of the O_2^+ $B\Sigma_g^-$ state showing the strong vibrational structure of $^2\Sigma_g^-$ state (Top) and weak structure of $^2\Sigma_u^-$ state (Below)

Weak Vibrational Structure - $B^2\Sigma_u^-$ state (20-21.1 eV)

Interspersed with the peaks of the $B^2\Sigma_g^-$ state, are weak peaks in the same region (see Fig 4 f). Our finding of this structure is consistent with TPES studies of Ellis *et al* [18], Tanaka *et al* [33] and PES study of Baltzer *et al* [35]. Based on their theoretical calculations, Baltzer *et al* assign this structure to the $2^2\Pi_u$ state, however fail to justify their interpretation. Ellis *et al*., affirm the findings of Baltzer *et al* stating that this ionic state is populated by direct ionization. The fact that the peak intensities resemble those of the PES study by Baltzer rule out a significant contribution from an indirect excitation process. In the study by Tanaka *et al* [33], they evaluate the energy at dissociation limit of this state to be 21.782 eV, which they state is near the third dissociation limit at 22.059 eV. The possible states that arise from this limit are $[\Sigma^-,\Sigma^+]_{g,u}$ states.

From obtaining the vibrational constant ω_e and the dissociation energy D_e and analyzing the rotational structure of this particular progression Tanaka *et al* arrive at the conclusion that this state is $^2\Sigma_u^-$. Their study is in agreement with the theoretical findings of Beebe *et al* [43] and Evans *et al* [16] who use the Born Oppenhheimer approximation, where the electronic, vibrational and rotational motions are separated out. Table 4.2 compares our observations with those of Baltzer and Ellis. Unlike Baltzer and Ellis we do not support their findings of a long vibrational structure beyond 20.63 eV.

Table 4.2: Vibrational Progression of the $^2\Sigma_u^-$ state

Vibrational quantum number (*v*)	**Baltzer *et al* *(PES)* eV**	**Ellis *et al* *(TPES)* eV**	**This work eV**	**Vibrational Spacing (meV) Baltzer *et al***	**Vibrational Spacing (meV) This work**
0	20.351	20.350	20.353	99	93
1	20.450	20.450	20.446	94	91
2	20.544	0.000	20.537	93	93
3	20.637	20.634	20.630	89	93
4	20.726	20.722	-	-	-
5	20.810	0.000	-	-	-
6	20.890	20.890	-	-	-
7	20.968	20.963	-	-	-

Unassigned Weak Structures (21-22 eV)

We also find two weak progressions of vibrational levels in the 21-24 eV range, in agreement with the findings of Ellis *et al* (see Fig 4 g). This region can be looked at as two similar structures that appear to converge to a limit before merging into a continuum. The structure in the first energy region between 21.2 – 22.2 eV was not observed in the PES study by Wills *et al* [44] or Baltzer *et al* [35]. However, contrary to the weak structure of the $^2\Sigma_u^-$ state discussed in the previous section, these structures were not observed in the PES studies, hence implying the role of an indirect process. It has been suggested by Ellis *et al* that this progression is a result of autoionization from Rydberg states converging to the $3^2\Pi_u$ state (22-24 eV). Supporting this line of argument is the similarity in the structure of the vibrational spectra of these weak peaks to those of $3^2\Pi_u$ state. Theoretical study by Takeshita *et al* [34] are in agreement with the experimental observations of Ellis and Wills [44] that autoionization to these states takes place through nonadiabatic coupling after excitation to the Rydberg states.

Table 4.3 lists the observed energies of these weak peaks in comparison to those observed by Ellis *et al.* It must be noted that there is some discrepancy between the two observations, hence requiring further high resolution TPES study in this region.

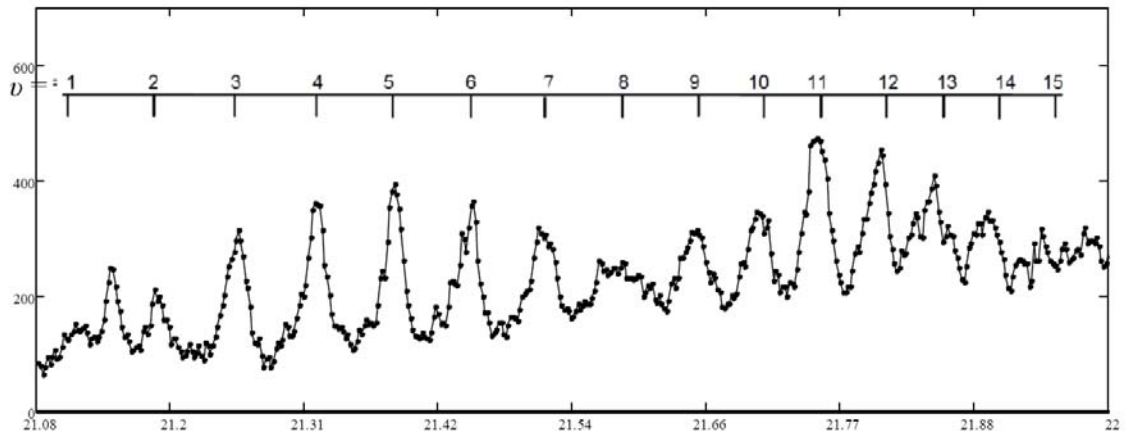

Fig 4 g: TPES of O_2^+ unassigned weak structure between 21-22 eV

Table 4.3: Unassigned weak structure between *hv* = 21-22 eV

Vibrational quantum number (*v*) (nominal)	Ellis *et al* *(TPES)* eV	This work eV	Vibrational Spacing (meV) Ellis *et al*	Vibrational Spacing (meV) This work
1	21.118	21.114	72	70
2	21.190	21.184	70	68
3	21.260	21.252	70	65
4	21.330	21.317	68	68
5	21.398	21.385	60	68
6	21.458	21.453	72	62
7	21.530	21.515	59	66
8	21.589	21.581	67	64
9	21.656	21.645	58	56
10	21.714	21.701	46	50
11	21.760	21.751	56	54
12	21.816	21.805	46	44
13	21.862	21.849	50	45
14	21.912	21.894	48	48
15	21.960	21.942		

$3^2\Pi_u$ state (22 – 24 eV)

Compared to the structure in the first region between 21 and 22 eV, the structure in the second region between 22-24 eV has been observed in PES study by Baltzer *et al* and also by Ellis *et al* in their TPES study. Baltzer *et al* assign the observed structure to a vibrational progression that belongs to $(1\pi_u)^3(1\pi_g)^2 3^2\Pi_u$ ionic state. Ellis *et al* assign this series as converging to the ion limit at 23.750 eV corresponding to dissociation products $O\ ^3P + O^+\ ^2P$. Wills [44] and Tanaka *et al* (2005) [34] in their theoretical study show that the vibrational levels of the $3^2\Pi_u$ state and the continuum of nuclear motion of the $(1)^2\Sigma_u^-$ state contribute to the broad peak of continuum between 22.5 and 26 eV. The edge at 23.75 eV arises due to the vibrations from the $3^2\Pi_u$ state merging into the broad continuum which exists between 23.7 and 26 eV (see Fig 4 e). The origin of this continuum has been attributed to the $(1)^2\Sigma_u^-$ state [34]. Table 4.4 lists the observed energies of $3^2\Pi_u$ state in comparison to those observed by Baltzer *et al* and Ellis *et al.*

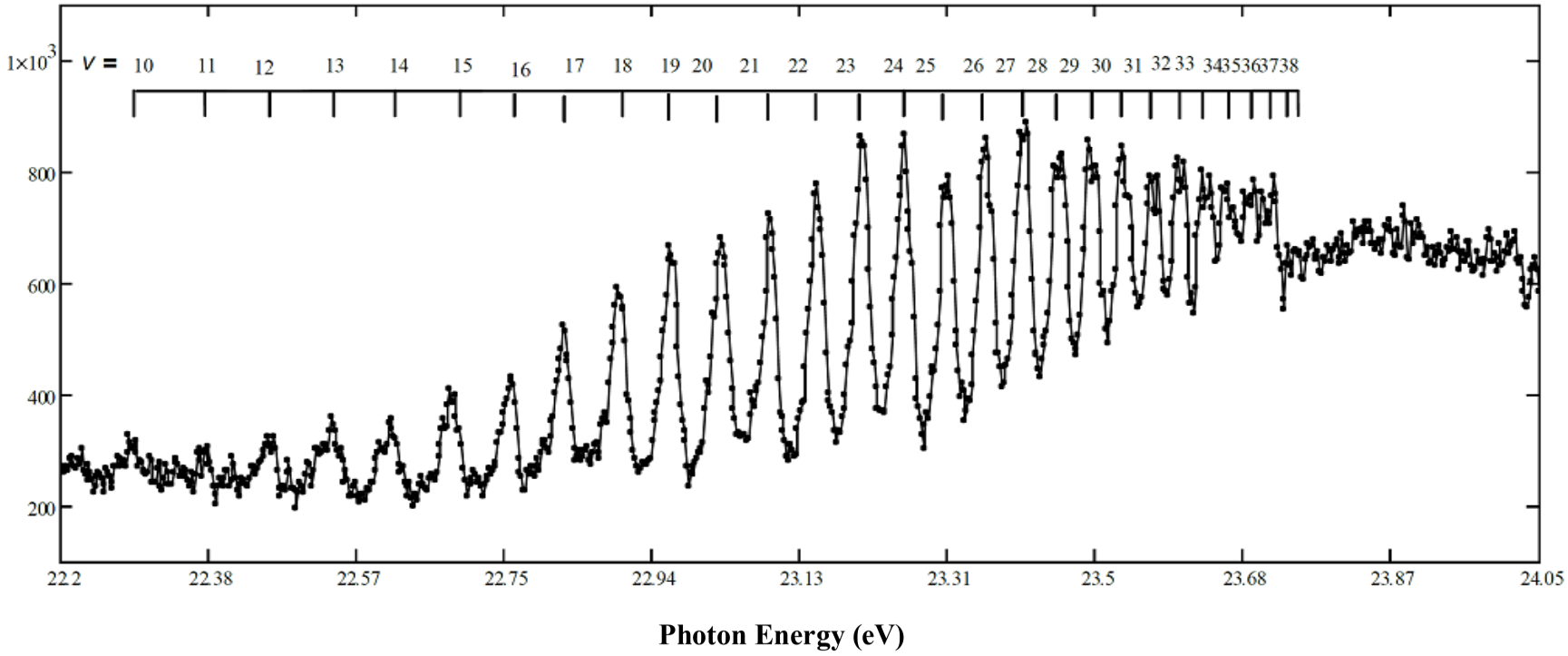

Fig 4 h: TPES of the O_2^+ $\mathbf{3^2\Pi_u}$ state between 22-24 eV

Table 4.4: Energy comparison of $3^2\Pi_u$ state between $h\upsilon$ = 22-24 eV

Vibrational quantum number (v)	Baltzer *et al (PES)* eV	Ellis *et al (TPES)* eV	This work eV	Vibrational Spacing (meV) This work	Vibrational Spacing (meV) Baltzer *et al*
10	22.300	22.300	22.290	90	93
11	22.393	22.392	22.380	80	68
12	22.461	22.472	22.460	77	77
13	22.538	22.544	22.537	74	78
14	22.616	22.622	22.611	76	68
15	22.684	22.692	22.687	76	79
16	22.763	22.766	22.763	68	70
17	22.833	22.838	22.831	68	67
18	22.900	22.906	22.899	66	65
19	22.965	22.968	22.965	62	64
20	23.029	23.030	23.027	62	62
21	23.091	23.094	23.089	57	57
22	23.148	23.152	23.146	58	57
23	23.205	23.210	23.204	52	52
24	23.257	23.262	23.256	52	52
25	23.309	23.316	23.308	50	52
26	23.361	23.362	23.358	48	47
27	23.408	23.410	23.406	46	44
28	23.452	23.454	23.452	40	42
29	23.494	23.492	23.492	42	40
30	23.534	23.534	23.534	36	38
31	23.572	23.572	23.570	32	30
32	23.602	23.606	23.602	32	36
33	23.638	-	23.634	30	26
34	23.664	-	23.664	24	25
35	23.689	-	23.688	21	19
36	23.708	-	23.709	27	24
37	23.732	-	23.736	11	-
38	-	-	23.747	-	-

4.2.4 CONCLUSION

In conclusion our observations of the vibrational progressions of the $B^2\Sigma_g^-$, $(1)^2\Sigma_u^-$, $3^2\Pi_u$ are in agreement with previous TPES and PES experimental studies.

However, we are in closer agreement with the PES study by Baltzer *et al* in terms of the energies levels of the observed peaks. This also remains true for our observations of the v= 0, 1, 2 vibrational levels of the $c^4\Sigma_u^-$ state, which will be discussed in-depth in the upcoming section.

4.3 DISSOCIATIVE PHOTOIONIZATION (DPI) OF O_2

4.3.1 INTRODUCTION

The dissociative photoionization (DPI) process of a diatomic molecule, the molecule is photoionized resulting in the formation of an atomic ion A^+, a neutral atom B, and an electron e^-, $h\nu + AB \rightarrow A^+ + B + e^-$ Dissociative photoionization (DPI) of O_2 between 20 and 28 eV has been recently explored in detail using electron-ion vector correlation methods, examining both the electron-ion kinetic energy correlation [9] and the molecular frame photoelectron angular distributions [10]. Fig 4 i shows the Threshold Photoelectron Spectra (TPES) of O_2 between 20-25eV that shows the various states and dissociative limits in this energy region. The focus of this section was on the $c^4\Sigma_u^-$ state in O_2^+ at ~24.56 eV (above the O_2 $X^3\Sigma_g^-$ ground state), which has a shallow minimum in its potential well that supports two distinct quasi-bound vibrational levels (ν =0, 1). This existence of such a strongly predissociative state partly explains why there have been numerous theoretical and experimental studies of the $c^4\Sigma_u^-$ state over the years. The vibrational levels of the $c^4\Sigma_u^-$ state in O_2^+ have distinctly different lifetimes, τ_v, due to predissociation, which reduces the state's inherent anisotropic photoion angular distribution for the non-rotating molecule. We have investigated the angular distributions of $O^+(^4S)$ ions produced from dissociative photoionization of O_2^+ $c^4\Sigma_u^-$ (ν =0,1) using the TPEPICO technique, i.e. by measuring the coincidence yield between threshold photoelectrons and photoions [47].

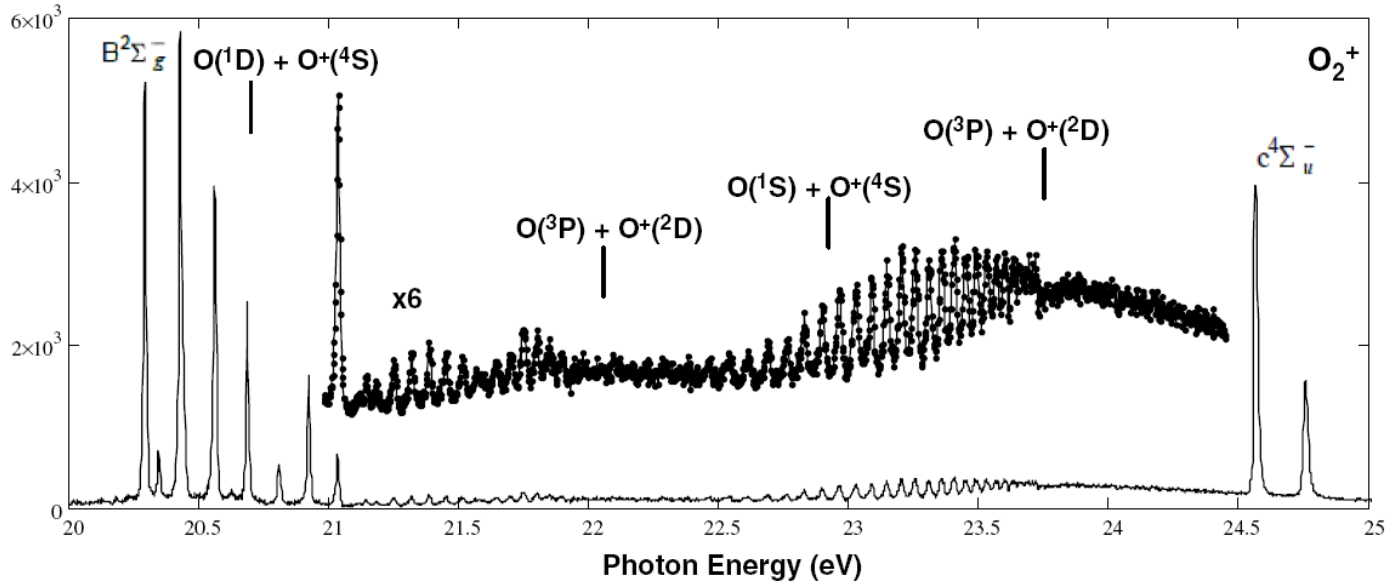

Fig 4 i.: The threshold photoelectron spectrum for O_2^+ between 20-25 eV taken with an accumulation time of 4 s per point, in 2 meV steps, and a vacuum chamber pressure of ~ $3x10^{-6}$ torr. The dissociative ionization limits L2-5 are indicated (see Table 4.5), as are the two most intense vibrational series: $B^2\Sigma_g^-$ and $c^4\Sigma_u^-$; the spectroscopy in this region discussed at length in [15, 33-37 and references therein].

4.3.2 THE $c^4\Sigma_u^-$ IONIC STATE

As seen in Fig 4 j at ~ 25 eV directly above the ground state ($X^3\Sigma_g^-$) is the predissociative state $c^4\Sigma_u^-$ that supports two distinct quasi-bound vibrational levels (ν=0, 1). The ν = 1 level dissociates almost exclusively to the $O(^1D) + O^+(^4S)$ dissociation limit (designated as L2 – see Table 4.5) at 20.700 eV [13-15]. The ν = 1 level's decay to the L2 limit is due to tunneling through the potential barrier and hence is short lived compared to ν = 0.

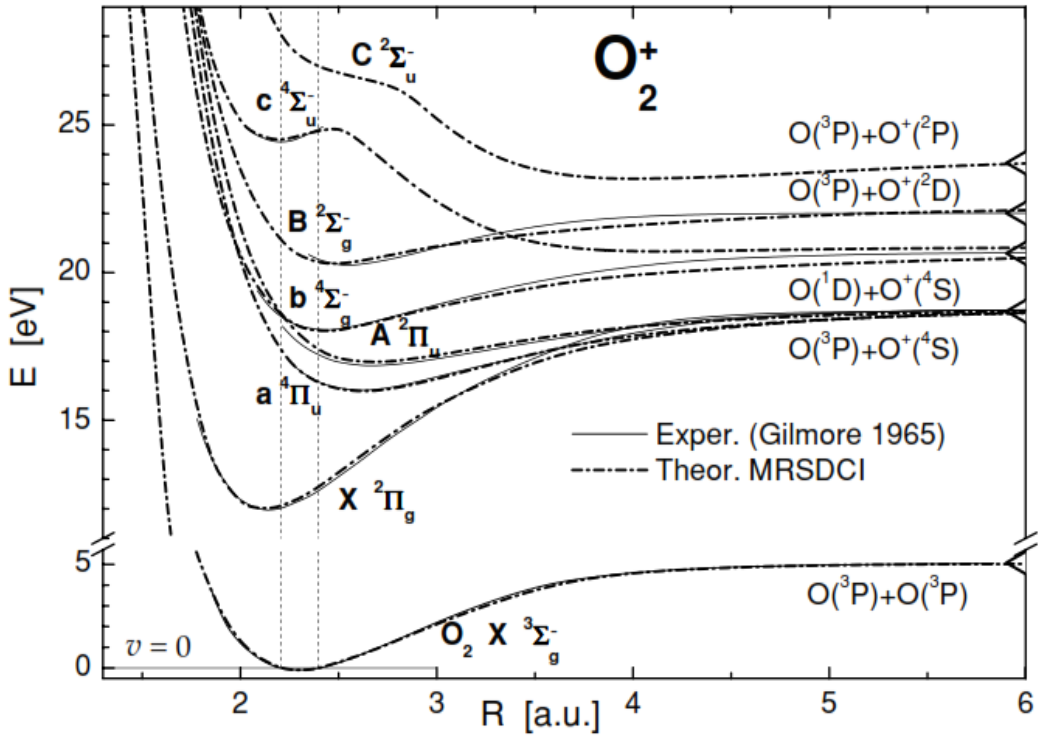

Fig 4 j: Theoretical and experimental potential energy diagram [25] plotted with various dissociation limits for relevant O_2^+ molecular states.

Table 4.5: Dissociation limits of $v = 0, 1$ vibrational levels of the $c^4\Sigma_u^-$ state.

Vibrational Level	Dissociation Products	Limits	Dissociation Energy (eV)
$v = 0$	$O\ ^3P + O^+\ ^4S$ (spin-orbit coupling)	L1	18.733
	$O\ ^1D + O^+\ ^4S$ (tunneling)	L2	20.700
	$O\ ^3P + O^+\ ^2P$ (continuum)	L5	23.750
$v = 1$	$O\ ^1D + O^+\ ^4S$ (tunneling)	L2	20.700

In contrast, the $v = 0$ level lives long enough to fluoresce to the $b^4\Sigma_g^-$ state [19, 20] and dissociative ionization competes with radiative decay. Two limits have been clearly established in the dissociative ionization channel, namely L1 and L2 (see Table 4.5) with a branching ratio of approximately 1:2 [13, 14, 20, 21]. Akahori *et al* (1985) [14] also find a weak L5 contribution (~5%) after subtracting L5 yield due to the underlying continuum, a background contribution that is also observed by [13, 15, 20]. Richard-Viard *et al* [20] conclude that decay to the (a) L2 limit occurs via tunneling and (b) L1 limit via spin-orbit coupling to the $^4\Pi_u$ state. They also quantify the O^+/O_2^+ ratio as 6 ± 1 for the $v = 0$ level; i.e. a ~15% fluorescence branching ratio.

4.3.3 ANISOTROPY IN A ROTATING DISSOCIATING MOLECULE

The vibrational levels have distinctly different lifetimes, τ_v, which diminish the inherent anisotropic photoion angular distribution for an ionic state characterized by a β parameter. Laboratory frame ion angular distributions are given by [Lafosse 10]:

$$\frac{d\sigma_{O^+}}{d\Omega} = \frac{\sigma_{O^+}}{4\pi}\left(1+\beta_{O^+}P_2(\cos\theta)\right) = \frac{\sigma_{O^+}}{4\pi}\left(1+\frac{\beta_{O^+}}{2}\left(3\cos^2\theta-1\right)\right) \qquad (4.2)$$

where θ is measured with respect to the polarization axis and is characterized by an asymmetry parameter, β_{O^+}, whose range lies between -1 and +2. Eqn (4.2) applies to photoionization processes, where electron ejection is much faster than rotation. We have to consider the effects of rotation in a dissociating molecule as this plays a role in diminishing the observed anisotropy.

We define the asymmetry parameter for a non-rotating molecule to be $\beta_{O^+}^T$, which is the inherent or natural asymmetry parameter. We define the measured asymmetry parameter β_{O^+} using the semi classical expression [45, 41]:

$$\beta_{O^+} = \beta_{O^+}^T\left(\frac{1+a^2}{4+a^2}\right) \qquad (4.3)$$

In Eqn (4.3), $a = 1/(\omega\tau)$, where ω is the rotational velocity of the molecular state and τ is its lifetime. When $\tau \to \infty$, $\beta_{O^+} \to \beta_{O^+}^T/4$ and as $\tau \to 0$, $\beta_{O^+} \to \beta_{O^+}^T$, thus the effect of rotation is to reduce the inherent asymmetry parameter.

However, it is to be noted that although rotational effects can reduce the inherent asymmetry parameter, it does not completely smear out the angular distribution to isotropic which would imply that $\beta_{O^+} = 0$. The average value for $\left(\frac{1+a^2}{4+a^2}\right)$ is determined over thermal distribution of rotational states *j*.

For the $v = 0$ vibrational level, the equations are as follows:

- The rotational velocity for $v = 0$ is determined by the equation $\omega_j = (L_j / I_{v=o})$; where the angular momentum $L_j = \frac{\sqrt{j(j+1)}\, h}{2\pi}$; j is the rotational quantum number. The moment of inertia I is calculated using the rigid rotor approximation i.e. $I_{v=0} = \mu R^2$, where μ is the reduced mass and R is the inter-nuclear separation. The equilibrium inter-nuclear separations for the v = 0 and 1 levels is taken to be 1.155 and 1.170 $x10^{-10}$ m respectively [16].

- Assuming the gas emerging from the effusive gas source is at room temperature, the thermal distribution of rotational states for v = 0 is determined by the population which is the Boltzmann distribution for each level multiplied by the corresponding degeneracy i.e. $Population_{v=0} = (2j+1)\ exp(-(E_j)_{v=0}/kT)$; k is the Boltzmann constant , Energy E_j for a Boltzmann distribution is determined by $(E_j)_{v=0} = \left(\frac{L^2}{2I}\right)_{v=0}$

- To calculate the weighted average for $\left(\frac{1+a^2}{4+a^2}\right)$, the population for each rotational state is summed and divided over the total population. From the equation given to calculate population, population for j=0 is 1, therefore $TotalPopulation = 1 + \sum_{j=1}^{j\max} Population_{v=0}$

- For a given $\beta_{O^+}^{T}$, the average value of $\beta_{O^+}^{v=0}$ is then given by

$$Average\beta_{O^+}^{v=0} = \beta_{O^+}^{T}\left(\frac{1+a_{v=0}{}^2}{4+a_{v=0}{}^2}\right)_{Weighted\ Avg}$$

$$Average\beta_{O^+}^{v=0} = \frac{\beta_{O^+}^{T} + \sum_{j=0}^{j\,max} Population_{v=0}\left(\frac{1+a_{v=0}{}^{2}}{4+a_{v=0}{}^{2}}\right)}{TotalPopulation}$$

However, since the population for $j = 0$ is 1, the summation in the above equation can be rewritten as:

$$\sum_{j=0}^{j\,max} Population_{v=0}\left(\frac{1+a_{v=0}{}^{2}}{4+a_{v=0}{}^{2}}\right) = 1 + \sum_{j=1}^{j\,max} Population_{v=0}\left(\frac{1+a_{v=0}{}^{2}}{4+a_{v=0}{}^{2}}\right)$$

Therefore,

$$Average\beta_{O^+}^{v=0} = \frac{\beta_{O^+}^{T} + \left(\beta_{O^+}^{T} + \sum_{j=1}^{j\max} Population_{v=0}\left(\frac{1+a_{v=0}{}^{2}}{4+a_{v=0}{}^{2}}\right)\right)}{TotalPopulation}$$

Substituting from Eqn 4.3:

$$Average\beta_{O^+}^{v=0} = \frac{\beta_{O^+}^{T} + \left(\sum_{j=1}^{j\max} Population_{v=0}\beta_{O^+}^{v=0}\right)}{TotalPopulation} \qquad (4.4)$$

; where $TotalPopulation = 1 + \sum_{j=1}^{j\max} Population_{v=0}$

In order to determine Average $\beta_{O^+}^{v=1}$ for a given $\beta_{O^+}^{T}$ the calculations are repeated with the above equation but considering the $v = 1$ vibrational level specifically.

4.3.4 PREVIOUS STUDIES

In the study by Lafosse *et al* [10] on the $c^4\Sigma_u^-$ state, the authors found a major discrepancy between their theoretical predictions and experimental observations. In [10] the authors determine β_{O^+} centered at ~1.9 eV (with $1.5 < E_{O+} < 3.2$ eV) in coincidence with ~2.7 eV electrons (with $1.2 < E_e < 4.5$ eV) for a photon energy of 27.35 eV. Their measured β_{O^+} value was ≈ 0.1 ± 0.05. The effect of rotation, due to the lifetime, on the theoretical asymmetry parameter, $\beta_{O^+}^T$, for a non-rotating molecule is considered in [10] and found that β_{O^+} should reduce from ≈ 1.4 [11] to ≈ 0.8. That study also found β_{O^+} to be ≈ 0 and 0.35 for $v = 0$ and 1 levels, respectively, at ~ 100 meV above their thresholds. Lafosse *et al* [10] recognized the appreciable discrepancy between theory and experiment and suggested that it could be due to either an underestimation in their apparatus function with large extraction fields or a lack of convergence in the calculation with respect to the inclusion of ion states. As this casts some doubt on the reliability of the experimental study and, indeed, the technique, it is important to reexamine their findings using a different method.

The vibrational levels v = 0, 1 have distinctly different lifetimes, τ_v, their dissociation routes are discussed in Sec 4.3.2. The lifetime τ_1 of the v = 1 level critically depends on the shape of the potential, given the fact that it decays to the L2 limit due to tunneling. Pulse-field ionization photoelectron (PFI-PE) experiments [16] determined τ_1 as 6.9 ± 0.7 $x10^{-14}$ s and this has been recently supported by theoretical studies [17, 18]. However, for the lifetime τ_0 of the v = 0 level there has been difficulty in reaching agreement between various research groups (both theory and experiment). The reason being that the v = 0 level dissociates to three different limits (as seen in Table 4.5). An earlier theoretical study by Tanaka and Yoshimine [23] took the tunneling lifetime for $v = 0$ to be the same as the estimated radiative lifetime, namely τ_f ~20 $x10^{-9}$ s, resulting in equal probabilities of fluorescence and DPI for $v = 0$, i.e. τ_0 ~10 $x10^{-9}$ s.

However, using the fluorescence branching ratio, *r*, of ~15% from [20] and Eqn (4.5) reduces τ_0 to $\leq 3\ x10^{-9}$ s.

$$\frac{1}{\tau_0} \geq \frac{1}{r\tau_f} \qquad (4.5)$$

As is evident, reliable knowledge of the fluorescence lifetime would be extremely valuable, yet this does not appear to have been measured at this time. Tanaka and Yoshimine [23] also provide a number of theoretical calculations, one of which has τ values for $\nu = 0$, 1 two orders of magnitude smaller than their final values (see Table 4.6). They considered those lifetimes to be too short, given the assumed value of τ_f.

The PFI-PE study of Evans *et al* [16], determined the τ_0 to be 2.7 ± 0.3 $x10^{-13}$ s, four orders of magnitude smaller than that from [23]. Although the subsequent theoretical study by Liebel *et al* [24] generally favoured 'fast' dissociation over 'slow' dissociation of [23], the τ_0 value from [16] was criticized in the study by Hikosaka *et al* [18] as being too prompt. From their experimental data they place a lower limit on τ_0 as $6\ x10^{-13}$ s and introduce a qualitative theoretical model resulting in a τ_0 value of ~ $1.3\ x10^{-11}$ s, which they caution should be viewed as a 'very rough estimate'. Two further theoretical studies [17, 25] now report τ_0 to be ≈ $1.2\ x10^{-11}$ s. Those studies, however, find ~99% of the dissociative ionization results in L2; this agrees with experiment for $\nu = 1$, but not $\nu = 0$ – as mentioned earlier, which has substantial decay to L1. These latter theoretical studies incorporated interactions between overlapping vibrational levels in the continuum, which reduces the slow dissociative ionization lifetimes from [23] by two orders of magnitude. For perspective, the vibrational spacing of 0.192 eV corresponds to a vibrational period of $2.15\ x10^{-14}$ s. Using $\tau_0 = 1.2\ x10^{-11}$ s and $\tau_1 = 6.9\ x10^{-14}$ s implies that $O_2^+(c^4\Sigma_u^-)$ in the $\nu = 0$ and 1 levels execute ~ 560 and 3 vibrations, respectively, prior to dissociation.

4.3.5 EXPERIMENTAL DETAILS

i. THE TPEPICO TECHNIQUE

Threshold Photoelectron Photoion Coincidence (TPEPICO) technique, i.e. measuring the coincidence yield between threshold photoelectrons and photoions was employed for this experiment. The information obtained with this method is particularly rich because the initial state of the system is well defined after the photon is absorbed [46]. In this technique the photon energy is fixed at a value that corresponds to a peak in the TPES spectrum which refers to the ionic state of interest. The threshold electrons are measured in coincidence with the ions that are produced in the dissociation of the molecular ions from that particular ionic state. The arrival times of these ions give information on the kinetic energy release and subsequently on the dissociation limits of the ionic states. This technique is hence an efficient tool to study the DPI of molecular systems. In this study we focus on studying the angular distribution of the $O^+(^4S)$ ions produced from dissociative photoionization of O_2^+ $c^4\Sigma_u^-(\nu=0,1)$.

ii. TOROIDAL SPECTROMETER USED FOR TPEPICO STUDY

The experiments were performed using the toroidal spectrometer in conjunction with linearly polarized synchrotron radiation on the VLS-PGM (undulator) beamline at the Canadian Light Source. The spectrometer as described in Chapter 2 consists of two toroidal analyzers configured to detect charged particles emitted in the plane orthogonal to the incoming photon beam, which is crossed with an effusive gas jet emanating from a hypodermic needle.

In this particular study we adapted the penetrating-field technique [31] to extract efficiently and selectively near-zero energy electrons. As shown in Fig 4 k, the smaller of the toroidal analyzers was dedicated to detecting threshold electrons and the larger analyzer to detect 2 eV $O^+(^4S)$ ions. The ~2 eV $O^+(^4S)$ photoions emitted in the detection plane are energy analyzed by the larger of the toroidal analyzers with the acceptance

angles and configuration indicated in Fig 4 k. The details of the electron optical arrangement needed for TPES have been given in [29].

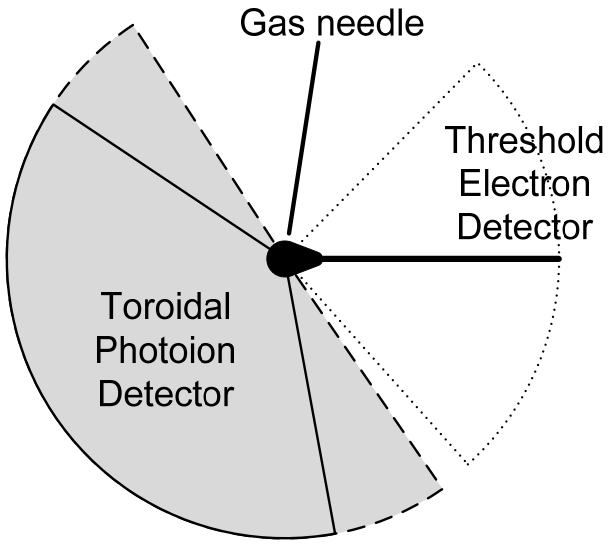

Fig 4 k: A schematic diagram of the acceptance angle ranges and the mutual configuration of the two toroidal analyzers in our detection geometry. The photon beam is out of the page and the polarization direction is horizontal. The TPEPICO signal corresponds to threshold electrons yield (over 4π sr) measured in coincidence with energy-resolved ions with emission angles within the central ~160° grey sector of the toroidal analyzer, whose mechanical angular range is 180°. The out-of-plane emission angular acceptance in the ion channel is ~ ±5°.

iii. DATA ACQUISITION

The focusing properties of the electrostatic analyzer allow the charged particle's emission angle (measured relative to the light polarization axis) to be mapped onto a 2-dimensional resistive anode encoder. The energy-resolved image on the ion detector is arc-shaped with positions around the perimeter corresponding to the emission angle. A

coincidence event is when both (ion and electron) detectors register a count within a specified time window, in this case 20 μs.

In the TPEPICO data acquisition mode, ($x,y,\Delta t$) are recorded for each coincidence event, where Δt is the time difference between the electron and ion signal and (x,y) are the ion detection coordinates on the position-sensitive detector . Post-processing the Δt data as a time histogram shows a peak of 'true' plus 'random' coincidences upon a constant background of only 'random' coincidences.

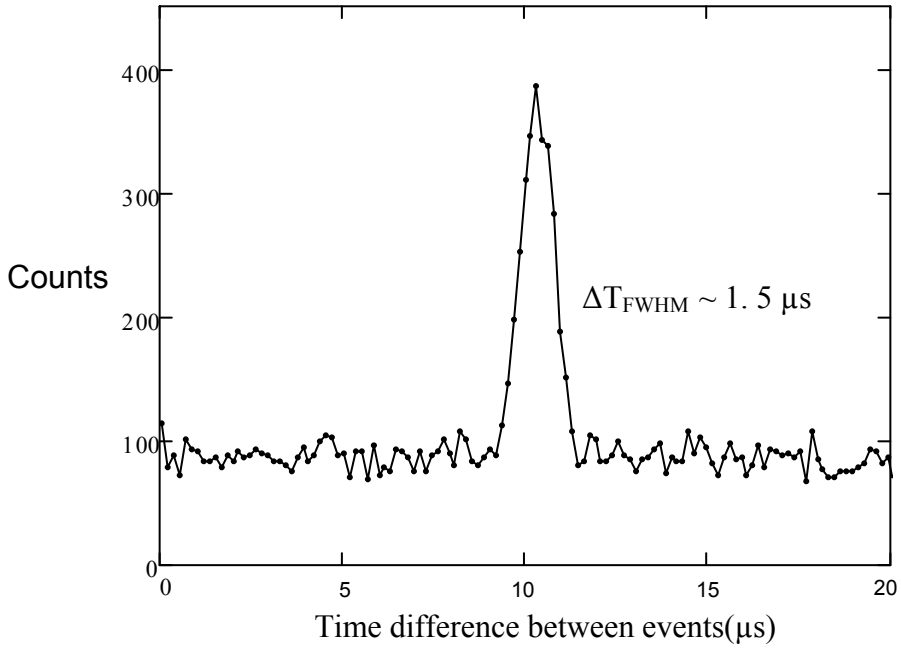

Fig 4 l: Shows sample TAC spectrum obtained for ion-electron coincidence data for this experiment showing a coincidence peak approximately around 10 μs

The 'true' coincidence peak was ~1.5 μs wide (FWHM) and the true-random ratio was ~ 7:1. The ion (x,y) data is converted to polar coordinates (r,θ) and the size of the angular intervals into which the data is processed is chosen later to correspond with the available statistics. In this case, 10° intervals in angle θ_i were used for all the presented data. The 'true' coincidence angular distribution was obtained by subtracting the 'random'

angular distribution from that of the total coincidence yield using standard procedures (see [26] and references therein). Since the random coincidence 'window' was 17.5 μs wide, 7 times wider than the base width of true 'window', this provided good statistical precision when subtracting these counts to obtain the true coincidences. The angular resolution, $\Delta\theta$, is deemed to be smaller that the angular interval based on our experience with (γ,2e) studies [28] and, when measuring the He^+ (n = 1) photoelectron angular distribution for 2 eV electrons, we observe the expected characteristic $\beta = 2$ pattern.

To study the angular distributions of the 2 eV ions produced specifically from the $c^4\Sigma_u^-$ ($v = 0,1$) vibrational level that dissociated specifically to the L2 limit, the kinematics of our coincidence experiment would be :

$$h\upsilon + O_2\ ^3\Sigma_g^- \rightarrow O_2^+\ c^4\Sigma_u^- + e^- \rightarrow O\ ^1D + O^+\ ^4S + e^-\ (\approx 0\ eV)$$

Due to axial recoil in a homonuclear diatomic molecule, the ion energy is simply given by:

$$E_{O^+} = \frac{1}{2}(h\upsilon - D) \qquad (4.6)$$

where the dissociation limit(s), D, is given in Table 4.5. As the threshold photoelectron yield peaks at $h\upsilon$ = 24.564 and 24.756 eV for $v = 0$ and 1 levels, respectively, then the corresponding E_{O^+} values using Eqn (4.6) are 1.932 eV and 2.028 eV for the L2 dissociation limit. The toroidal analyzer used to detect ions was operated with an energy resolution of $\approx \Delta E = 0.5$ eV, which is much broader than the ~100 meV spacing when set to detect 2.0 eV ions, and can readily separate ions from the neighbouring L1 and L3 limits.

4.3.6 RESULTS AND DISCUSSION

i. ENERGY WIDTHS AND LIFETIMES

Fig 4 o shows the threshold photoelectron spectrum for O_2^+ in the vicinity of the predissociative $c^4\Sigma_u^-$ state showing its three vibrational levels (ν = 0, 1, 2) with progressively larger energy widths. We can also measure the *increase* in peak widths of the $\nu = 0$ and $\nu = 1$ vibrational levels over the instrumental width determined earlier. The rotational profile [16, 25] seen in Fig 4 m and 4 n shows that the main contribution to the *rising* edge of the threshold peak is from the 'P' branch, which is expected to extend over only a few meV depending upon rotational temperature. The procedure is to fit each peak to a Lorenzian lineshape over its *rising* edge from low photon energy to the peak maximum, which gives 4.2 ± 0.2 meV for $\nu = 0$ and 11.8 ± 0.4 meV for $\nu = 1$. Since the rotational profiles of the $\nu = 0$ and $\nu = 1$ transitions are broadly similar [16] and since $\tau_0 >> \tau_1$, we can use these values to estimate the increase in the $\nu = 1$ peak width due to lifetime broadening. As in other photoelectron studies [15, 31, 34], a very weak broad feature corresponding to $\nu = 2$ is observed at ≈ 24.97 eV on the sloping background of the $c^4\Sigma_u^-$ continuum [33]. We estimate its energy width to be ~ 120 ± 20 meV, which is larger than the 40 meV observed in [34] and in remarkable agreement with the predicted values given in Table 4.6.

For a given energy width ΔE the lifetime τ is calculated using the following equation; $\Delta E = \frac{h}{2\pi\tau}$ where h is Planck constant and thus τ is calculated individually for $v = 0$ and $v = 1$. Subtracting the values in quadrature gives a width of 11.0 ± 0.5 meV for $\nu = 1$ corresponding to a lifetime of 6.0 ± 0.3 $x10^{-14}$ s. This is reasonable agreement with the only other measured value of 6.9 ± 0.7 $x10^{-14}$ [16] and the theoretical values given in Table 4.6. Note that the lower limit on τ_1 from this study is 5.6 ± 0.2 $x10^{-14}$ s, based on the measured $\nu = 1$ peak width and the photon resolution.

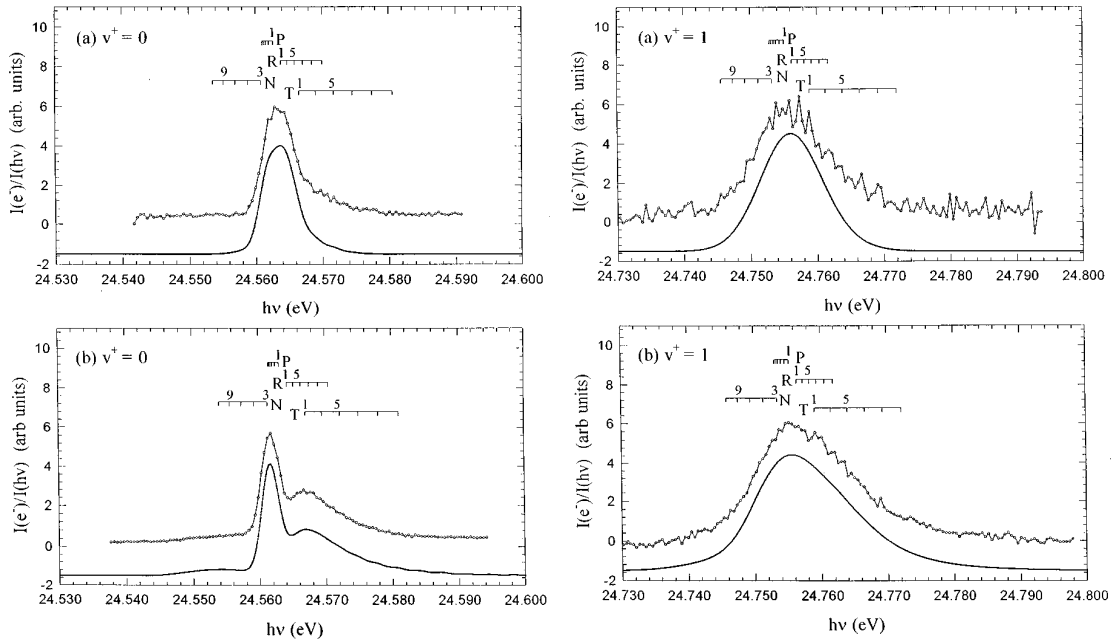

4 m 4 n

Fig 4 m & 4 n: Shown in Fig 4 m and 4 n are the rotational profiles of the vibrational levels $v = 0$, 1 respectively of the O_2^+ $c^4\Sigma_u^-$ state from the PFI PE study of Evans *et al* [16]. Fig 4 m: PFI PE bands for O_2^+ $c^4\Sigma_u^-$ $v = 0$ (upper curves) Fig 4 n: PFI PE bands for O_2^+ $c^4\Sigma_u^-$ $v = 1$ (upper curves). Fig 4 m, 4 n: a) Supersonically cooled O_2 sample b) effusive gas jet O_2 sample [16]. Also plotted are the simulated curves (lower curves, solid line) using rotational temperature of 35 K for supersonically cooled sample and 298 K for the effusive sample. The rotational lines for the N, P, R, and T rotational branches are marked in the figures. The instrumental PI-PE resolution used is 1.4 meV or 11 cm^{-1} (FWHM)

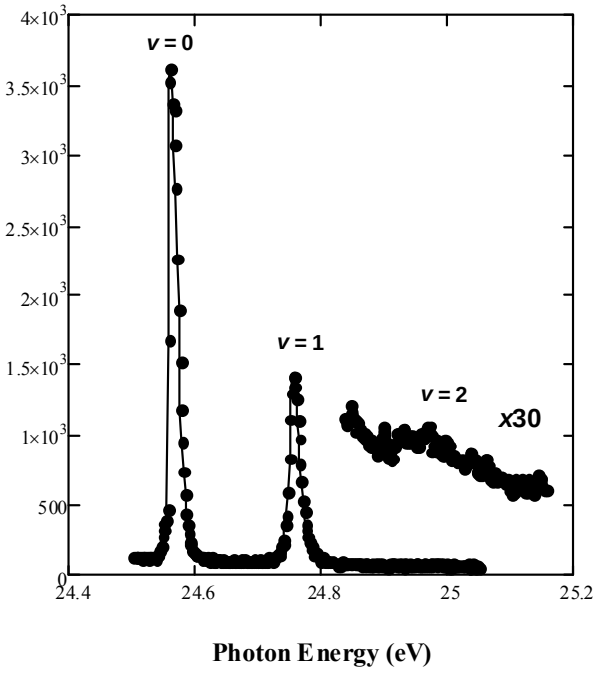

Fig 4 o: TPES of the O_2^+ $c^4\Sigma_u^-$ state, showing vibrational levels v = 0, 1 and also seen is the broader and weaker v = 2 vibrational level

ii. RATIO OF ANGULAR DISTRIBUTIONS AND LIFETIMES

Our goal was to determine individual β for the O^+ angular distributions for the v = 0, 1 levels of the $c^4\Sigma_u^-$ state using the TPEPICO technique. However, we were not able to ascertain the individual ion angular distributions from this data due to:

a) Non-negligible systematic errors in the angular response of the toroidal analyzers
b) The lack of a suitable calibrant of 2 eV ions with an accurately and reliably known β.

Taking the ratio of the angular distributions gives a *relative* measurement and has the advantage in that the systematic errors in the angular efficiency are effectively eliminated. Using such ratios has been used previously to good effect [*e.g.* 38-40]. Fig 4 p represents the *ratio* of the O^+ angular distributions to the L2 limit for the v = 1:0 levels

of the $c^4\Sigma_u^-$ state measured in coincidence with a threshold photoelectron. The ratio in Fig 4 p (a) of the 'true' coincidence angular distribution of 2 eV O^+ ions corresponds explicitly to the $\nu = 1/\nu = 0$ yield. The Eqn (4.7) below is deduced by using Eqn 4.2 from Sec 4.3.3 for individual (ν = 0, 1) angular distribution and then taking a ratio:

$$\frac{\sigma_{O^+}^{\nu=1}\left(1+\beta_{O^+}^{\nu=1}P_2(\cos\theta)\right)}{\sigma_{O^+}^{\nu=0}\left(1+\beta_{O^+}^{\nu=0}P_2(\cos\theta)\right)} \qquad (4.7)$$

Fig 4 p (b) corresponds to the angular distribution ratio of 2 eV O^+ ions at $h\upsilon$ = 24.756 and 24.564 eV i.e., random coincidences:

$$\frac{\left(\sigma_{O^+}^{\nu=1}\left(1+\beta_{O^+}^{\nu=1}P_2(\cos\theta)\right)+\sigma_{O^+}^{\nu=0}\left(1+\beta_{O^+}^{\nu=0}P_2(\cos\theta)\right)\right)_{24.756\,\mathrm{eV}}}{\left(\sigma_{O^+}^{\nu=0}\left(1+\beta_{O^+}^{\nu=0}P_2(\cos\theta)\right)\right)_{24.564\,\mathrm{eV}}} \qquad (4.8)$$

At 24.756 eV, 2eV O^+ ions can be produced by DPI from both $\nu = 1$ and 0 levels, unlike the lower photon energy which is below the $\nu = 1$ threshold. The underlying continuum does not decay to L2, but to L5, hence this does not contribute to the 2 eV ion yield. The relative proportion of $\nu = 1$ and 0 levels at the upper photon energy is taken to be given by the ratio of the threshold photoelectron yield, namely 1: 2.1; i.e. we make the approximation that both the $\nu = 0$ cross section and $\beta_{O^+}^{\nu=0}$ at 24.756 eV is the same as at 24.564 eV is made. Thus, Eqn (4.8) is further modified and the measured angular distribution ratio in Fig 4.p(b) is proportional to:

$$\frac{\left(\sigma_{O^+}^{\nu=1}\left(\left(1+\beta_{O^+}^{\nu=1}P_2(\cos\theta)\right)+2.1\left(1+\beta_{O^+}^{\nu=0}P_2(\cos\theta)\right)\right)\right)_{24.756\,\mathrm{eV}}}{\left(\sigma_{O^+}^{\nu=0}\left(1+\beta_{O^+}^{\nu=0}P_2(\cos\theta)\right)\right)_{24.564\,\mathrm{eV}}} \qquad (4.9)$$

It is evident in Fig 4 p (a) that the ratio distribution is slightly elongated along the polarization direction; from the form of Eqn 4.7 this implies $\beta_{\nu=1} > \beta_{\nu=0}$, which is primarily due to the differences in lifetimes.

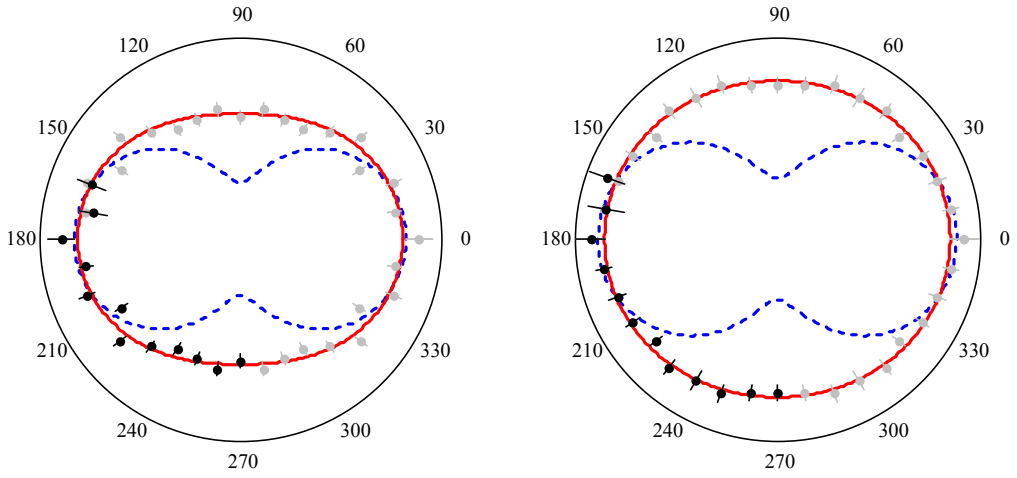

(a) (b)

Fig 4 p: Polar plots of the *ratio* of the O^+ angular distributions to the L2 limit for the v = 1:0 levels of the $c^4\Sigma_u^-$ state measured in coincidence with a threshold photoelectron. The two graphs correspond to the ratio of (a) 'true' coincidences and (b) random coincidences (i.e. completely uncorrelated in time) at the two threshold photon energies, 24.756 and 24.564 eV. The measured black data points between 180° and 270° have been reflected in the x and y axes to give the grey points. The dashed curve corresponds to the ratio (arbitrarily normalized to the experimental data) using the following values of the asymmetry parameter and the lifetimes: $\beta^T_{O^+} = 1.6$, $\tau_0 = 1.2\,x10^{-11}$ s and $\tau_1 = 6.0\,x10^{-14}$ s. The solid curve is fitted to the measured data leading to $\beta^T_{O^+} = 0.40$; see text for discussion.

The value of $\beta^T_{O^+}$ has, to our knowledge, only been determined by Lin and Lucchese [11]. They do not find a significant change in the $\beta^T_{O^+}$ values with the number of channels they include in their calculations and at threshold $\beta^T_{O^+} \geq 1.6$. We used $\beta^T_{O^+} = 1.6$, $\tau_0 = 1.2\,x10^{-11}$ s from the published literature (see Table 4.6) and $\tau_1 = 6.0\,x10^{-14}$ s from this work (from energy width analysis, see Sec 4.3.6.i) and used Eqn 4.7

(for "true" coincidences) , Eqn 4.9 (for "random" coincidences) and Eqn 4.3 to plot the ratio on top of the experimental angular distribution ratio. A completely unacceptable ratio *shape* in comparison to the data (arbitrarily normalized), as shown in Fig 4 p (dotted lines) is obtained. No agreement is found between the observed and theoretical ratio shape for any physically plausible values of τ_0 and τ_1. Thus, it seems like the value for $\beta^T_{O^+} = 1.6$ needs to re-evaluated following further work. Hence, it was necessary to perform a fitting procedure with the three variables $\beta^T_{O^+}$, τ_0 and τ_1.

Eqns (4.7), (4.8) and (4.3) were used in Origin 6.1 to perform non linear curve fitting on the angular distribution ratios.

- Fitting Procedure 1 (varying $\beta^T_{O^+}$): τ_0 = 1.2 $x10^{-11}$ s (from published literature-Table 4.6) and τ_1 = 6.0 $x10^{-14}$ s , from our energy width analysis was kept fixed. The only value that was varied was $\beta^T_{O^+}$. This resulted in $\beta^T_{O^+}$ = 0.38 ± 0.07 and 0.40 ± 0.05 for Fig 4 p(a) and (b), respectively, giving essentially the same $\beta^T_{O^+}$ from the two different data sets and justifying the approximations made in Eqn (4.9). The corresponding β_{O^+} values are 0.10 ± 0.02 and 0.30 ± 0.04 for $\nu = 0$ and 1 levels, respectively. These values are in good agreement with $\beta_{O^+} \approx 0$ and 0.35 observed in the earlier vector correlation study of Lafosse *et al* [10], indicating that their determination of their vector mapping apparatus function was reliable – despite their stated caution. Although these results are obtained from using the 'best' values of τ_0 and τ_1 in Eqns (4.7), (4.9) and (4.3) the effect of using other plausible values had to be considered.

- Fitting Procedure 2 (varying τ_0): Increasing τ_0 from 1.2 $x10^{-11}$ s makes essentially no difference to the result, since β_{O^+} is close to its limit of $\beta^T_{O^+}/4$ for τ_0

(see Eqn (4.3)). If τ_0 is taken as 6 $x10^{-13}$ s, the experimental lower limit from [18], it is found that $\beta^T_{O^+}$ = 0.40 ± 0.07 and 0.41 ± 0.06 for Fig 4 p(a) and (b), respectively.

- Fitting Procedure 3 (varying τ_1): If τ_1 = 6.9 ± 0.7 $x10^{-14}$ s is taken, the consensus experimental and theoretical value from Table 4.6 [16, 18] then it is found that $\beta^T_{O^+}$ = 0.42 ± 0.07. These values all cluster within error bars of the fit, so the uncertainties in the lifetimes τ_0 and τ_1 do not significantly affect the value of $\beta^T_{O^+}$.

4.4 CONCLUSION

From our energy width analysis and taking ratio of the photoion angular distribution of $O^+(^4S)$ produced from dissociative photoionization of O_2^+ $c^4\Sigma_u^-$ (ν = 0, 1) allows us to place a lower limit on τ_0 as ≈1 $x10^{-12}$ s, corresponding to an energy width of < ≈1 meV. This work, therefore, supports the experimental findings of [18]. There remains a factor ~20 difference between the experimentally determined lower limit of τ_0 and the current predicted values, even with this new experimental approach; narrowing that gap is a challenge for future work. The lack of sensitivity in being able to determine the τ_0 more precisely, for a given τ_1, using this technique is partly due to the small value of the inherent asymmetry parameter $\beta^T_{O^+}$ for this particular ionic state. It is also determined that τ_1 = 6.0 ± 0.3 $x10^{-14}$ s and $\beta^T_{O^+}$ = 0.40 ± 0.05, which is significantly smaller than predicted, $\beta^T_{O^+} \geq 1.6$, but in agreement with the experimental findings in [10]. The estimate of the energy width of 120 ± 20 meV for the ν = 2 level, corresponds to τ_2 = 5.5 ± 1.0 $x10^{-15}$ s, is in excellent agreement with the results of recent calculations [17, 24, 25].

Table 4.6: Table below summarizes our results in comparison with recent theoretical and experimental work.

$c^4\Sigma_u^-$	$v = 0$		$v = 1$		$v = 2$	
$h\upsilon$ (eV)	24.564[a]		24.756[a]		25.005[a]	
Theory / Exp	Γ_0 (meV)	τ_0 (s)	Γ_1 (meV)	τ_1 (s)	Γ_2 (meV)	τ_2 (s)
[23] T[b]	$3.3\,x10^{-5}$	$20\,x10^{-9}$	0.013	$5\,x10^{-11}$	1.6	$4\,x10^{-13}$
[23] T (SDCI) [b,c]	0.019	$3.5\,x10^{-11}$	3.6	$1.8\,x10^{-13}$		
[16] E	2.4	$2.7(3)\,x10^{-13}$	9.5	$6.9(7)\,x10^{-14}$		
[24] T[b]	0.19	$3.4\,x10^{-12}$	10.4	$6.3\,x10^{-14}$	167	$3.9\,x10^{-15}$
[18] E[d]	< 1.1	$> 6\,x10^{-13}$	9.5	$6.9\,x10^{-14}$		
[18] T[d]	0.05	$1.3\,x10^{-11}$	9.5	$6.9\,x10^{-14}$		
[25] T[b]	0.056	$1.17\,x10^{-11}$	13.2	$4.99\,x10^{-14}$	112	$5.88\,x10^{-15}$
[17] T[b]	0.054	$1.2\,x10^{-11}$	9.7	$6.8\,x10^{-14}$	142	$4.6\,x10^{-15}$
This Work	$< \approx 1$	$> \approx 1\,x10^{-12}$	11.0 ± 0.5	$6.0 \pm 0.3\,x10^{-14}$	120 ± 20	$\approx 5.5 \pm 1.0\,x10^{-15}$

[a] From [35]. The calculated energies from [25] are 0.108 meV higher and the observed value in [15] is 24.96 eV.

[b] Predissociation lifetimes only, which is the dominant decay mechanism. However, when comparing with experimental values for the $v = 0$ level, one should note the lifetime is slightly shorter (Γ_0 wider) than calculated due to the fluorescence channel.

[c] Single and double excitation configuration interaction (SDCI).

[d] 1.1 meV is their *upper* limit from experimental observation, corresponding to a *lower* limit on τ_0; 0.05 is an estimate from the model presented in [18]. They support [16] in their value for τ_1.

4.5 REFERENCES:

[1] Rees M H 1989 Physics and Chemistry of the Upper Atmosphere *Cambridge: Cambridge University Press*

[2] Yung Y L and DeMore W B 1999 Photochemistry of Planetary Atmospheres (Oxford: Oxford University Press)

[3] Vardavas I M and Taylor F 2007 Radiation and Climate *Oxford: Oxford University Press*

[4] Waite J H, Jr *et al.* 2005 *Science* **307** 1260-2

[5] Johnson R E *et al.* 2006 *Icarus* **180** 393-402

[6] Luna H, McGrath C, Shah M B, Johnson R E, Liu M, Latimer C J and Montenegro E C 2005 *Astrophys. J.* **628** 1086-96

[7] Melo W S, Santos A C F, Sant'Anna M M, Sigaud G M and Montenegro E C 2008 *J. Phys. B: At. Mol. Phys.* **41** 205201

[8] Bagenal F, Dowling T E and McKinnon W B 2004 Jupiter: The Planet, Satellites and Magnetosphere *Cambridge: Cambridge University Press*

[9] Lafosse A, Brenot J C, Golovin A V, Guyon P M, Hoejrup K , Houver J C, Lebech M and Dowek D 2001 *J. Chem. Phys.* **114** 6605-17

[10] Lafosse A, Brenot J C, Guyon P M, Houver J C, Golovin A V, Lebech M, Dowek D, Lin P and Lucchese R R 2002 *J. Chem. Phys.* **117** 8368-84

[11] Lin P and Lucchese R R 2002 *J. Chem. Phys.* **116** 8863-75

[12] Eland J H D and Duerr E J 1998 *Chem. Phys.* **229** 1-11

[13] Frasinski L J, Randall K J and Codling K 1985 *J. Phys. B: At. Mol. Phys.* **18** L129-L135

[14] Akahori T, Morioka Y, Watanabe M, Hayaishi T, Ito K and Nakamura M 1985 *J. Phys. B: At. Mol. Phys.* **18** 2219-29

[15] Ellis K, Hall R I, Avaldi L, Dawber G, McConkey A, Andric L and King G C 1994 *J. Phys. B: At. Mol. Phys.* **27** 3415-26

[16] Evans M, Stimson S, Ng C Y and Hsu C W 1998 *J. Chem. Phys.* **109** 1285-92

[17] Demekhin F V, Omel´yanenko D V, Lagutin B M, Sukhorukhov V L, Werner L, Ehresmann A, Schartner K -H and Schmoranzer H 2007 *Rus. J. Phys. Chem. B.* **2** 213-21

[18] Hikosaka Y, Lablanquie P, Ahmad M, Hall R I, J.G. L, Penent F and Eland J H D 2003 *J. Phys. B: At. Mol. Phys.* **36** 4311

[19 LeBlanc F J 1963 *J. Chem. Phys.* **38** 487-8

[20] Richard-Viard M, Dutuit O, Ait-Kaci M and Guyon P M 1987 *J. Phys. B: At. Mol. Phys.* **20** 2247-54

[21] Richard-Viard M, Dutuit O, Lavollee M, Govers T, Guyon P M and Durup J 1985 *J. Chem. Phys.* **82** 4054-63

[22] Hikosaka Y, Aoto T, Hall R I, Ito K, Hirayama R, Yamamoto N and Miyoshi E 2003 *J. Chem. Phys.***119** 7693-700

[23] Tanaka K and Yoshimine M 1979 *J. Chem. Phys.* **70** 1626-33

[24] Liebel H, Ehresmann A, Schmoranzer H, Demekhin Ph V, Lagutin B M and Sukhorukov V L 2002 *J. Phys. B: At. Mol. Phys.* **35** 895-905

[25] Ehresmann A, Werner L, Klumpp S, Schmoranzer H, Demekhin Ph V, Lagutin B M, Sukhorukov V L, Mickat S, Kammer S, Zimmermann B and Schartner K-H 2004 *J. Phys. B: At. Mol. Phys.* **37** 4405-22

[26] Reddish T J, Richmond G, Bagley G W, Wightman J P and Cvejanović S 1997 *Rev. Sci. Instrum*. **68** 2685-92

[27] Hu *et al.* 2007 *Rev. Sci. Instrum.* **78** 083109

[28] Wightman J P, Cvejanović S and Reddish T J 1998 *J. Phys. B: At. Mol. Phys.* **31** 1753-64

[29] Cvejanović S, S Bagley G W and Reddish T J 1994 *J. Phys. B: At. Mol. Phys.* **27** 5661-79

[30] Slattery A E, Wightman J P, MacDonald M A, Cvejanović S and Reddish T J 2000 *J. Phys. B: At. Mol. Phys.* **33** 4833-48

[31] Cvejanović S and Read F H 1974 *J. Phys. B: At. Mol. Phys.* **7** 1180-92

[32] Guyon P M and Nenner I 1980 *App. Opt.* **19** 4068-79

[33] Tanaka T, Yoshii H, Y Morioka Hayaishi T, Ito K and Hall R I 1998 *J. Chem. Phys.* **108** 6240-8

[34] Takeshita K, Sadamatu Y and Tanaka K 2005 *J. Chem. Phys.* **122** 044302

[35] Baltzer P, Wannberg B, Karlsson L, Göthe M C and Larsson M 1992 *Phys. Rev. A.* **45** 4374-84

[36] Lu Y, He Z X, Cutler J N, Southworth S H, Stolte W C and Samson J A R 1998 *J. Elec. Spec.* **94** 135-47

[37] Shaw D A, Holland D M P, Rennie E E and Shpinkova L G 2005 *J. Phys. B: At. Mol. Phys.* **38** 173-88

[38] Reddish T J and Feagin J M 1999 *J. Phy. B: At. Mol. Phys.* **32** 2473-86

[39] Seccombe D P, Collins S A, Reddish T J, Selles P, Malegat L, Kazansky A L and Huetz A 2002 *J. Phy. B: At. Mol. Phys.* **35** 3767-80

[40] Kheifets A S and Bray I 2005 *Phys. Rev. A.* **72** 022703

[41] Jonah C 1971 *J. Chem. Phys.* **55** 1915-22

[42] Cafolla A A, Reddish T, Wills A A and Comer J 1990 *J. Phys. B: At. Mol. Phys.* **7** 1180

[43] N. H. F. Beebe, E. W. Thulstrup, and A. Anderson, 1976 *J. Chem. Phys.* **64**, 2080

[44] Wills A A, Cafolla A A and Comer J 1991 *J. Phys, B;* At. *Mol. Opt. Phy,* **24** 3989

[45] J. H. D. Eland and E. J.Duerr 1998 *Chem. Phys*. **229** 1

[46] R I Hall *et al* 1992 *J. Phys. B: At. Mol. Opt. Phys.* **25** 377

[47] Padmanabhan A, MacDonald A, Ryan C H, Zuin L and Reddish T J 2010 *J. Phys: B Mol. Opt. Phys*. **43** 165204

[48] Sadeghpour *et al* 2000 *J. Phys. B: At. Mol. Opt. Phys.* **33** R93

[49] King and Avaldi 2000 *J. Phys. B: At. Mol. Opt. Phys.* **33** R215

[50] Bouri *et al* 2007 *J. Phys. B: At. Mol. Opt. Phys.* **40** F51

[51] Cvejanovic S, Shiell R C and Reddish T J 1995 *J. Phys. B: At. Mol. Opt. Phys.* **28** L707

[52] Wehlitz, M-T Huang, I A Sellin and Y Azuma 1999 *J. Phys. B: At. Mol. Opt. Phys.* **32** L635

[53] Thompson D B *et al* 1998 *J. Phys. B: At. Mol. Opt. Phys.* **31** 2225

[54] Lablanquie P, Ito K, Morin P, Nenner I and Eland J H D 1990 *Z. Phys.* D **16** 77

[55] Wannier G H 1953 *Phys. Rev.* **90** 817–25

[56] Read F H 1985 *Electron Impact Ionisation* ed T D M¨ark and G H Dunn

CHAPTER 5: DISSOCIATIVE PHOTOIONIZATION STUDIES OF H_2

5.1 INTRODUCTION

In the dissociative photoionization (DPI) process, ionization and dissociation can both occur on a very short timescale and the coupling between the electrons and nuclei can lead to the observation of interference phenomena [1,2]. The DPI process equation for H_2 is expressed by $h\nu + H_2 \rightarrow H + H^+ + e^-$. Fernández and Martín 2009 [1] reported oscillations in electron/ion asymmetry parameter β, for photon energy region 33eV in their theoretical calculations. Results for photoelectron/ion asymmetry parameter, β, for photon energies 20 and 27 eV were also presented in that study, however it was the 33 eV result that showed a rapidly changing photoelectron β (with electron energy) for randomly oriented H_2 molecules. Further analysis reveals that, these predicted large amplitude oscillations are the signature of interferences between the $1Q_1\,{}^1\Sigma_u^+$ and $1Q_2\,{}^1\Pi_u$ doubly-excited states decaying at different inter-nuclear distances. The oscillations thus provide information about the classical paths followed by the nuclei during DPI. The presence of such oscillations is predicted to be a general phenomenon in DPI.

In light of the above predictions, we performed DPI experiments in the region between $h\nu$ = 31-35 eV. Large amplitude oscillations in the photoelectron asymmetry parameter,β, as a function of electron energy for photon energies 31,33 and 35 eV are observed for the first time. Subsequent to the initial study, a second set of measurements were recorded at photon energies above and below the photon energy region 31-35 eV, in order to study the role of the interference, or lack there of, between the Q_1 and Q_2 doubly-excited states and how that would affect the nature of β as a function of electron and photon energy. Also measured were ion (proton) asymmetry parameter,β, for photon energies 27 and 33 eV. Preliminary results for measured electron/ion β for 25, 29, 35 and 37 eV are also presented at the end of this chapter.

5.2 DISSOCIATIVE PHOTOIONIZATION (DPI) IN H_2

Dissociative Photoionization (DPI) in H_2 occurs when the photon energy is greater than the dissociative ionization threshold for H_2 i.e. when *hv* is ≥ 18.076 eV resulting in $H(1s)+H^{+}+e^{-}$ (Fig 5 a). At *hv* ≥ 28.281 eV the $H(n=2)+H^{+}+e^{-}$ channel can be accessed. As seen in Fig 5 a, the first ionic state is $H_2^{+}\ X^{2}\Sigma_g^{+}\left(1s\sigma_g\right)$ and has bound vibrational levels. The next two ionic states are $H_2^{+}\ ^{2}\Sigma_u^{+}\left(2p\sigma_u\right)$ and $H_2^{+}\ ^{2}\Pi_g\left(2p\pi_u\right)$ that are both repulsive and converging to these limits are two Rydberg series labeled Q_1 ($2p\sigma_u, nl\lambda$) and Q_2 ($2p\pi_u, nl\lambda$) ($n >$ 1), respectively. The Q_1 resonance series includes doubly excited states that lie above the first ionization threshold $X^{2}\Sigma_g^{+}\left(1s\sigma_g\right)$, but below the second second ionization threshold of $^{2}\Sigma_u^{+}\left(2p\sigma_u\right)$. Therefore, autoionization of the Q_1 states leads to H_2^{+} ions in the ground state $X^{2}\Sigma_g^{+}$. However, autoionization of resonances Q_n (n> 1) converging to higher thresholds also lead to H_2^{+} ions in excited sates. This would be the case for the Q_2 series which converges to the third ionization threshold $^{2}\Pi_u\left(2p\pi_u\right)$. At photon energies around *hv* = 33 eV where both Q_1 and Q_2 are accessible in the Franck Condon (FC) region, autoionization leads to H_2^{+} ions in the $X^{2}\Sigma_g^{+}\left(1s\sigma_g\right)$ (ground state) state and also in the $^{2}\Sigma_u^{+}\left(2p\sigma_u\right)$ state (second ionization threshold). In the region where $h\nu$ = 31-35 eV, since both the Q_1 and Q_2 doubly excited states are accessible more than one route to a DPI process is possible. The competing processes are:

$$h\nu + H_2\left(X^{1}\Sigma_g^{+}\right) \rightarrow H_2^{+}\ ^{2}\Sigma_g^{+}\left(1s\sigma_g\right) + e^{-} \rightarrow H^{+} + H(1s) + e^{-} \quad (1)$$

$$h\nu + H_2\left(X^{1}\Sigma_g^{+}\right) \rightarrow H_2^{+}\ ^{2}\Sigma_u^{+}\left(2p\sigma_u\right) + e^{-} \rightarrow H^{+} + H(1s) + e^{-} \quad (2)$$

$$h\nu + H_2\left(X^{1}\Sigma_g^{+}\right) \rightarrow H_2^{**}\left(Q_1\ ^{1}\Sigma_u^{+}, ^{1}\Pi_u\right) \rightarrow H_2^{+}\ ^{2}\Sigma_g^{+}\left(1s\sigma_g\right) + e^{-} \rightarrow H^{+} + H(1s) + e^{-} \quad (3)$$

$$h\nu + H_2\left(X^{1}\Sigma_g^{+}\right) \rightarrow H_2^{**}\left(Q_2\ ^{1}\Sigma_u^{+}, ^{1}\Pi_u\right) \rightarrow H_2^{+}\ ^{2}\Sigma_g^{+}\left(1s\sigma_g\right) + e^{-} \rightarrow H^{+} + H(1s) + e^{-} \quad (4)$$

$$h\nu + H_2\left(X^{1}\Sigma_g^{+}\right) \rightarrow H_2^{**}\left(Q_2\ ^{1}\Sigma_u^{+}, ^{1}\Pi_u\right) \rightarrow H_2^{+}\ ^{2}\Sigma_u^{+}\left(2p\sigma_u\right) + e^{-} \rightarrow H^{+} + H(1s) + e^{-} \quad (5)$$

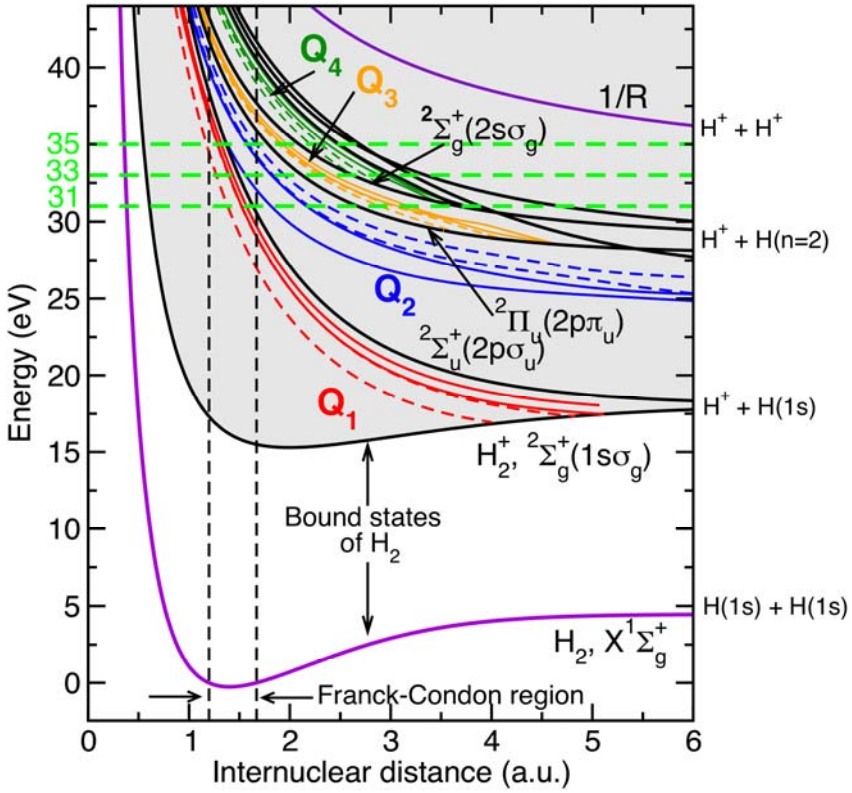

Fig 5 a**:** The potential energy curves of the H_2 and H_2^+ systems from [1] with the shaded area representing the ionization continuum and the dashed vertical lines corresponding to the Franck Condon (FC) region from the ground vibrational level. The different series of doubly excited states, Q_n, are represented by different colors: red lines, Q_1 states; blue lines, Q_2 states; orange lines, Q_3 states; green lines, Q_4 states. Q_n states of $^1\Pi_u$ symmetry are represented by full lines and those of $^1\Sigma_u^+$ symmetry by dashed lines. Of particular interest to $h\nu$ = 31-35 eV energy region are the Q_1 (red curves) and Q_2 (blue curves) doubly excited states of $^1\Pi_u$ and $^1\Sigma_u^+$ symmetry designated by full and dashed curves, respectively.

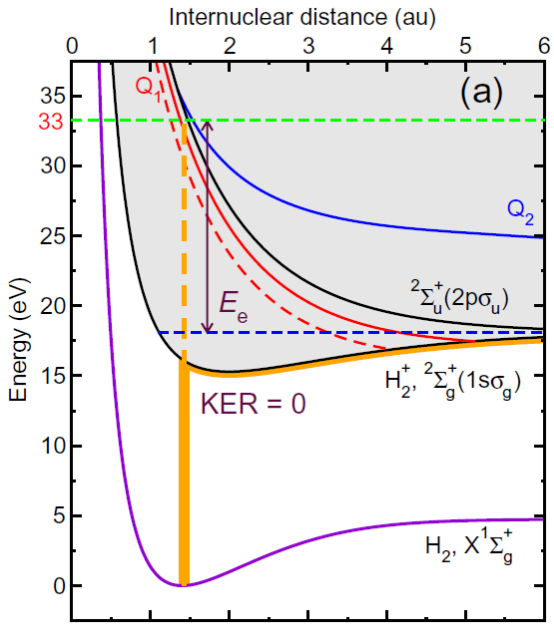

Fig 5 b: Potential energy curve from [1] for process (1) at $h\nu$ = 33 eV, where dissociative ionization is a direct process that leads to the H_2^+ ion in the $X\,^2\Sigma_g^+\left(1s\sigma_g\right)$ state.

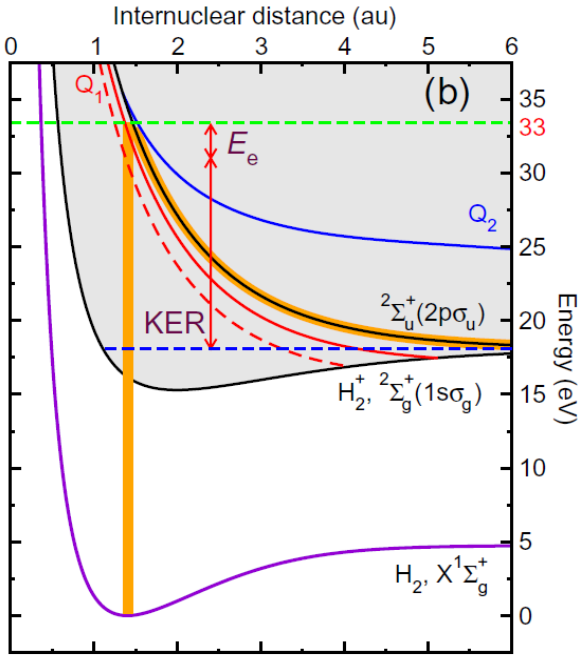

Fig 5 c: Potential energy curve from [1] for process (2) at $h\nu$ = 33 eV, where dissociative ionization is a direct process that leads to the H_2^+ ion in the second ionization threshold, $^2\Sigma_u^+\left(2p\sigma_u\right)$ state.

Specifically for $h\nu$ = 33 eV when ionization occurs through processes (1) and (2), DPI is a direct process and the ionization pathways are distinguishable; as shown in Fig 5 b and 5 c respectively. Process (1) results in the H_2^+ ion being in the $X\,^2\Sigma_g^+\left(1s\sigma_g\right)$ state and H_2^+ ion from process (2) ends up in the $^2\Sigma_u^+\left(2p\sigma_u\right)$ state. One can note from Fig 5 a, that the energy difference between the first two ionization thresholds in the FC region is approximately 17 eV. In process (1), if H_2 is directly ionized in a vertical transition to the ground state the photoelectron would have an energy of about $E_e = h\nu$ – 16 eV and the H_2^+ ion would remain in $X\,^2\Sigma_g^+\left(1s\sigma_g\right)$ state. In case of process (2), the second ionization state is a repulsive state, the energy of the photoelectron post ionization would be about $E_e = h\nu$ – 33 eV for the H_2^+ ion to remain in $^2\Sigma_u^+\left(2p\sigma_u\right)$ state.

Processes (3), (4) & (5) are indirect processes where the dissociation is attributed to resonant DPI. It should be noted that in case of autoionization; the ionization process can occur outside the FC region due to the finite lifetimes and the repulsive nature of the potentials. The photoelectron energies resulting from the two different channels $1s\sigma_g$ and $2p\sigma_u$ can be more similar than the photoelectron resulting from the direct ionization process. Such is the case for process (3), (4) & (5), where the autoionization from Q_1 and Q_2 state occurs at a larger inter-nuclear distance. It can be seen in Fig 5 e that the photoelectron energy associated with $^2\Sigma_g^+\left(1s\sigma_g\right)$ channel is closer to the energy of the photoelectron associated with the $^2\Sigma_u^+\left(2p\sigma_u\right)$ channel. Thus the photoelectron energies associated with autoionization also depend on the final H_2^+ ion state. The lowest Q_1 and Q_2 states have $^1\Sigma_u^+$ and $^1\Pi_u$ symmetries, respectively, and both autoionize on a < 10 fs timescale [3].

In Fig 5 d and 5 e, the kinetic energy release (KER_i) of the ion fragments is given by the difference in the kinetic energy of the dissociating molecule K_i and the energy to dissociate D_i. Indirect DPI of H_2 via process (3), through lowest Q_1 states leads to H_2^+ ion in the $X\,^2\Sigma_g^+\left(1s\sigma_g\right)$ state. The dissociating molecule in the Q_1 doubly excited state transitions through the Q_1 state with a kinetic energy K_1 (as indicated in Fig 5 d), to end up at a larger inter-nuclear distance . The molecule autoionizes from this point, for the H_2^+ ion to be in the $X\,^2\Sigma_g^+\left(1s\sigma_g\right)$ state. The energy then required by the H_2^+ ion to dissociate from this point to the final products as shown in process equation (3) is given by D_1. KER in this case is then the difference between the energies K_1 and D_1. KER_1 in Fig 5 e is derived in the same manner where DPI occurs via Q_2 state and the dissociation products as shown in process (4).

It should be noted that in case of the indirect process (5) where *resonant DPI* occurs through the lowest Q_2 states, KER_2 is given by the sum of the kinetic energy K_{2A} of the dissociating molecule to transition through the Q_2 state ending up at a larger inter-nuclear distance and K_{2B} being the kinetic energy of the molecule to dissociate to the dissociative ionization threshold, thus requiring no more energy needed for the ion to the dissociate to the $^2\Sigma_u^+\left(2p\sigma_u\right)$ state.

Thus, as seen in Fig 5 d and 5 e, it is possible that the ejected photoelectron energies depend critically on the R at the moment of autoionization and hence it is possible to have electrons of very similar energies due to different decay processes, giving rise to interference effects. In case of process (3) and (4), the photoionization not only occurs via experimentally indistinguishable routes, but it is also possible that the ejected photoelectrons would have the similar energies depending on the inter-nuclear distance R at which the autoionization occurs.

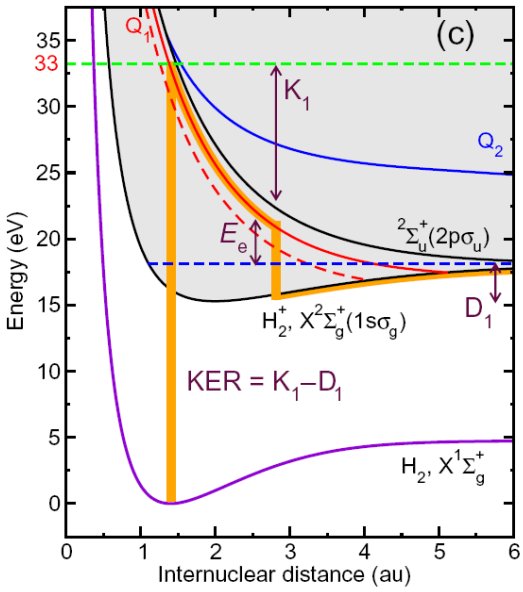

Fig 5 d: Semiclassical pathway for DPI [1] of H_2 shown via process (3) $h\nu$ = 33 eV, where resonant dissociative ionization through lowest Q_1 states leads to H_2^+ ion in the $X\,^2\Sigma_g^+(1s\sigma_g)$ state.

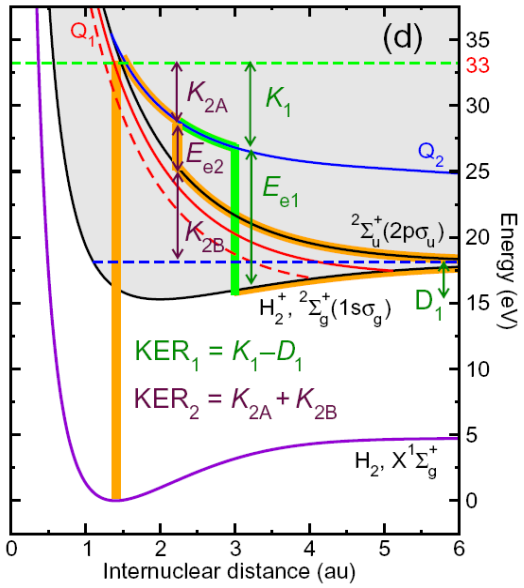

Fig 5 e: Semiclassical pathway for DPI [1] of H_2 via process (4) (shown in green) & (5) for $h\nu$ = 33 eV, where resonant DPI through the lowest Q_2 states leads to either the H_2^+ $^2\Sigma_g^+(1s\sigma_g)$ or $^2\Sigma_u^+(2p\sigma_u)$ state respectively.

5.3 PHOTOELECTRON ASYMMETRY PARAMETER (β) MEASUREMENTS

5.3.1 EXPERIMENT

The β parameters in this DPI study of H_2 were measured using an electrostatic toroidal photoelectron spectrometer, whose details are given elsewhere [4, 5] and in Chapter 2. The spectrometer was oriented so that electrons emitted at 0° and 90° to the polarization axis were both included in the final energy-resolved and angle-dispersed image. The toroidal spectrometer was used in conjunction with linearly polarized synchrotron radiation on the VLS-PGM (undulator) beamline at the Canadian Light Source.

When using linearly polarized light, the emission of photoelectrons from a random distribution of atoms or molecules has a characteristic differential cross section that is expressed in terms of an asymmetry or β parameter [6] as:

$$\frac{d\sigma}{d\Omega} = \frac{\sigma}{4\pi}\left[1 + \beta P_2(\cos\theta)\right] = \frac{\sigma}{4\pi}\left[1 + \frac{\beta}{2}\left(3\cos^2\theta - 1\right)\right] \quad (6)\ ; \text{ where,}$$

$$P_2(\cos\theta) = \frac{3}{2}\cos^2\theta - \frac{1}{2}$$

Here σ is the photoionization cross section for a particular ionic state and θ is the angle between the polarization axis, $\hat{\varepsilon}$, and the direction of the ejected electron. The asymmetry parameter β depends on the wave functions of the partial waves of the outgoing electrons and the phase shift between them [7]. Thus, the variation of β with photoelectron energy depends on the partial waves which contribute to the final channel and is therefore a sensitive probe of the photoionization dynamics. The energy variation in β is generally gradual and β lies within the range $2 \geq \beta \geq -1$, the limits corresponding to $\cos^2\theta$ and $\sin^2\theta$ distributions respectively. In direct photoionization there is only one distinguishable possible route (no interference between decay channels) and thus the β is generally slowly varying with photon (and hence photoelectron) energy. However, when

photoionization occurs via experimentally indistinguishable routes, such as directly (1) and via intermediate neutral states (3, 4), this can give rise to dramatic changes in both the partial cross section *and* the angular distribution of the photoelectrons as a function of photon/photoelectron energy.

Electrons emitted in the plane orthogonal to the photon beam are focused onto the entrance slit of the toroidal analyzer by cylindrical slit lenses (see Fig 5 f). They are then energy analyzed and emerge from the toroidal exit slit to be focused on to a 2-dimensional position-sensitive detector by a conical lens. The focusing properties of the toroidal analyzer [8] enable the initial angles of emission to be mapped onto the detector so that the final images are circular arcs with their centers on the photon beam axis.

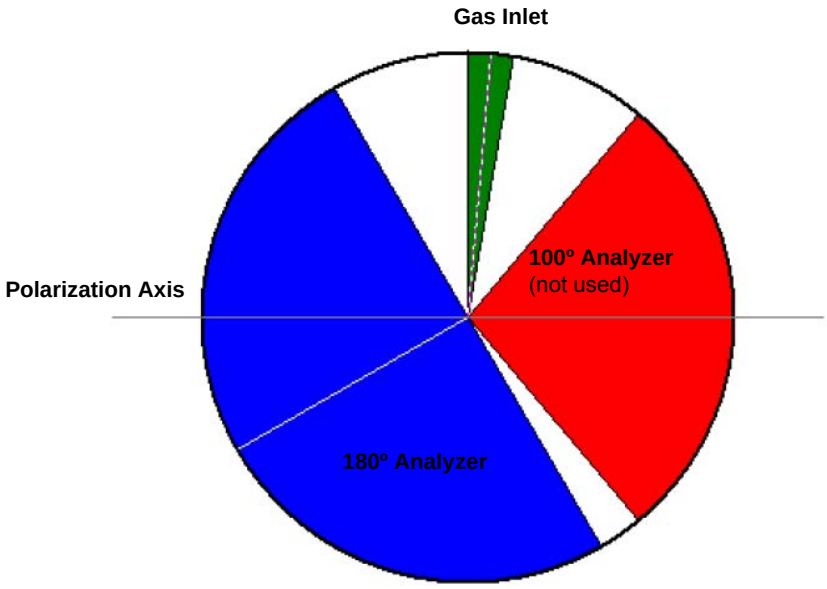

Fig 5 f: Orientation of the 180º analyzer with respect to the polarization axis and hypodermic gas needle. The smaller 100º analyzer was not used for the H_2 experiment.

The photon energy resolution was ~10 meV at ~33 eV. The angular resolution depends on the geometry and focusing properties of the toroidal analyzer and electron lenses. This

has previously been determined to be ± ≈2.5° from helium photodouble ionization studies (Wightman *et al* [9]) where the angular distribution varies more rapidly with angle than in single ionization. The (angle-averaged) electron energy resolution was measured as ≈ 100 meV (FWHM) using He^+ ($n = 2$) photoelectrons.

The toroidal spectrometer as seen in Fig 5 g -a), has its symmetry axis about the photon beam direction, $\hat{k}_\gamma$, not the polarization axis $\hat{\varepsilon}$. The expression in Eqn (6) is for 100% linearly polarized light where θ is defined with respect to $\hat{z} \equiv \hat{\varepsilon}$ hence one needs to express Eqn (6) in the frame where $\hat{z}$ is along $\hat{k}_\gamma$ (Fig 5 g- b)

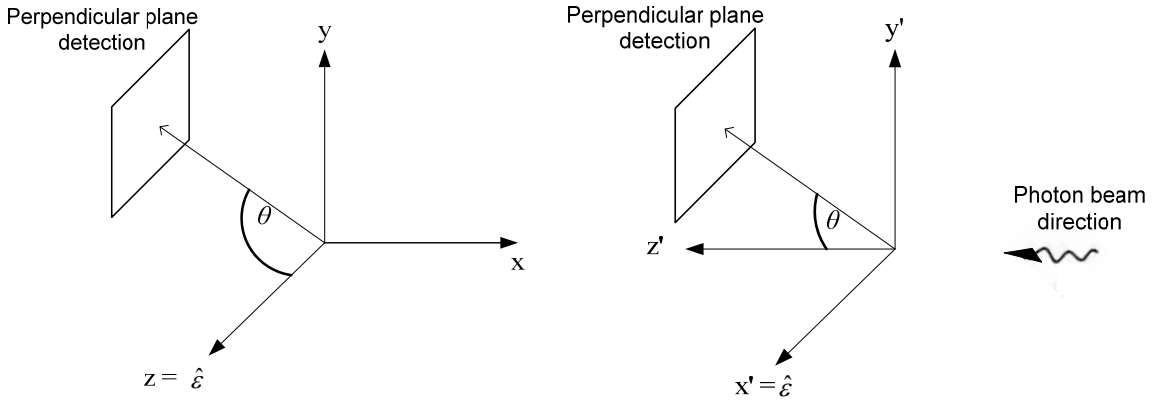

Fig 5 g: a) Coordinate frame of reference for the standard equation (6) for a 100 % linearly polarized light where θ is defined with respect to $\hat{z} \equiv \hat{\varepsilon}$. b) Frame is rotated around y axis to represent the experimental frame of reference where θ is now defined with respect to $x' \equiv \hat{\varepsilon}$ and z' is rotated to align with the direction of the photon beam.

Using the standard equations given in [10] for differential cross-sections for linearly polarized light, one can modify Eqn (1) to incorporate S_1:

$$\frac{d\sigma(\theta,\phi)}{d\Omega} = \frac{\sigma}{4\pi}\left[1 + \frac{\beta}{2}\left(3S_1 \sin^2\theta\cos^2\phi - 1\right)\right] \qquad (7)$$

Eqn (7) represents the current experimental reference frame where z is along $\hat{k}_\gamma$.

5.3.2 DATA ACQUISITION AND ANALYSIS

The spectrometer was used in the non-coincidence mode [Chapter 3 Sec 3.3.1], where the angle-dispersed photoelectron yield is recorded at each photoelectron energy. Hence, to measure the β parameter over a span of electron/ion energies, the photon energy was kept fixed and the collection energy of the toroidal analyzer (180º) was varied (Fig 5 f). At each electron/ion collection energy, the angle dispersed images were collected for a fixed number of buffers i.e. 100 buffers (~25,600 counts) in this case. Although, the accumulated number of counts for each energy was the same, the data accumulation time was different as this depended on the photoionization cross section and experimental variables such as photon flux, gas pressure, photon/electron resolutions. Thus, the statistical quality of the data for this method of comparing the angular distributions is uniform. The raw images are processed and the angular distributions are histogrammed in 5º intervals.

The experimental goal was to plot the photoelectron β parameter (for constant photon energy) as a function of photoelectron energy (E_k). The angle dispersed images were recorded for electron energies at ΔE_k = 0.2 eV intervals i.e. double the analyzer resolution. For a given photoelectron energy (calibration point), β_{H_2} parameter was calibrated with He (n = 1, β = 2) image. With a known β_{E_k} for photoelectron energy E_k, the β parameter for the consecutive photoelectron energies $E_k + \Delta E_k$ was then obtained by taking ratios of the angular distributions of the images for consecutive electron energies to measure $\beta_{E_k+\Delta E_k}$.Hence, this method involved taking the ratio of angular distributions of two separate processes that had different β's and different photoionization cross sections σ's. However, the data accumulation was obtained under the same spectrometer tuning conditions and polarization state, S_1.

Using basic trigonometric identities Eqn (7) can then be re-written as :

$$\frac{d\sigma(\theta,\phi)}{d\Omega} = \frac{\sigma}{4\pi}\left[1+\frac{\beta}{4}(1-3S_1)+\frac{3}{2}\beta S_1 \sin^2\theta\cos^2\phi-\frac{3}{4}\beta(1-S_1)\cos^2\theta\right] \quad (8)$$

where ϕ is the azimuthal angle, whose origin lies on the major axis of the polarization ellipse. In order to compare the yield from two processes, Eqn (8) needs to integrated over the detection solid angle $d\Omega = sin\theta\ d\theta\ d\phi$. First integrating over $\theta = 90^\circ - \delta\theta \rightarrow 90^\circ + \delta\theta$ corresponding to the detection geometry, where $\delta\theta$ is the effective half-angle of the acceptance lens for all azimuthal angles gives:

$$\frac{d\sigma(\phi)}{d\phi} = \frac{\sigma}{4\pi}2\sin(\delta\theta)\left[1+\frac{\beta}{4}(1-3S_1)+\frac{3}{2}\beta S_1\cos^2\phi-\frac{\beta}{4}\sin^2(\delta\theta)\left[1-S_1+2S_1\cos^2\phi\right]\right] \quad (9)$$

It should be noted that the third term in the square brackets vanishes to negligible terms within the small angle approximation, appropriate in this case as $\delta\theta \sim 5°$. Second integration is now performed over $\phi = \phi_1 \rightarrow \phi_2$ which gives:

$$\int_{\phi_1}^{\phi_2}\sigma = \frac{\sigma}{4\pi}2\,sin(\delta\theta)\left[\Delta\phi\left(1+\frac{\beta}{4}\left(1-sin^2(\delta\theta)\right)\right)+\frac{\beta S_1}{8}\left(3-sin^2(\delta\theta)\right)\left(sin(2\phi_2)-sin(2\phi_1)\right)\right] \quad (10)$$

where $\Delta\phi = \phi_2 - \phi_1$ is in radians. It should be noted here that when $\sin(2\phi_2) = \sin(2\phi_1)$, such as when $\phi_2 = n\pi/2$ and $\phi_1 = 0$, then the second term disappears.

In this experiment, the ratio of angular distributions of two separate processes can thus be obtained by taking the ratio of Eqn 9 and incorporate experimental variables, l_i, N_i, t_i as defined below. However, by omitting the terms of order $sin^2(\delta\theta)$ within the square brackets, since $\delta\theta \sim 5°$ in this application, the ratio simplifies to:

$$\frac{I_1(\phi)}{I_2(\phi)} \cong \frac{\sigma_1 n_1 l_1 N_1 t_1}{\sigma_2 n_2 l_2 N_2 t_2} \frac{\left[1+\frac{\beta_1}{4}(1-3S_1)+\frac{3}{2}\beta_1 S_1 \cos^2\phi\right]}{\left[1+\frac{\beta_2}{4}(1-3S_1)+\frac{3}{2}\beta_2 S_1 \cos^2\phi\right]} \quad (11)$$

where

$n_i \rightarrow$ is the target number density,

$l_i \rightarrow$ is the interaction length,

$N_i \rightarrow$ is the number of photons per second and

$t_i \rightarrow$ is the data accumulation times for each experimental measurement.

This expression is independent of $sin(\delta\theta)$ showing that the ratio is insensitive to small variations of $\delta\theta$ with ϕ that may arise from alignment errors in the apparatus.

Even if β_1 is a known calibrant, $\frac{\sigma_1 n_1 l_1 N_1 t_1}{\sigma_2 n_2 l_2 N_2 t_2}$ is a difficult quantity to experimentally determine with accuracy and seriously limits the precision in determining β_2 when fitting the measured ratio to Eqn(11). However, if one accumulates data for *equal number of counts*, rather than time, then integrated yield over the whole detection solid angle $(\delta\theta, \Delta\phi)$ will be the same. According to Eqn (10) and by again, ignoring the $sin^2(\delta\theta)$ within the square brackets, one obtains the following expression:

$$\frac{\sigma_1 n_1 l_1 N_1 t_1}{\sigma_2 n_2 l_2 N_2 t_2} = \frac{\left[\Delta\phi\left(1+\frac{\beta_2}{4}\right)+\frac{3\beta_2 S_1}{8}\left(\sin(2\phi_2)-\sin(2\phi_1)\right)\right]}{\left[\Delta\phi\left(1+\frac{\beta_1}{4}\right)+\frac{3\beta_1 S_1}{8}\left(\sin(2\phi_2)-\sin(2\phi_1)\right)\right]} \quad (12)$$

Hence Eqn (11) can be re-written as:

$$\frac{I_1(\phi)}{I_2(\phi)} \cong \frac{\left[\Delta\phi\left(1+\frac{\beta_2}{4}\right)+\frac{3\beta_2 S_1}{8}\left(\sin(2\phi_2)-\sin(2\phi_1)\right)\right]}{\left[\Delta\phi\left(1+\frac{\beta_1}{4}\right)+\frac{3\beta_1 S_1}{8}\left(\sin(2\phi_2)-\sin(2\phi_1)\right)\right]} \frac{\left[1+\frac{\beta_1}{4}(1-3S_1)+\frac{3}{2}\beta_1 S_1 \cos^2\phi\right]}{\left[1+\frac{\beta_2}{4}(1-3S_1)+\frac{3}{2}\beta_2 S_1 \cos^2\phi\right]} \quad (13)$$

Interestingly, if $\sin(2\phi_2) = \sin(2\phi_1)$ and $S_1 \equiv 1$, then this expression simply reduces to:

$$\frac{I_1(\phi)}{I_2(\phi)} \cong \left(\frac{4+\beta_2}{4+\beta_1}\right)\frac{\left[1+\frac{\beta_1}{2}\left(3\cos^2\phi-1\right)\right]}{\left[1+\frac{\beta_2}{2}\left(3\cos^2\phi-1\right)\right]} \qquad (14)$$

An expression that is independent of the acceptance angles $\Delta\phi$ and $\delta\theta$ when $\sin^2(\delta\theta) << 1$.

The ratio of the experimental data can now be placed on an absolute scale using Eqn (13), which only depends on S_1 and the two β values, one of which, for instance β_1, could be a calibrant, and the known values of ϕ_1 and ϕ_2. Before performing a fitting procedure, it should be noted that:

a) *All* measured ratio values across the $\Delta\phi$ range contribute to the determination of the unknown β_2.
b) The statistical uncertainties at each ϕ value can be appreciably different, depending on the number of counts in both measurements at that angle.

Therefore a weighted least-squares fit across the entire $\Delta\phi$ range maximizes the precision in determining β_2.

Before proceeding further, one needs to consider that the collected signal is also a function of the efficiency of the analyzer, $\eta(\phi)$, which may vary with azimuthal angle. Although, this function will be cancelled out in the angular part of Eqn (11), it will however be present in Eqns (10, 12) where the yield is integrated over a $\Delta\phi$ range. Eqn (13) is now rewritten to account for the efficiency function as follows:

$$\frac{I_1(\phi)}{I_2(\phi)} \cong \frac{\left[\Delta\phi\overline{\eta}\left(1+\frac{\beta_2}{4}\right)+\frac{3\beta_2 S_1}{4}\int_{\phi_1}^{\phi_2}\eta(\phi)cos(2\phi)d\phi\right]\left[1+\frac{\beta_1}{4}(1-3S_1)+\frac{3}{2}\beta_1 S_1 cos^2\phi\right]}{\left[\Delta\phi\overline{\eta}\left(1+\frac{\beta_1}{4}\right)+\frac{3\beta_1 S_1}{4}\int_{\phi_1}^{\phi_2}\eta(\phi)cos(2\phi)d\phi\right]\left[1+\frac{\beta_2}{4}(1-3S_1)+\frac{3}{2}\beta_2 S_1 cos^2\phi\right]} \quad (15)$$

where $\overline{\eta}$ is the mean efficiency over the $\Delta\phi$ range. Note that if $\eta(\phi)/\overline{\eta} \cong 1$ then this expression reduces to (13). Since the result of the integral within (15) is a constant and the same for both measurements, one can therefore conveniently express the integral as

$$\int_{\phi_1}^{\phi_2}\eta(\phi)\cos(2\phi)d\phi = k\Delta\phi\overline{\eta} = k\int_{\phi_1}^{\phi_2}\eta(\phi)d\phi \qquad (16)$$

where k is a constant defined by this equation that, by inspection, lies between $0 \le |k| < 1$. Consequently Eqn (15) can be rewritten as:

$$\frac{I_1(\phi)}{I_2(\phi)} \cong \frac{\left[\left(1+\frac{\beta_2}{4}(1+3kS_1)\right)\right]\left[1+\frac{\beta_1}{4}(1-3S_1)+\frac{3}{2}\beta_1 S_1 cos^2\phi\right]}{\left[\left(1+\frac{\beta_1}{4}(1+3kS_1)\right)\right]\left[1+\frac{\beta_2}{4}(1-3S_1)+\frac{3}{2}\beta_2 S_1 cos^2\phi\right]} \qquad (17)$$

The efficiency function, $\eta(\phi)$, is obtained using a photoionization process with a reliably known β parameter and S_1 for a given photoelectron energy. Hence k can be obtained from (16).

5.3.3 β MEASUREMENTS

Seen in Fig 5 h are the first experimentally presented β oscillations that are shown in comparison with the theoretically predicted oscillations in β as a function of E_k by Fernández and Martín 2009 [1] for randomly oriented H_2 molecules. Furthermore, there is a remarkable agreement in the *phase* and *frequency* of the oscillations at all three photon energies; the only minor exception being at ~13 eV in the $h\nu$ = 35 eV data.

There is, however, a general discrepancy in the amplitude of the oscillations in Fig 5 h which requires comment. Firstly, the theoretical curve is not convoluted with the experimental photoelectron energy resolution, namely ≈100 meV (FWHM). Incorporating this would reduce the amplitude of the oscillations. Secondly, and more importantly, there is further experimental issue which *systematically* alters the absolute β values below E_k ~ 10 eV, namely the contribution due to low energy 'background' electrons. It is well known that energetic photoelectrons, in this case from the H_2^+ $^2\Sigma_g^+\left(1s\sigma_g\right)$ ground state, undergo inelastic collisions with metal surfaces near the interaction region. The detected electron yield at a given E_k will inevitably contain a background contribution from this photo-induced process and, unfortunately, the signal-to-noise ratio gets progressively worse as one reduces E_k towards 0 eV. These background electrons are not isotropic, since they arise from photoelectrons with a high β, but their β variation with E_k has no structure. The effect of this increasing background contribution with decreasing E_k is to suppress the *amplitudes* of the observed β oscillations, but this does not alter the *phase* and *frequency* of the β oscillations. This background electron issue will fade away for E_k > ~10 eV and therefore the reason for the observed discrepancy in the β values is unclear in this E_k region.

It can also be seen in Fig 5 h that the β values at each observed peak are significantly lower than the corresponding theoretical value. Measurements by Parr *et al* [13] show that the vibrationally averaged (non-dissociative) β values for $h\nu$ = 31, 33, and 35 eV are approximately 1.9, 1.75 and 1.6, respectively, corresponding to the high E_k 'limit'.

There is, therefore, a body of experimental evidence that suggests β at high E_k values is significantly lower than β = 2.0 of the united atom limit – helium – and of the H_2 theoretical results. Further work is needed to address this issue.

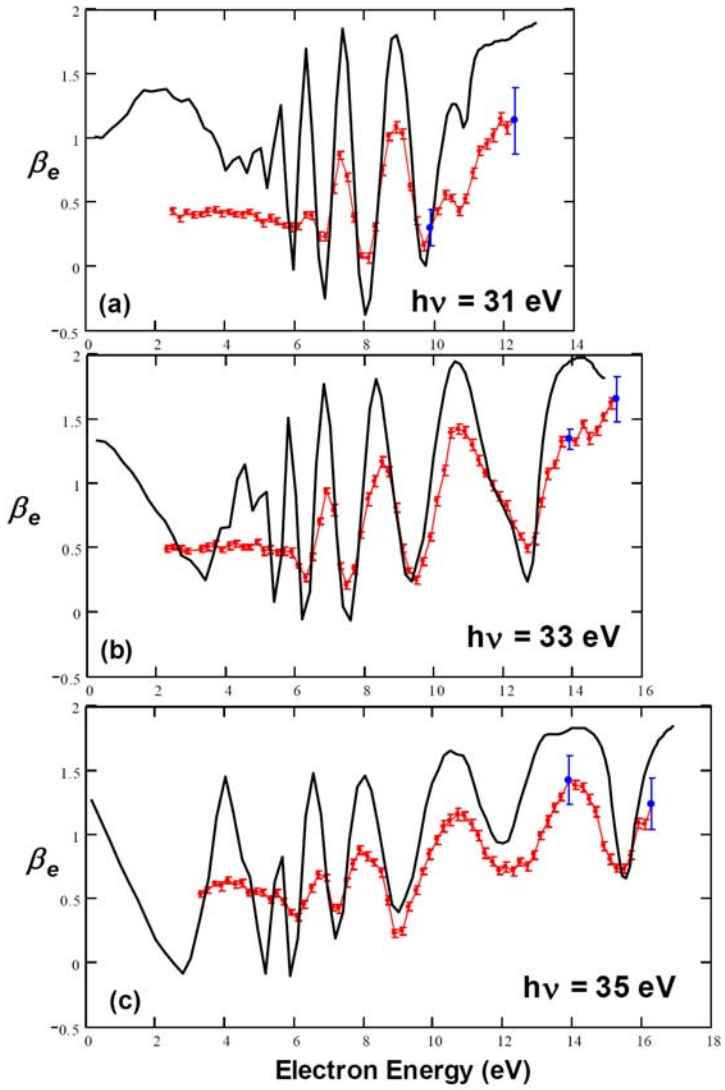

Fig 5 h: The electron asymmetry parameter,β, variation with energy for the $h\nu$ = 31, 33 and 35 eV. The theoretical curves- close coupling calculations (black) oscillations and the measured data (red) are shown. The error bars on the calibration points (blue) at 9.9 and 13.9 eV indicate the uncertainty in the overall β scale; the *relative* statistical uncertainty is shown in the smaller (red) error bars. The (blue) error bars for the highest photoelectron energies are a combination of the β scale uncertainty and the statistical uncertainty associated with the sequential ratio fitting procedure.

5.3.4 DATA ANALYSIS PROCEDURE

The β_{H_2} spectra presented in Fig 5 h are placed on an absolute scale by performing a weighted least squares fit using (17) of the observed ratio of the $I_{H_2}(\beta_{H_2},\phi)/I_{He}(\beta_{He},\phi)$ yield. The calibrant used to determine β_{H_2} was He (n = 1), β = 2 angular distribution that using the same spectrometer tuning conditions at each E_k. This was done for selected photoelectron energies, namely E_k = 13.9 eV (for $h\nu$ = 33, 35 eV) and 9.9 eV (for hν = 31 eV). By performing angle-integrated photoelectron spectra (PES), it was ascertained that the background counts were essentially zero at all ϕ angles at relatively high E_k values. Consequently, $\beta_{H_2} \pm \delta\beta_{H_2}$ at these E_k values was obtained, as shown in the figure, where $\delta\beta_{H_2}$ corresponds to the uncertainty in the *absolute* scale.

Beginning with the calibration point of E_k = 13.9 eV, the *variation* of β_{H_2} with E_k was found by *sequentially* performing a weighted least squares fit using (17) of the observed ratio of the $I_{H_2}((E_k \pm \Delta E_k), \beta_{E_k \pm \Delta E_k}, \phi)/I_{H_2}(E_k, \beta_{E_k}, \phi)$ yield, where ΔE_k = 0.2 eV. Fig 5 i shows the fitting procedure performed for $h\nu$ = 31 eV at sample photoelectron energies. The spectrometer tuning conditions are assumed to be essentially the same at each pair of photoelectron energies, since ΔE_k is small, i.e a ~2% change in E_k at E_k ~ 10 eV. This, in turn implies the net efficiency term, k, defined in (17) is the same in both cases. In fact, it is found, as expected, that k varies very slowly with E_k. For a given β_{E_k}, the uncertainty in $\beta_{E_k \pm \Delta E_k}$ from the least squares fitting process lies typically between ±(0.02 –0.06), which corresponds to the *relative* uncertainty of the 'channel-to-channel' β_{H_2} variations.

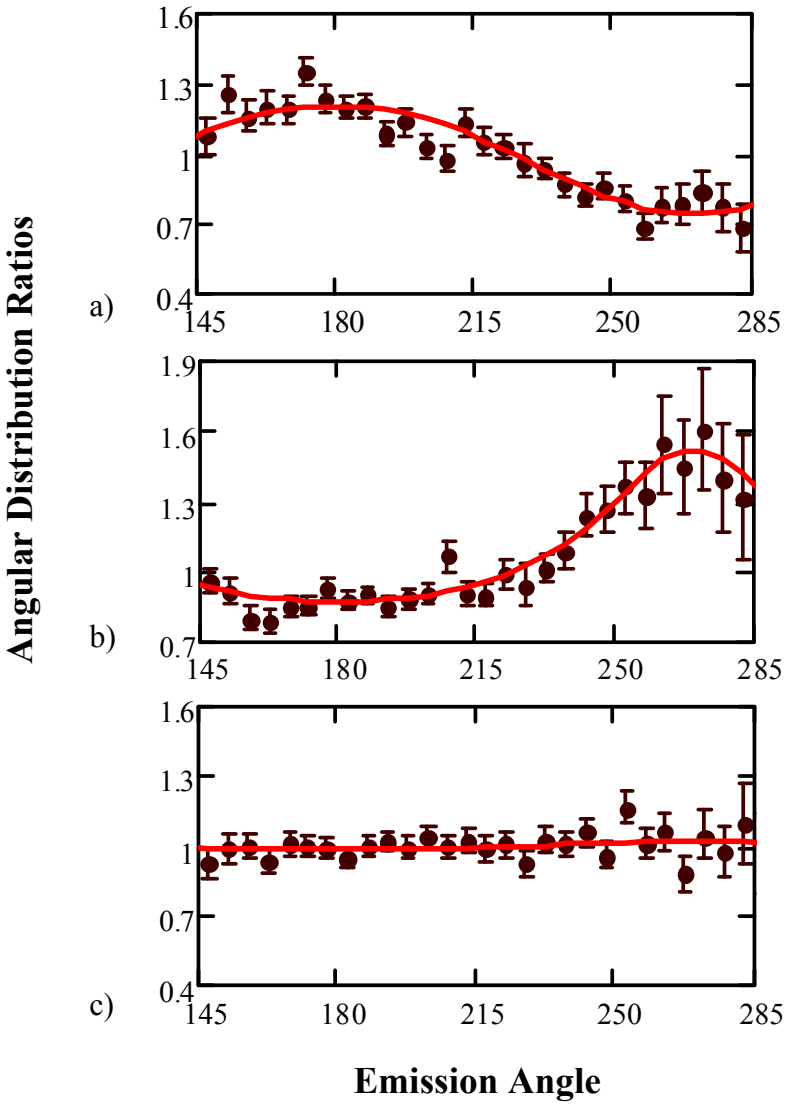

Fig 5 i: Ratio of angular distributions of the experimental data fitted with weighted least squares fit using (17). β ratio fitted for $h\nu = 31$ eV at photoelectron energies, a) 6.84 eV and 6.64 eV b) 5.44 eV and 5.24 eV c) 9.04 eV and 8.84 eV

5.4 THEORY

From theoretical details of the DPI processes occurring at $h\nu$ = 33 eV, it should be noted that ionization is effectively possible through the $^2\Sigma_g^+(1s\sigma_g)$ and $^2\Sigma_u^+(2p\sigma_u)$ ionization thresholds over a wide range of proton/electron energies. Fernández and Martín [1] have published close coupling calculations of electron and ion asymmetry parameters (β) for 33 eV that showed rapidly changing (β) as a function of electron/proton energy for randomly oriented H_2 molecule [1].

The theoretical method employed by Fernández and Martín [1] for the description of molecular continuum states uses B-spline basis sets [16]. For diatomic molecules, this method allows for an accurate description of the ionization continuum, including resonance effects due to electron correlation (Feshbach resonances) and dissociation. For a given energy, there is a continuum state for each electronic state of the residual H_2^+ ion and angular momentum l of the ionized electron. For every value of inter-nuclear distance R, the resulting continuum states from close coupling calculations satisfy the usual incoming boundary conditions corresponding to

(i) one electron in a bound electronic state of H_2^+ and

(ii) the other electron in a single outgoing spherical wave with a well-defined value of the angular momentum l and a combination of incoming spherical waves for all accessible electronic states of H_2^+ and all possible values of the angular momentum of the ejected electron compatible with the molecular symmetry [16].

Therefore, all calculated wave functions include electron correlation and the two-centre character of molecular potential. In addition, final wave function accounts for interferences among the various ionization thresholds and angular momenta of the ejected electron.

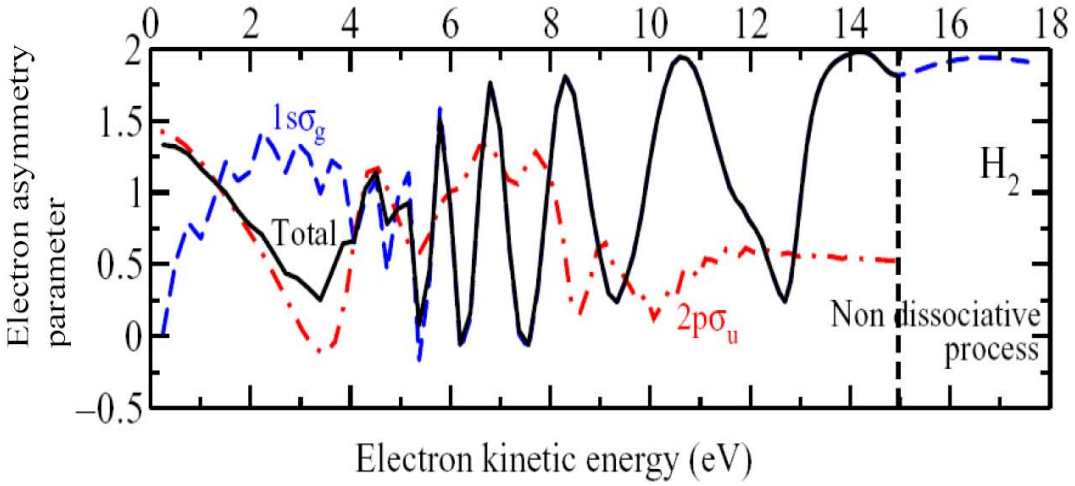

Fig 5 j: Electron asymmetry parameter as a function of electron energy for H_2 obtained for $h\nu$ = 33 eV. The contribution from the first two ionization thresholds is also included: blue dashed line, $1s\sigma_g$ contribution; red dot-dashed line, $2p\sigma_u$ contribution.

In Fig 5 j, the β parameters calculated for $h\nu$ = 33 eV include contributions from a total of 24 Q_1 and Q_2, doubly excited states i.e. 12 of each state, with 6 each of $^1\Sigma_u^+$ and $^1\Pi_u$ symmetry. It can be noted that the β parameter oscillates strongly for electron energies greater than 6 eV and total electron β parameter is essentially identical to the $1s\sigma_g$ channel. For electron energies $\leq$ 6 eV the total β parameter is dominated by the $2p\sigma_u$ channel. At this photon energy, the photoelectron beta parameter has been measured by Lafosse *et al* [11], which is discussed in the next section.

5.4.1 REVIEW AND COMPARISON WITH THEORETICAL AND EXPERIMENTAL STUDIES

There has been a body of experimental and theoretical work that have implied the role of interference between the $Q_1\,^1\Sigma_u^+$ and $Q_2\,^1\Pi_u$ doubly excited states of H_2. Most of these studies have been for an aligned H_2 molecule, the significant studies

performed in photon energy region where both the Q_1 and Q_2 doubly excited states are accessible are highlighted in this section.

In their landmark study Lafosse *et al* [11], examine DPI of the H_2 molecule in the molecular frame. Molecular frame photoelectron angular distributions (MFPAD) for DPI of H_2 in the region of Q_1 and Q_2 doubly excited states were obtained. It was found in this study, that $\beta \approx 1 \pm 0.1$ (for 0 eV $\leq E_k \leq$ 5 eV) and $\beta \approx 0.15 \pm 0.1$ (for 5eV $\leq E_k \leq$ 10 eV) at $h\nu$ = 32.5 eV. While the averaging over a broad E_k is inherent in the MFPAD coincidence technique, their findings are in good agreement with the theoretical work. By integrating the theoretical angular distributions for $h\nu$ = 33 eV in the same electron energy ranges, averageβ's of 1.16 and 0.2, are obtained respectively. These values agree reasonably well with the experimental values.

Another significant MFPAD-DPI study of H_2 has been of Hikosaka and Eland [12]. In their study, they find the β values at $h\nu$ = 21.2, 23.1, 26.9 and 40.8 eV lie between 1.83→1.69 (± 0.05). More recently, Dowek e*t al* [14] presented a circular dichorism *i.e.* the differential absorption of left and right circularly polarized light, study of H_2. By means of experiments and theoretical calculations, they show the presence of circular dichorism when the MFPADs are integrated over electron emission angles with respect to molecular axis *i.e.* polar emission angle, in the case of resonant DPI of H_2 in the region where *hυ* = 30-35 eV. They conclude that their observation of circular dichorism in H_2, a homonuclear molecule in the photoelectron angular distributions is the signature of delayed autoionization ($Q_1{}^1\Sigma_u^+$ and $Q_2{}^1\Pi_u$ states) into channels of different inversion symmetry (*i.e.* $1s\sigma_g$ and $2p\pi_u$).

Theoretical and experimental work by Martin *et al* [2] show that the photoelectron angular distribution with respect to the polarization axis for $h\nu$ = 33.25 eV varies with KER ≅ 8 to 10 eV, corresponding to an electron energy of E_e ≅ 5 to 7eV. The $1s\sigma_g$ and $2p\pi_u$ channels overlap in the 8 to 10 eV region and this is the regions where the largest asymmetry is observed.

Studies have also been performed at higher photon energies and one of the significant studies here have been of Ito *et* al [15]. They have measured the angular distributions of photoelectrons for H_2 molecule aligned perpendicular to the polarization to an ionic state with an energy of 38 eV in the photon energy range 44–76 eV. It is shown in their work, that angular distribution is isotropic for ionization into the $2s\sigma_g$ and $2p\pi_u$ states of H_2^+ at low electron energy and is anisotropic at higher photon energies, where the electron emission was preferentially in the direction perpendicular to the molecular axis. The transition of the angular distribution patterns is explained in terms of the competition of direct photoionization to the $2s\sigma_g$ and $2p\pi_u$ states of H_2^+, i.e. possibly indicating that the $s\sigma_g$ and $p\pi_u$ partial waves play an important role.

5.4.2 EXPLANATION OF THE OBSERVED *(AND PREDICTED)* β OSCILLATIONS

As mentioned in section 5.2, there are five competing process that lead to DPI in the energy region $h\nu = 31 - 35$ eV. They are:

$$h\nu + H_2\left(X\,^1\Sigma_g^+\right) \rightarrow H_2^+\,{}^2\Sigma_g^+\left(1s\sigma_g\right) + e^- \rightarrow H^+ + H\left(1s\right) + e^- \quad (1)$$

$$h\nu + H_2\left(X\,^1\Sigma_g^+\right) \rightarrow H_2^+\,{}^2\Sigma_u^+\left(2p\sigma_u\right) + e^- \rightarrow H^+ + H\left(1s\right) + e^- \quad (2)$$

$$h\nu + H_2\left(X\,^1\Sigma_g^+\right) \rightarrow H_2^{**}\left(Q_1\,^1\Sigma_u^+, {}^1\Pi_u\right) \rightarrow H_2^+\,{}^2\Sigma_g^+\left(1s\sigma_g\right) + e^- \rightarrow H^+ + H\left(1s\right) + e^- \quad (3)$$

$$h\nu + H_2\left(X\,^1\Sigma_g^+\right) \rightarrow H_2^{**}\left(Q_2\,^1\Sigma_u^+, {}^1\Pi_u\right) \rightarrow H_2^+\,{}^2\Sigma_g^+\left(1s\sigma_g\right) + e^- \rightarrow H^+ + H\left(1s\right) + e^- \quad (4)$$

$$h\nu + H_2\left(X\,^1\Sigma_g^+\right) \rightarrow H_2^{**}\left(Q_2\,^1\Sigma_u^+, {}^1\Pi_u\right) \rightarrow H_2^+\,{}^2\Sigma_u^+\left(2p\sigma_u\right) + e^- \rightarrow H^+ + H\left(1s\right) + e^- \quad (5)$$

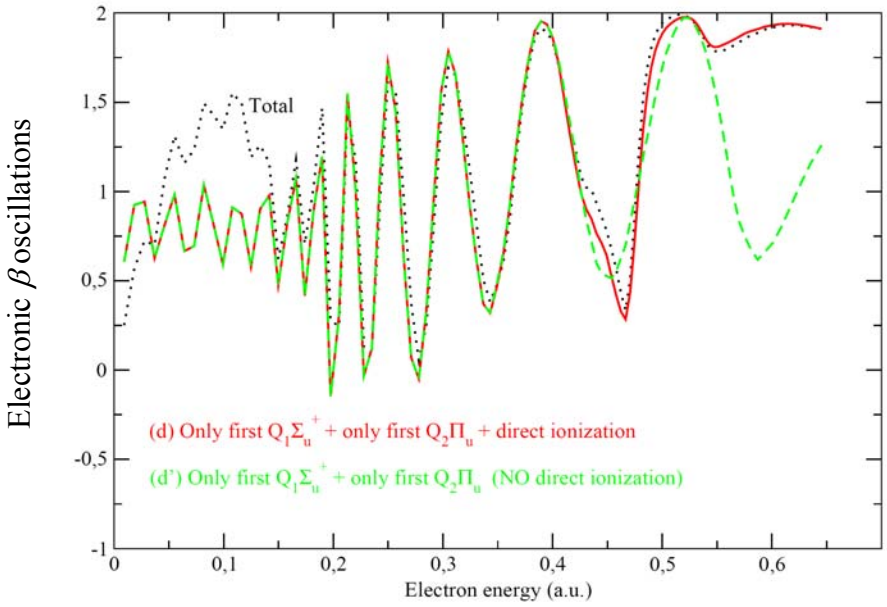

Fig 5 k: Calculated β oscillations for $h\nu = 33$ eV verifying the involvement of direct and indirect DPI processes in producing the oscillation. The figure proves that the oscillations are mainly due to the interference between the autoionizing states, $^1Q_1{}^1\Sigma_u^+$ (process (3)) and $^1Q_2{}^1\Pi_u$ states (processes (4,5)) . Black dotted line includes 12 each of $^1Q_1{}^1\Sigma_u$ and $^1Q_2{}^1\Pi_u$ states, while the green dashed line includes only the lowest $^1Q_1{}^1\Sigma_u$ and $^1Q_2{}^1\Pi_u$ state along with the direct ionization process (1) and the red dashed line includes only the lowest $^1Q_1{}^1\Sigma_u$ and $^1Q_2{}^1\Pi_u$ state.

It can be seen from Fig 5 k that there is no significant change in the oscillations with or without the direct ionization channel (process (1)). Further analysis shows that only the lowest Q_1 and Q_2 states need to be considered; in fact the longer lived Q_n states decay to other channels. This implies that the oscillations are mainly due to the interference between the $1Q_1{}^1\Sigma_u^+$ and $1Q_2{}^1\Pi_u$ ionization channels. The oscillations in Fig 5 k are calculated by considering only the lowest Q_1 and Q_2 states, as opposed to 12 of each state in the earlier theoretical work. It is evident that amplitude and phase of the oscillations are synchronous to the earlier calculation, hence implying interference between the lowest Q_1 and Q_2 states sufficient to produce these oscillations.

In order to conserve total parity the electrons ejected from processes (3) and (4) will only have odd numbered ℓ partial waves and electrons ejected via process (5) will have even ℓ partial waves. The effect of the partial waves in the β oscillations at $h\nu = 33$ eV is demonstrated in Fig 5 l. The oscillations are seen only when the $\ell = 1$ partial waves contribute, however with the inclusion of higher order ℓ waves (odd pairs) the nature of the oscillations do not change, just the amplitude. Also, when only even ℓ waves are considered (i.e. process 5), the oscillations are not as dramatic, especially above ~ 6 eV where process (3) and (4) dominate. Hence, for $h\nu$ = 33 eV, it is an excellent approximation to assume only ℓ = 1 partial waves contribute to the ionization/autoionization process.

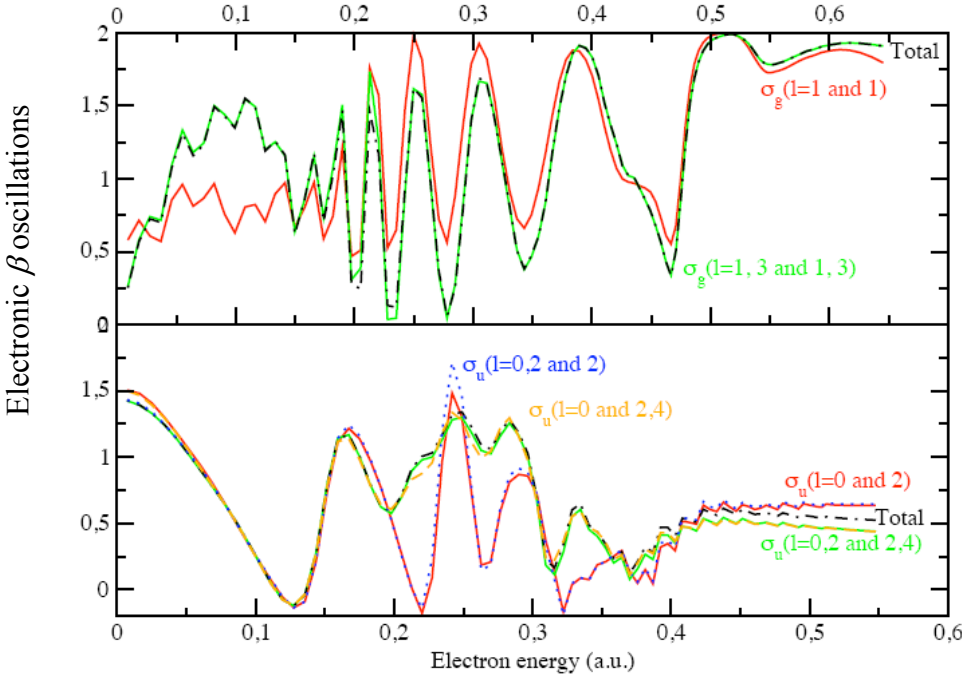

Fig 5 l: Analysis of the involvement of the partial waves in producing the β oscillations $h\nu = 33$ eV Total calculation shown in black line includes all the possible channels.

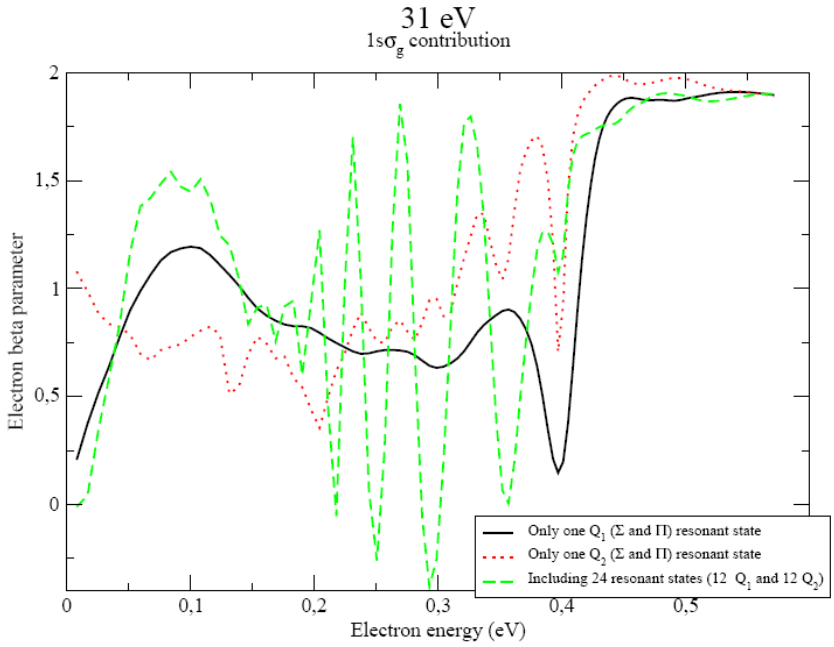

Fig 5 m: Calculated β oscillations for $h\nu$ = 31 eV ; the variation β with respect to electron energy has been plotted for scenario when the contributing resonances are only from the Q_1 resonant state (shown in black), only the Q_2 state (shown in dashed red line) and including contributions from 12 Q_1 states and 12 Q_2 states.

For photon energy of 31 eV, the Q_2 state is excited weakly outside the FC region and hence one still sees oscillations in β (Fig 5 h). This is verified by considering a scenario where only either Q_1 or Q_2 states contribute to the DPI process at this energy and this confirms that this does not lead to the oscillations (see Fig 5 m). At photon energy 35 eV, the Q_1 and Q_2 states are still accessible in the FC region, which lead to the observed oscillations seen in Fig 5 h.

5.5 THEORETICAL MODEL

To reiterate, it has been shown that for $h\nu$ = 33 eV, it is an excellent approximation to assume only ℓ = 1 partial waves contribute to the ionization/autoionization process. Also, considering the ionization to be exclusively through the $^2\Sigma_g^+(1s\sigma_g)$ channel is a good

approximation in the 5-15 eV region. Dehmer and Dill [6], obtain an expression (equation 13 in their paper) for asymmetry parameter β for single ionization of H_2^+ to $2s\sigma_g$ state. The equation is applied here to give:

$$\beta \approx \frac{2}{5\left(D_{p_\sigma}^2 + 2D_{p_\pi}^2\right)}\left(2D_{p_\sigma}^2 + 7D_{p_\pi}^2 + 6\left|D_{p_\sigma}\right|\left|D_{p_\pi}\right|\cos\phi\right) \quad (18)$$

Where, D_{p_σ} and D_{p_π} are the σ and π ionization amplitudes at a given electron kinetic energy E_{e^-} and ϕ is the corresponding phase difference. Theoretical *ab initio* calculations of Fernandez and Martin [1] show that the above amplitudes are comparable in magnitude Hence, for simplicity, we can assume that $\left|D_{p_\sigma}\right| = \left|D_{p_\pi}\right|$ for all energies, such that Eqn (18) simplifies to:

$$\beta(E_{e^-}) \approx \frac{6}{5} + \frac{4}{5}\cos\left[\phi(E_{e^-})\right] \quad (19)$$

From the calculations [1] it is also known that the largest contribution to the D_{p_σ} and D_{p_π} amplitudes is from the $1Q_1\,{}^1\Sigma_u^+$ and $1Q_2\,{}^1\Pi_u$ doubly excited states, respectively, (it can be seen in Fig 5 o; notice also that these states do not lead to any oscillation when considered separately). It is then assumed that ϕ_i is given by the difference between the phases accumulated along the two classical paths depicted in Fig. 5 n (pale blue lines) plus an arbitrary energy-independent phase ϕ_c. Within the semiclassical WKB approximation, the energy dependent contribution is given by:

$$\phi(E_{e^-}) = \int_{R_1^0}^{R_1} dR\, k_\mu^{Q1}(R) + \int_{R_1}^{R_2} dR\, k_\mu^{1s\sigma_g}(R) - \int_{R_2^0}^{R_2} dR\, k_\mu^{Q2}(R) \quad (20)$$

where R_i^0 and R_i are, respectively, the values of the inter-nuclear distance at the beginning of the trajectory ($\omega = E_{Q_i}(R_i^0)$).

At the point where the ejected electrons have energy E_{e^-}, $k_\mu^N(R) = \sqrt{2\mu T_N(R)}$ is the nuclear momentum (μ stands for the reduced mass of H_2^+), and $T_N(R)$ is the nuclear kinetic energy. For $R < R_i$, the latter is given by the difference between the photon energy and the energy of the i autoionizing state at the inter-nuclear distance R. For $R > R_i$, $T_N(R)$ is given by the difference between the photon energy and the sum of the ground state ion and the outgoing electron energies. For the energy independent part of the phase, $\delta_e \sim \pi/2$ is chosen, whose only sizable effect is to shift the position of the maxima and minima of the cosine function. For every energy E_{e^-}, the R_i^0 and R_i values are taken from the calculated curves for the $1Q_1\,^1\Sigma_u^+$ and $1Q_2\,^1\Pi_u$ doubly excited states, respectively (see Fig 5 n).

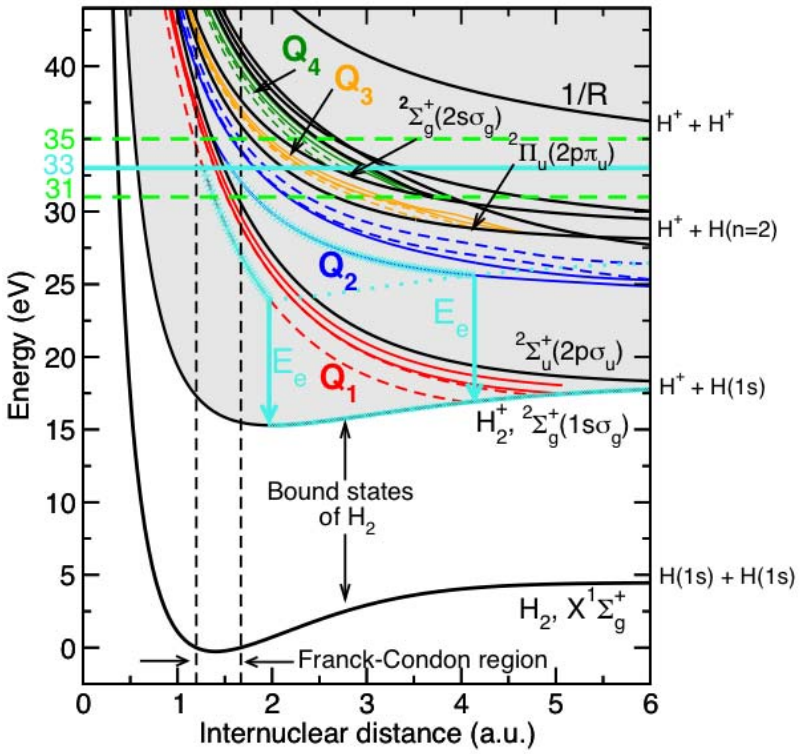

Fig 5 n: The light blue curves on potential energy curves of the H_2 and H_2^+ systems from [1] depict a representative semi-classical pathway to DPI via the lowest Q_1 and Q_2 states, resulting in electrons of identical energies.

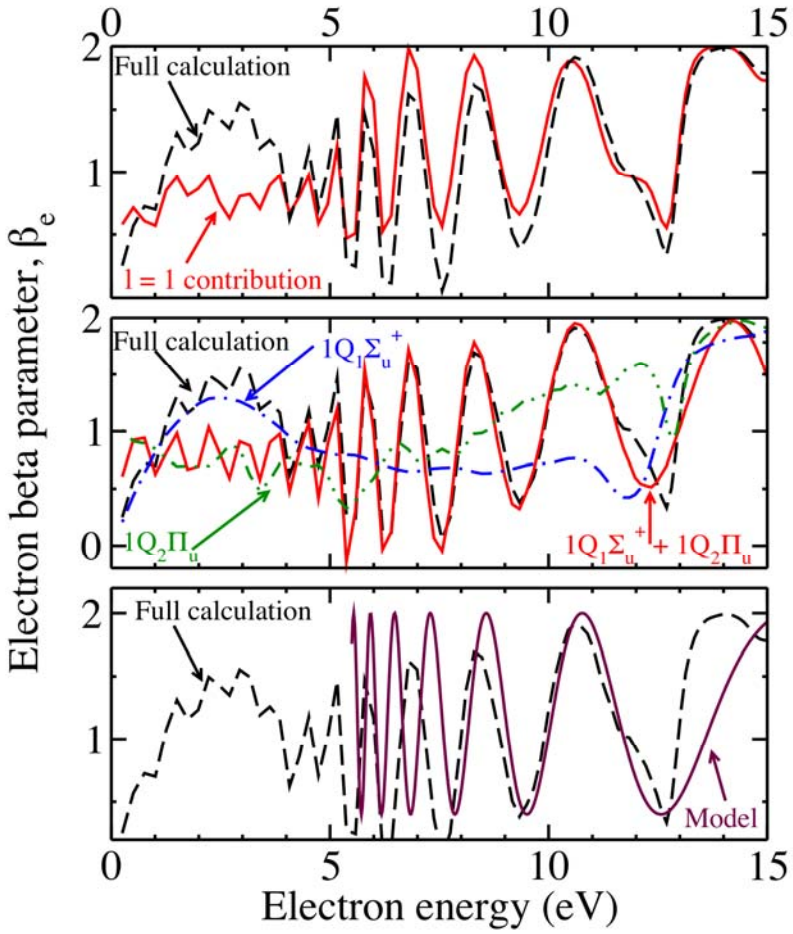

Fig 5 o: The electron asymmetry parameter, β, variation with energy for $h\nu$ =33 eV. The black dashed curve is the result of our full *ab initio* calculations. (a) Top panel shows the dominant ℓ = 1 partial wave contribution. (b) Middle panel shows the individual contributions of the deduced that the largest contribution to the D_{p_σ} and D_{p_π} amplitudes comes from the $1Q_1{}^1\Sigma_u{}^+$ and $1Q_2{}^1\Pi_u$ amplitudes together with their coherent superposition, which gives rise to oscillations in β. (c) Bottom panel shows the results from the simple model presented in the text.

The results of such a model are shown in Fig 5 o (bottom panel). As can be seen, the essence of the oscillatory behavior is reasonably caught. Indeed, the fact that the *difference* between R_1 and R_2 increases (decreases) with proton (electron) energy (see Fig 5 n) leads to an *energy-dependent* frequency of the oscillations in reasonable agreement with the results of the *ab initio* calculations. Therefore, the observed oscillations in the beta parameter as a function of electron energy are the signature of the interference between the $1Q_1{}^1\Sigma_u^+$ and $1Q_2{}^1\Pi_u$ doubly excited states, providing information about the different classical paths followed by the nuclei. The interference effects are observed when photoelectrons are ejected at different inter-nuclear distances R_1 and R_2, such that they have similar energy (see Fig 5 p). The small, systematic changes in the oscillations at different photon energies in Fig 5 q confirm that the same two states are responsible at all three photon energies.

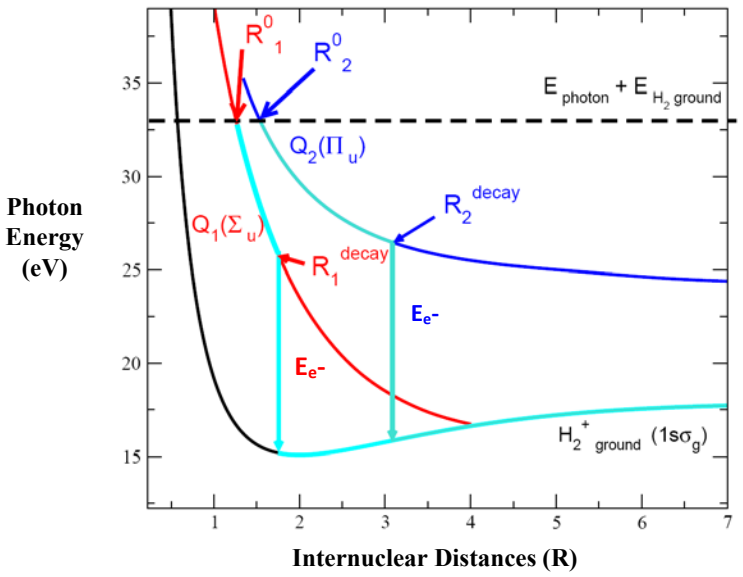

Fig 5 p: Interferences appear when electrons with the same energy are ejected to the same final states in the continua with the same angular momenta. Semiclassical pathways for DPI considering the first Q1 and Q2 states occurring at inter-nuclear distances R_1 and R_2 such that the energy of the ejected electrons, E_{e^-} are similar.

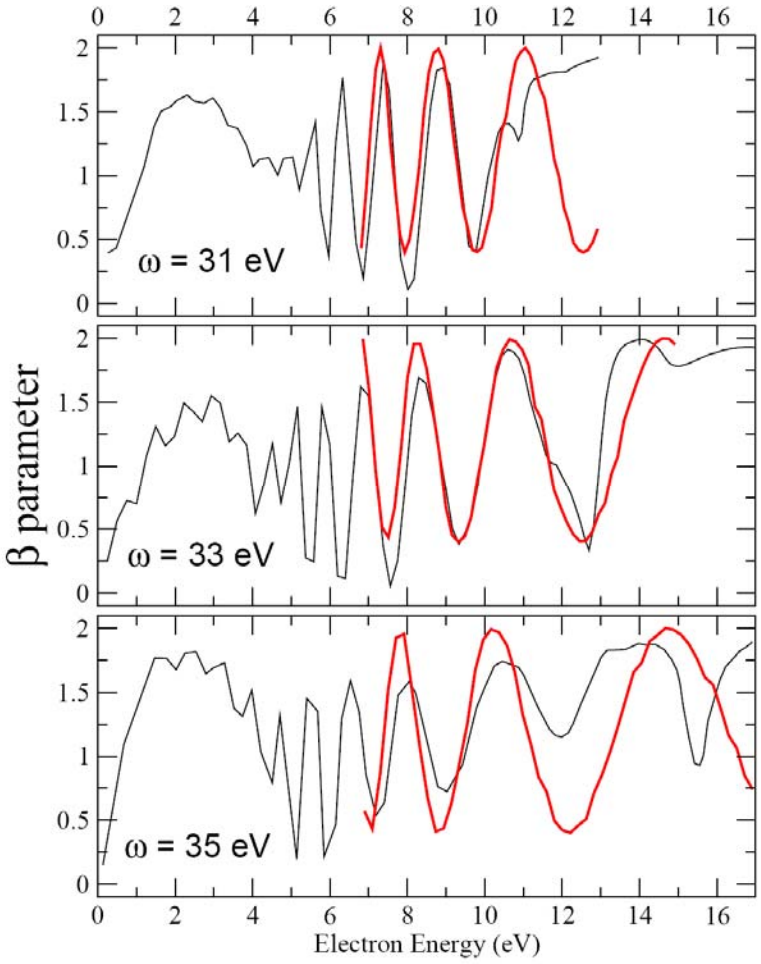

Fig 5 q: Model (red thick line) and full calculations (black thin line) for the electron β parameter at three different photon energies (31, 33 and 35 eV).

5.6 CONSEQUENT β MEASUREMENTS

5.6.1 ELECTRON AND ION β MEASUREMENTS - $h\nu$ = 27eV

At 27 eV, the Q_1 doubly excited states are accessible and the processes that contribute to DPI in this energy region are:

$$h\nu + H_2\left(X^1\Sigma_g^+\right) \rightarrow H_2^+\left(1s\sigma_g\right) + e^- \rightarrow H^+ + H(1s) + e^- \quad (6)$$

$$h\nu + H_2\left(X^1\Sigma_g^+\right) \rightarrow H_2^{+}{}^{**}(Q_1\,{}^1\Sigma_u^+) \rightarrow H_2^+\left(1s\sigma_g\right) + e^- \rightarrow H^+ + H(1s) + e^- \quad (7)$$

$$h\nu + H_2\left(X^1\Sigma_g^+\right) \rightarrow H_2^{+}{}^{**}(Q_1\,{}^1\Pi_u^+) \rightarrow H_2^+\left(1s\sigma_g\right) + e^- \rightarrow H^+ + H(1s) + e^- \quad (8)$$

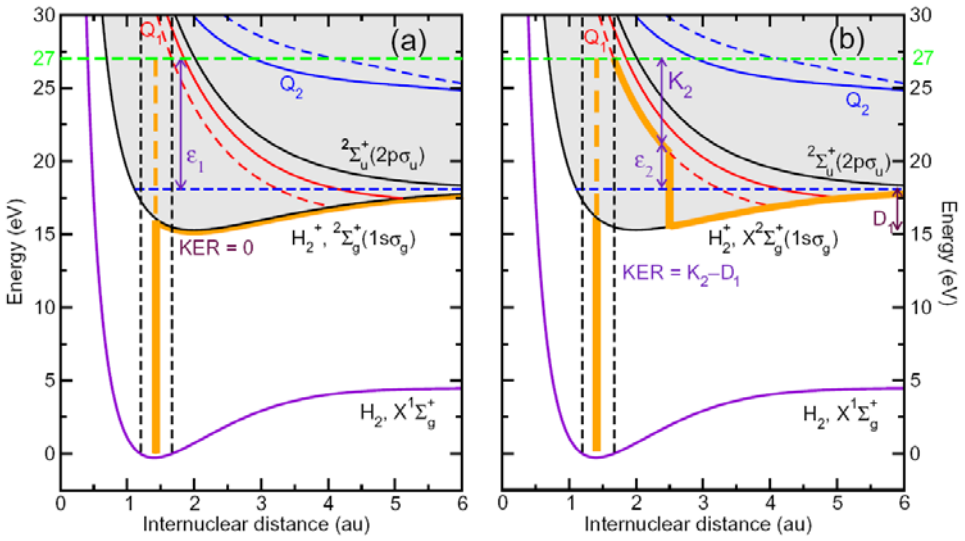

Fig 5 r: Semiclassical pathways for dissociative ionization by absorption of a 27 eV photon. (a) Nonresonant ionization leading to $H_2^+\left(1s\sigma_g\right)$ (process (6) in the text). (b) Resonant ionization through the lowest Q_1 doubly excited states leading to $H_2^+\left(1s\sigma_g\right)$ (process (7) in the text). Q_1 state of $^1\Pi_u$ symmetry is represented by full lines and $^1\Sigma_u^+$ symmetry by dashed lines. Red and blue lines represent the first Q_1 and Q_2 resonant states. The thick vertical line represents a 27 eV vertical transition from the ground state; the dashed part of this line indicates the excess photon energy. The energy carried by the autoionized electron when the residual H_2^+ ion dissociates is indicated by ε_2 [1].

The possible paths to DPI are processes (6), (7) and (8). The equation in process (6) corresponds to a direct DPI process, illustrated by Fig 5 r a). Simultaneously to this direct process, the Q_1 resonant states are populated and, after some time, they autoionize leading to the delayed emission of an electron and to a dissociative H_2^+ nuclear state (Fig 5 r b)). Here again, it is important to note that autoionization can occur well outside the FC region and in a large range of inter-nuclear distances. In Fig 5 r-b), the KER is approximately given by the difference between K_2 (the kinetic energy of the dissociating H_2 molecule in the Q1 state at R = 2.5 au) and D_1 (the energy required to dissociate H_2^+ at R = 2.5 au). Hence, there is a possibility of interference between the Q_1 states of $^1\Pi_u$ and $^1\Sigma_u^+$ symmetry as the resonant DPI occurs.

The calculated electron β as a function of electron energy for $h\nu$ = 27 eV, is shown in Fig 5 r a. The calculations predict slight oscillations between electron energy 2 and 6 eV. For electron energies smaller than 6 eV (proton energies greater than 1.5 eV), the electron is mainly ejected along the molecular axis when it is aligned along the direction of the polarization vector This is because as ionization is dominated by $^1\Sigma_u^+$ symmetry for electrons of this energy and thus, the electron tends to follow the molecular axis. At electron energy of ~ 6.6 eV the situation changes drastically; the electron is ejected perpendicular to the polarization vector, since the contribution of the $Q_1\,^1\Sigma_u^+$ states has a minimum at this energy and hence interference with the Π_u amplitude is largest. The minimum in the $^1\Sigma_u^+$ amplitude is due to the interference between the resonant and non-resonant ionization processes. Therefore, the dip seen in Fig 5 r a at electron energy of 6.6 eV is a consequence of this interference. As the electron energy increases, the non-resonant process dominates and the electron is ejected following the polarization direction. The integrated (over electron/ion energy) theoretical electron (ion) β of 1.85 ± 0.26 is in close agreement with that of Hikosaka *et al* [12], where the experimental β was obtained by integrating over a range of electron energies.

Fig 5 s b shows our preliminary measurements of the electron β as a function of electron energy. The experimental observations for electrons do not show the weak oscillations between electron energy 2 and 6 eV that the calculations predict. This could be attributed to the low energy background noise in this lower energy region, as discussed previously. We do observe the dip in our measurement around ~6.5 eV similar to the theoretical curve, as seen in Fig 5 s a [1].

a)

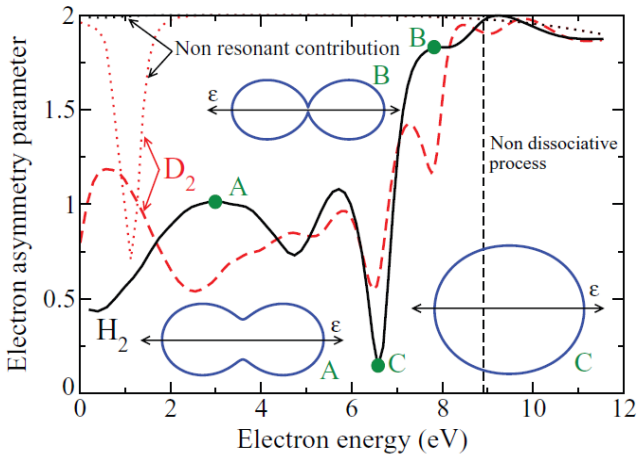

b)

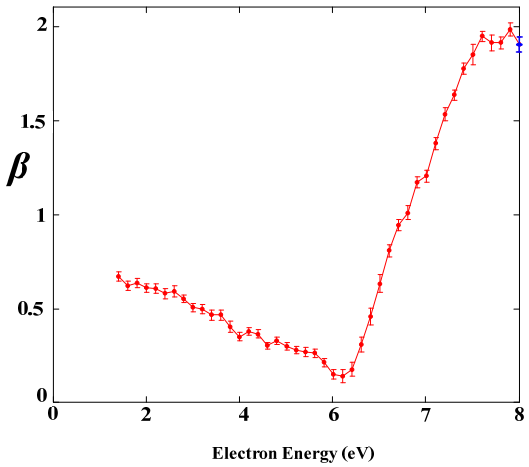

Fig 5 s: a) Calculated β parameter as a function of electron energy for $h\nu$ = 27eV. The results for H_2 are shown by full black. The lobes represent the electron angular distributions at the electron energies labelled by the symbols *A*, *B* and *C*. The non resonant contribution for H_2 shown in dotted black lines. b) Experimental observation of β parameter with the relative statistical uncertainty is shown in the smaller (red) error bars. The (blue) error bar for the highest photoelectron energy is a combination of the β scale uncertainty (using He (n = 1, β = 2)) and the statistical uncertainty associated with the sequential ratio fitting procedure.

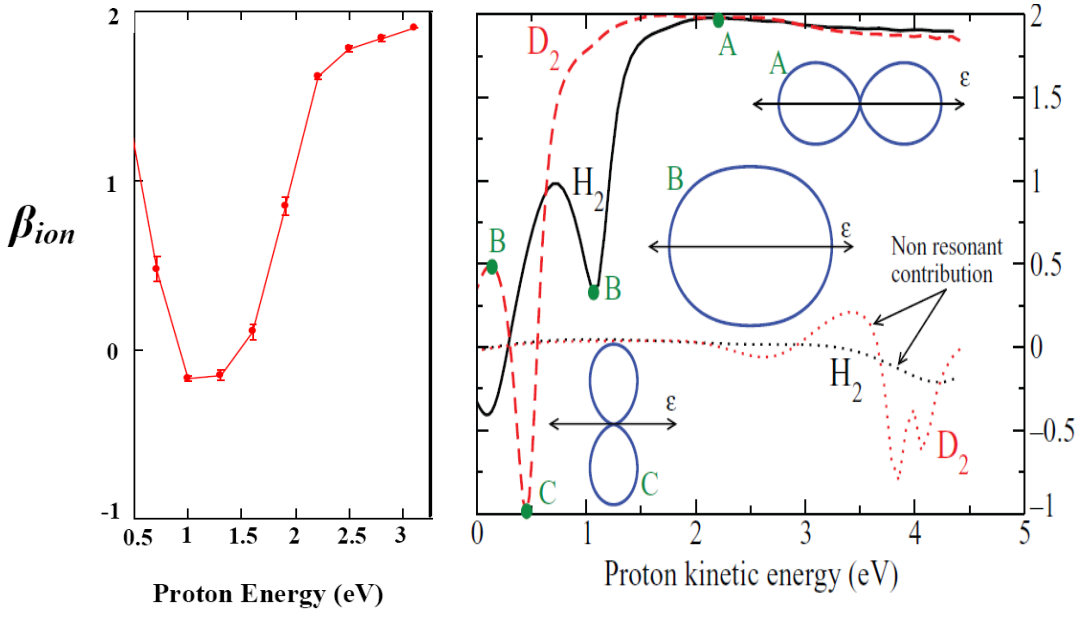

a) b)

Fig 5 t: a) Experimental observations of the β_{ion} $h\nu$ = 27eV as a function of proton energy (eV). Fig 5 s: b) Calculated ion asymmetry parameters with the results for H_2 are shown by full black [1].

Ion β measurements seen in Fig 5 t a, were made for at $h\nu$ = 27 eV parameter with the relative statistical uncertainty is shown in the smaller (red) error bars. With ions, the signal to background ratio is much higher than that for electrons where the background contribution is from low energy (metal scattered) electrons. While there is still background contribution from low energy ions, the detection efficiency improves significantly with higher energy ions (hence, smaller error bars > 2 eV in Fig 5 t a. The data analysis procedure is the same as that applied for electron β data, the *variation* of β_{ion} with proton energy E_k is found by *sequentially* performing a weighted least squares fit of the observed ratio of the $I_{ion}\left(\left(E_k \pm \Delta E_k\right), \beta_{E_k \pm \Delta E_k}, \theta\right) / I_{ion}\left(E_k, \beta_{E_k}, \theta\right)$ yield, where ΔE_k = 0.3 eV. The ratio of angular distributions β_{ion} was taken from the higher proton energy end, by calibrating the starting β_{ion} (E_k =3 eV) with the corresponding theoretical value. The experimental observations show a dip in β at ~ 1 eV proton energy as predicted in theory [1].

5.6.2 β_{ion} MEASUREMENTS - $h\nu = 33$ eV

Subsequent to the photoelectron β measurements at $h\nu$ = 33 eV, ion asymmetry parameter $\beta_{ion,}$ were measured at this photon energy. Preliminary experimental observations along with the theoretical calculations [1], are shown in Fig 5 u a) and b) respectively. Our observations are consistent with theory, we observe two closely spaces peaks in the proton energy region between 4.5 - 6 eV. Here again, the ratio of angular distributions β_{ion} was taken from the higher proton energy end, by calibrating the starting β_{ion} (E_k = 7.5 eV) with the corresponding theoretical value.

a)

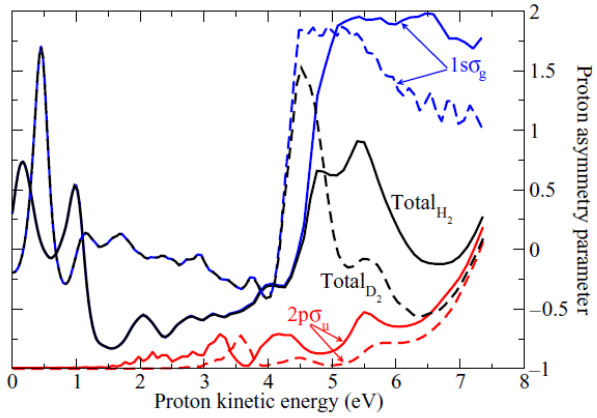

b)

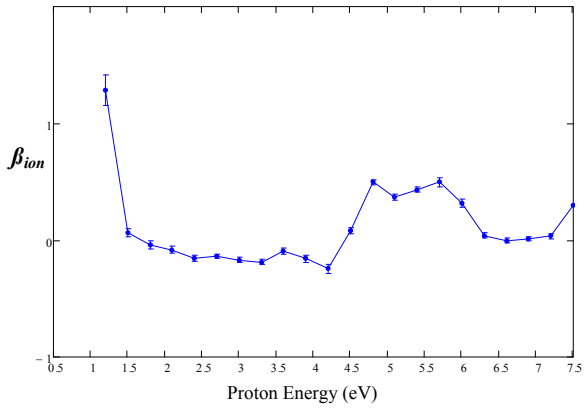

Fig 5 u: a) ionic asymmetry parameter as a function of the proton energy for H_2 (full lines) for $h\nu$ = 33 eV. The contribution from the first two ionization thresholds is also included: blue line, $1s\sigma_g$ contribution; red line, $2p\sigma_u$ contribution. b) Preliminary β_{ion} experimental observations for $h\nu$ = 33 eV as a function of proton energy (eV).

5.6.3 PRELIMINARY ION (PROTON) AND ELECTRON β MEASUREMENTS

Seen in Fig 5 v are preliminary β_{ion} measurements for $h\nu$ = 25, 29, 35 eV as a function of proton energy. At $h\nu \leq 27$ eV, the doubly excited states are expected to have limited contribution and one would expect to see slight or no oscillations in electron β. It can be seen in Fig 5 w that the electron β measurements for $h\nu \leq 27$ eV do not show any significant oscillations β. However, for $h\nu \geq 27$ eV, the doubly excited states are accessible and we expect to see oscillations in β. At $h\nu$ = 29 eV , the beginning of interference effects can be seen in Fig 5 w, as the electron β show oscillations between electron energy 5-9 eV. For $h\nu$ = 37 eV, we may switch off the Q_1 and Q_2 interferences. The results shown in Fig 5 v and 5 w are preliminary and the first set of measurements made at the above photon energies. In subsequent analysis, these results need to compared with *ab initio* calculations and further theoretical analysis is required at this point to understand the involvement of the doubly excited states for the specific photon energies.

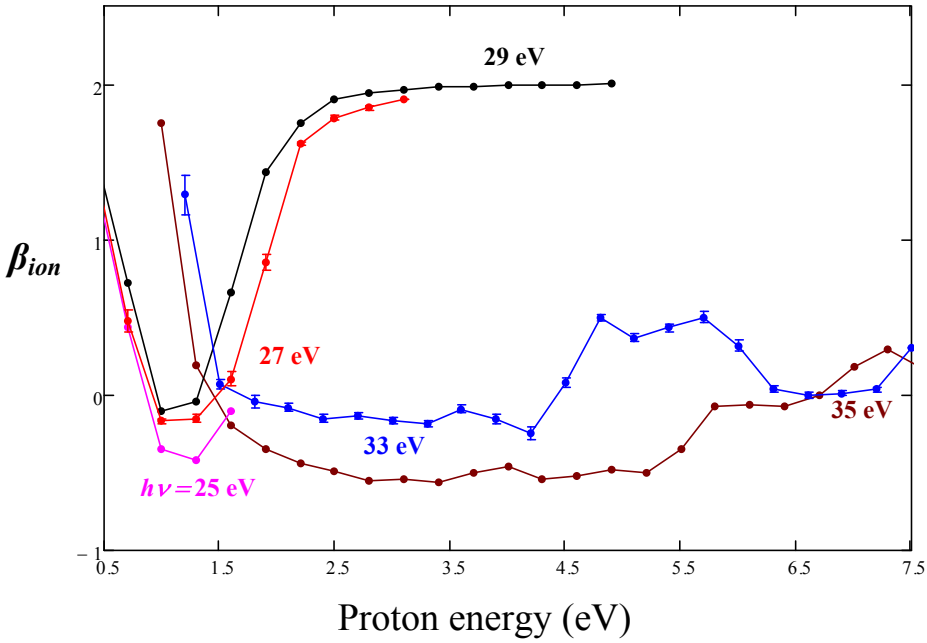

Fig 5 v: β_{ion} as a function of proton energy measured for various photon energies as shown in the plot. Also seen is the measured β_{ion} for $h\nu$ = 27, 33 eV with the statistical uncertainty.

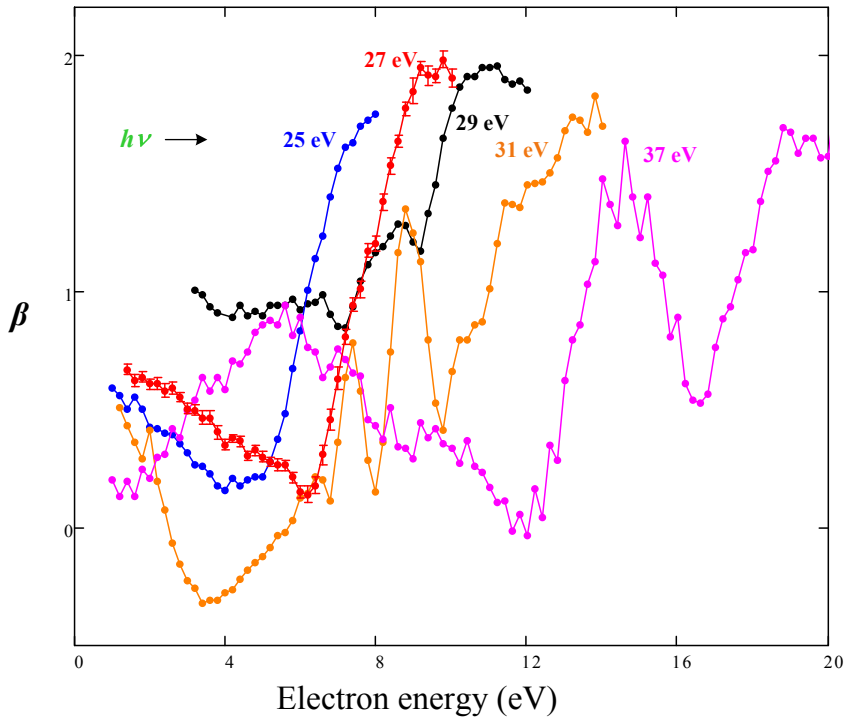

Fig 5 w: Electron β as a function of electron energy measured for various photon energies as shown in the plot. Also seen is the measured β for $h\upsilon$ = 27 eV with the statistical uncertainty.

5.7 CONCLUSION:

Large amplitude oscillations in the photoelectron asymmetry parameter, β, as a function of electron energy, for randomly oriented H_2 have been observed for the first time. β oscillations are in excellent agreement in (phase and frequency)with the results of recent close coupling calculations of Fernández and Martín [1]. To summarize our analysis, the observed oscillations at photon energies of 31, 33 and 35 eV are attributed to the coherent superposition of lowest $1Q_1\,^1\Sigma_u^+$ and $1Q_2\,^1\Pi_u$ doubly-excited states, where DPI occurs via two quantum mechanical routes that result in photoelectrons of same energy.

A simple model has been developed to explain the β oscillations. The change in the frequency of the oscillations with photon energy is directly related to the change in the difference in the inter-nuclear distances between the two semi-classical pathways, ΔR. The presence of such oscillations is predicted to be a general phenomenon in DPI. This phenomenon will not be unique to H_2. Similar oscillations in the beta parameter are expected whenever two autoionizing states decay at significantly different inter-nuclear distances.

Subsequent to our first study, β (electron/ion) measurements have been made at lower photon energy of 27 eV. The preliminary results are compared to theoretical predictions [1]. The key features predicted in theory are observed. At this photon energy, only the Q_1 doubly excited states of $^1\Sigma_u$ and $^1\Pi_u$ symmetry are accessible. Oscillations in electron β due to interference effects, for this photon energy theoretically predicted between 2 and 6 eV, are not observed. This could be due to background contributions from metal scattered electrons at lower energies that might have suppressed the oscillations. Also compared were β_{ion} measurements $h\upsilon$ = 33 eV, which are in excellent agreement with theory. Preliminary electron/ion β measurements for $h\upsilon$ = 25, 27, 29 and 37 eV, along with ion β measurements for $h\upsilon$ = 31 and 35 eV are also presented.

5.8 REFERENCES:

[1] Fernández J and Martín F 2009 *New J. Phys*. **11** 34 (2009)

[2] F Martín *et al* 2007 *Science* **315** 5812 629-633

[3] Sánchez I and Martín F 1997 *J Chem Phys* **106** 7720

[4] Reddish T J, Richmond G, Bagley G W, Wightman J P and Cvejanović S 1997 *Rev. Sci. Instrum*. **68** 2685-92

[5] Wightman J P Cvejanović S, Bagley G W and Reddish T J 1998 *J Elec Spec & Rel Phen* **95** 203

[6] Dehmer J L and Dill D 1978 *Phys Rev A* **18** 164

[7] Becker U and David A. Sherley 1996 VUV and Soft X-Ray Photoionization *Plenum Press* pp 138

[8] Toffoletto F, Leckey R C G, and Riley J D 1985 *Nucl. Instrum. Methods Phys. Res*. B **12** 282

[9] Wightman J P, Cvejanović S and Reddish T J 1998 *J. Phys. B: At. Mol. Phys.* **31** 1753-64

[10] Schmidt V 1997 Electron Spectrometry of Atoms using Synchrotron Radiation *Cambridge University Press* pp 41-45, 364-366.

[11] Lafosse A, Lebech M, Brenot J C, Guyon P M, Spielberger L, Jagutzki O, Houver J C and Dowek D 2003 *J. Phys. B: At. Mol. Phys.* **36** 4683

[12] Hikosaka Y and Eland J H D 2003 *J Elec Spec & Rel Phen* **113** 77

[13] Parr A C, Hardis J.E, Southworth S, Feigerle C, Ferrett T, and Holland D.M.P.1988 *Phys. Rev. A* **37** 437

[14] Dowek D, Pérez-Torres J-F, Picard Y J, Billaud P, Elkharrat C, Houver J C, Sanz-Vicario J L and Martín F 2010 *Phys. Rev. Lett*. **104** 233003

[15] Ito K, Hall R I and Ukai M 1996 *J. Chem. Phys.* **104** 21

[16] Martín F 1999 *J. Phys. B: At. Mol. Phys.* **32** R197–231

SUMMARY AND CONCLUSION

Photoionization experiments in this thesis were performed using linearly polarized synchrotron radiation. The toroidal spectrometer was successfully commissioned at the Canadian Light Source (CLS), a third generation synchrotron facility. The spectrometer was aligned with the VLS PGM beamline that operated from an undulator source. Standard set of equations that characterize linearly polarized light, that are then applied to measuring angular distribution for photoionization processes are reviewed. Design details of the spectrometer that consists of two analyzers based on toroidal geometry along with focusing properties of toroidal analyzers are presented. The multi coincidence capability of the spectrometer and various other operational modes are reviewed. Data acquisition method for each mode is outlined along with non-trivial details on data acquisition and data processing for coincidence experiments.

For the first time, the spectrometer was employed to perform Threshold Photoelectron Photoion Coincidence (TPEPICO) technique. By energy width analysis of vibrational peaks of O_2^+ $c^4\Sigma_u^-$ state (ν = 0, 1) and taking ratio of the photoion angular distribution of $O^+(^4S)$ produced from DPI , we obtain lifetimes $\tau_1 = 6.0 \pm 0.3\ x10^{-14}$ s and a lower limit on τ_0 of $\approx 1\ x10^{-12}$ s. The obtained results are in broad agreement with other experimental studies using different methods. We find the inherent anisotropic β parameter $\beta_{O^+} = 0.40 \pm 0.05$, for this ionic state, which is significantly at variance with the predicted value of ≥ 1.6.

Dissociative photoionisation (DPI) of randomly oriented H_2 molecules has been studied using linearly polarized synchrotron radiation at selected photon energies of 31, 33 and 35 eV. The phase and frequency of these β oscillations are in excellent agreement with the results of recent close coupling calculations (Fernández and Martín 2009 *New J. Phys*. **11** 34). It is shown that the oscillations are the signature of interferences between the $1Q_1\,^1\Sigma_u^+$ and $1Q_2\,^1\Pi_u$ doubly-excited states decaying at different inter-nuclear distances. The oscillations thus provide information about the classical paths followed by the nuclei. The presence of such oscillations is predicted to be a general phenomenon in

DPI. A simple semi-classical model that captures the essence of both the experimental observations and the results of full *ab initio* calculations are given. The model links the *electron* angular distributions with the *nuclear* motion of the dissociating diatomic molecule.

Subsequently, ion/proton angular distributions were measured for the photon energies of 25, 27, 29, 33 and 35 eV. The proton angular distributions for 33 and 27 eV as a function of proton energy were compared to the theoretical predictions. The key features in the predicted angular distributions were observed. Also measured are electron angular distributions at photon energies below and above 31- 35 eV to gain a better understanding of the role of interference between the Q_n doubly excited states.

****

APPENDIX

A.1 DATA ACQUISITION SOFTWARE

A.1.1 INTRODUCTION

A.1.2 MAIN PROGRAM

A.1.3 CAMAC LIBRARY

A.1.4 TEST PROGRAMS

A.1.5 SOFTWARE UPDATES

A.2 PRELIMINARY PHOTOIONIZATION STUDIES OF KRYPTON

A.2.1. INTRODUCTION

A.2.2. POST COLLISION INTERACTION (PCI)

A.2.3. THRESHOLD PHOTOELECTRON SPECTROSCOPY OF Kr

A.2.4. CONSTANT KINETIC ENERGY SPECTRA (CKES) IN THE VICINITY OF Kr 3d EDGES

A.2.5. CONCLUSION

A.3 REFERENCES

A.1 DATA ACQUISITION SOFTWARE

A.1.1 INTRODUCTION

This section is dedicated to information regarding the various software programs used for data acquisition. The software platforms on which these were originally written and details on the various upgrades made in the past are given.

A.1.2 MAIN PROGRAM (PFSPEC)

The main program for data acquisition is a DOS based, written under Prospero Fortran. The program has been written and developed by Reddish, Wightman and Bagley. Two kinds of libraries with sub routines are linked to the program. Low level sub routines are simple programs written to perform simple commands to the CAMAC hardware, like reading or writing a byte of data. High level sub routines are complex programs written to call one or more routine to perform specific tasks. The program when executed initializes the CAMAC hardware, which means that the memory in the modules are cleared out and the modules are ready to receive the necessary commands. The user is allowed to choose from possible modes for data acquisition. More details can be found in Wightman [1]. The modes of data acquisition used in this thesis are described below:

Type 1: Dual Photoelectron Spectrum
Type 2: Coincidence Mode

Type 1: Dual Photoelectron Spectrum

Here, the photon energy is fixed and the toroidal analyzer energy is scanned. Each of the analyzers are connected to dedicated 12-bit DAC (Digital-to Analogue Convertor) units. The energy scan conditions are set by specifying the total number of points, step size between each point for each of the analyzer. The start-stop, step size can be specified separately for each detector and the directory path to save the output file is typed in before the commencement of data accumulation. A CAMAC dual counter

records the number of counts from both the detectors for a user specified accumulation time per point and another counter records the accumulated photon flux. The analyzer can be used simultaneously for a dual PES, but can also be used for a single PES by rewiring only a single DAC unit to the required analyzer. At the completion of a scan, the first display is the counts accumulated from the 100º analyzer, the second from the 180º analyzer and the third the photon flux. One could freeze the screen to look at one of the displays by hitting the pause-break key.

Each data file has a ".dat" file containing the data and a ".inf" information file. The .dat file consists of 4 arrays of floating-point numbers that are stored in memory. The 4 columns in the data file correspond to photon energy (PC) (the column is zero in this case as the photon energy is constant), photon flux (EC), 100º detector counts (RC) and 180º detector counts (BC). The .inf file contains the information for that particular run, such as photon energy, analyzer energy, etc. Any Type 1 data file can be read into the program and be displayed if required.

Type 2: Coincidence Mode:

The counts for a specified Time to Amplitude Convertor (TAC) window are accumulated, each count indicating a valid TAC output (i.e. a 'coincidence') in correspondence to the (*x, y*) positional information within the specified time window. The photon energy is fixed and the analyzer energies are fixed in accordance to kinematics of the desired experiment. Five ADCs are used to collect the positional information and timing information (TAC spectrum). Low level sub routines written into the software enable the performance of LAM (CAMAC protocol – 'Look At Me') tests for the Type 2 spectra. Hence, one can ensure synchronization between the 5 ADCs by checking if they produce LAMs at the same time.

In the coincidence mode, one can chose the number of files, number of buffers per file, where each buffer represents 256 coincidence events and the directory path for the output file. The screen while accumulating data shows a small display window that shows

the live TAC spectrum as counts are being accumulated. There should be a prominent TAC peak signifying a "true" coincidence event and the window provides a visual check. To abort a scan in this program one needs to press ctrl + esc keys simultaneously.

As mentioned for Type 1 spectra, the data files outputted are *.dat, *.inf files and in addition to these a master file with extension "*.mas" and a "*.tac" is created as well. The *.dat file for Type 2 spectra consists of 6 columns and the format is (J, X1(J), Y1(J), X2(J), Y2(J), T(J)) where J is each buffer with J= 1..256. The *.tac file has 2 arrays, the format being (J, TAC(J)). At the start of the spectrum the *.dat and *.tac file is kept open and at the end of the run the files are closed and the filename (includes number of points) is written to the master file and then the process is repeated for consequent file. Each master file comprises of a specified number of files and the number of buffers for each file can be chosen. At the end of collecting the specified number of files, the master file is closed.

A.1.3 CAMAC LIBRARY

Low level routines have been written in the CAMAC library that provide interface between the main program and the CAMAC hardware. The routines that can be performed are:

- Read, write bytes of data to CAMAC controller module via singular board
- CAMAC initialization , read and write data
- Module specific control
- Perform LAM tests on modules

MAIN LIBRARY:

This library contains routines that enable the following:

- Control DAC modules ; essential in controlling the analyzer detection energies
- Screen display options i.e. user interface options, program options and processing user inputs
- Read and Write data in the specified formats on the hard disk
- Graphic routines for displaying data

It should be noted that the routines that control hardware, such as DAC, are all low-level routines from the CAMAC library.

A.1.4 TEST PROGRAMS:

Various test programs have been written to check the CAMAC interface for troubleshooting purposes. The most commonly used in this thesis work are:

Kitcar:

This is a Delphi based program. A 24 bit LED register is dedicated to check the write operation on a given CAMAC slot. The module can be inserted in any one of the 24 normal stations. Each LED light on the module corresponds to a data bit and when a data is written to the module, each LED light is turned on and off in succession.

TS1S2:

S1 and S2 pulses can be sent to the CAMAC crate, initialize all CAMAC commands. The timing and amplitude of the pulses can be checked with an oscilloscope from the back-plane.

TestIt:

Module dedicated and operation specific testing can be done using this Delphi program. A module number N is specified directing the program to address a module in a specific CAMAC slot, a function F and sub-address A is typed in, Q and X values are returned indicating if the operation was successfully executed [N, F, A, Q and X are all standard CAMAC protocol].

A.1.5 SOFTWARE UPDATES:

The software written earlier in FORTRAN using a DOS based compiler was upgraded to 16 bit Delphi 1.0 compiled within Windows 3.1. However, with the rapid growth of the Operating System, it was necessary to find compatibility within the latest

OS of that time, Windows 95. Although the 16-bit Delphi version was functioning in a Win 95 environment, the necessity of an upgrade to a 32-bit Delphi compiler was inevitable in order to take full advantage of the latest version of the 32 bit Windows. Specific details on the software update can be found in Wightman [1]. The following software programs were used in this thesis work:

SpecUtils ;

This is a 32 bit Deplhi 1.0 version program written by S.A. Collins. This program was used in the initial phase of an experiment. The program has 3 options.

Tab 1: Spectrometer Angles and Angular Distributions:

This option enables visual display of the spectrometer from the observer's point of view (i.e. looking towards the incoming photon beam). The smaller toroid (100º) is represented in red and the larger toroid (180º) is represented in blue. The horizontal line represents the plane of polarization. This page has the option of selecting the orientation for one of the analyzers by specifying the angle for the centre of the analyzer (see Fig A a). The orientation of the analyzer with respect to the other analyzer and the photon beam axis is then simulated by the program. The analyzers can then be physically rotated around the photon beam axis to suit the experimental needs. The positions for the mechanical stops that have been built into the spectrometer are included in the program. The software prompts a warning if a specific geometry is not possible. This option has been a useful resource for a visual check on the mutual orientation of the analyzers.

Tab 2: Analyzer Pass Energies and Resolution

Here, one can enter the analyzer pass energy to determine the energy resolution as per the pre-programmed formula, given in Chapter 2, Eqn 2.3. By entering the pass energy, the program calculates the potentials to be applied to the outer toroid (OT), inner toroid (IT), delta toroid (DelT), the corrective hoops R1, R2, R3, R4 in order to attain the required energy resolution, as seen in Fig A b.

Tab 3: Experimental Information and beta calculator:

Values for the β parameters for He^+ (n=2) single ionization threshold at various electron energies can be obtained from this option. The theoretical β values provides a consistency check on the angular distributions and also if the detectors have been wired accurately.

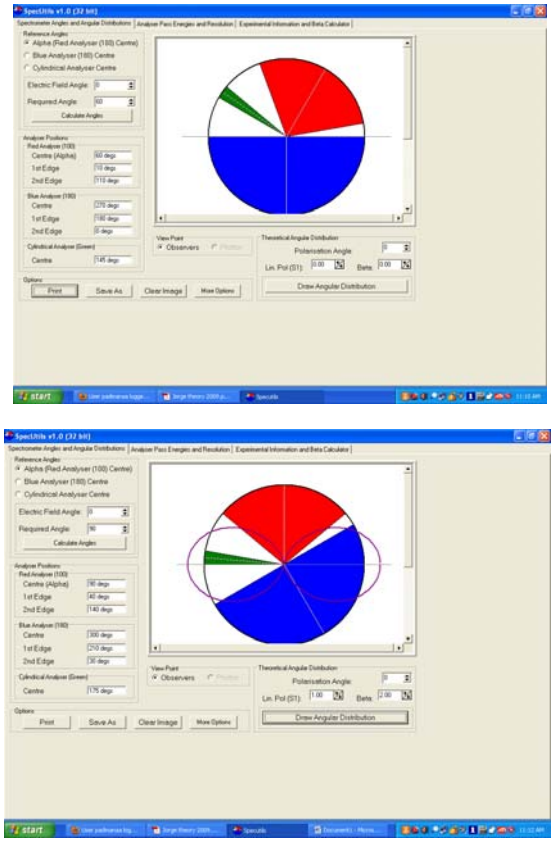

Fig A a: Screen shot (Top) shows the 100º Analyzer (in Red) centre at 60º to the horizontal light polarization axis and mutual orientation of the 180º Analyzer (in Blue) and the hypodermic needle as seen looking onwards to the incoming photon beam. The second screen shot (Bottom) shows the angular distribution for a linear polarization (S_1= 1) for a given beta of two. Here the mutual orientation is displayed with the Red Analyzer chosen to be at 90 º.

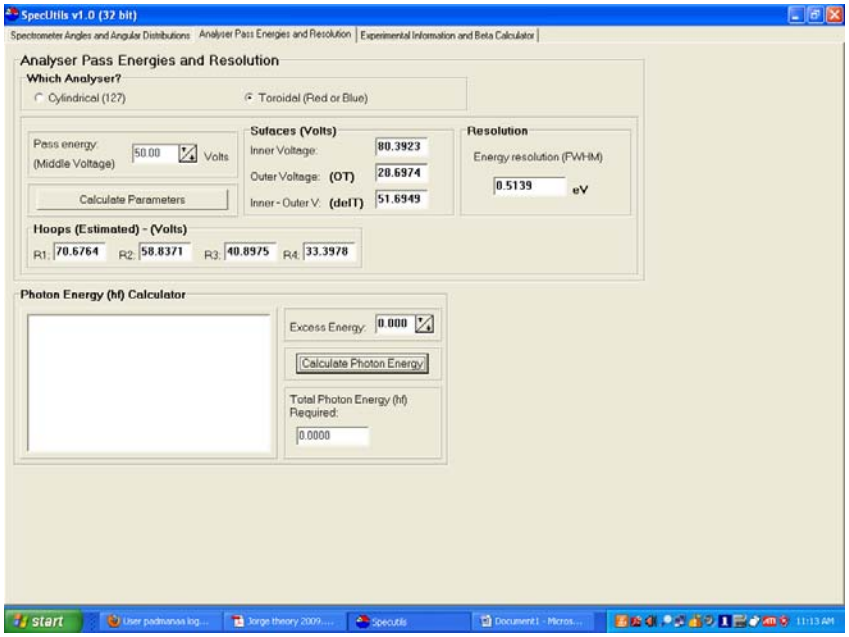

Fig A b: Screen shot of Tab 2 of the SpecUtils program. The theoretical electrostatic potentials for the toroidal surfaces and hoops is calculated and displayed for a particular toroidal pass energy given by the user.

Tune16:

This 16 bit Delphi 1.0 program was written by J. P. Wighman. The program is used while tuning the spectrometer. The software enables one to see live positional (*x,y*) images on each detector as counts are being accumulated. One can chose which detector one wants to view, for a user preset number of buffers. The live images also provide a check for the presence of the mechanical stops or "teeth", which should be 160º apart. This is seen as minima in the "graph" option and as zero counts in the teeth region in the "image" option. Any stretching in the angular scale can be checked for and can be improvised by further tuning the electron optics of the analyzer lens.

Tab 1 –Image:

The first tab "image" displays the x-y data in polar coordinates, allows one to correct for the radial filters and improvise on the spectrometer tuning for optimum image results. Each buffer accumulated corresponds to 256 counts from the ADC module. As the counts are being accumulated the number of "good" buffers and "bad" buffers are updated as well. A "bad" buffers refers to an invalid LAM and that particular buffer is discarded. The position computers have an image gating option via hardware masking to restrict the images to narrow angular range. This option was used while tuning the spectrometer for threshold electrons and the live visual display provided by the software assures one of limits of the selected angular range. To abort a run ALT + F10 keys need to be pressed simultaneously.

Tab 2-graph:

This displays the accumulated counts against the angle according to the chosen detector. Number of buffers to be accumulated can be chosen here as well, there is an option to enter the following parameters: spectrometer angle, polarization, scale, beta (if known). For instance, while recording an image for the He^+ (n=1) single ionization threshold, the beta value is well known to be; $\beta = 2$. So when the counts are being accumulated the predicted beta parameter is plotted on top of the real plot. The images can be saved to a chosen directory path as "*.dat" file (MathCAD friendly). These images can then be used as calibration images for data processing.

A.2. PRELIMINARY PHOTOIONIZATION STUDIES OF KRYPTON

A.2.1 INTRODUCTION

The focus of this study was to investigate the angular dependence on Post Collisional Interaction (PCI) [2] between Auger electrons and threshold electrons in Kr. To study the PCI effect on angular distribution of the Auger electrons arising from the

$3d_{3/2}$ core hole state, coincidence measurements were made at the threshold peak and the corresponding PCI tail with an isolated Auger electron. Results from spectroscopic measurements of Kr i.e Threshold Photoelectron Spectrum (TPES) and Constant Kinetic Energy Spectrum (CKES) of Kr which were necessary for energy calibration are also presented in this section.

A.2.2 POST COLLISION INTERACTION (PCI)

During an inner shell photoionization process, a core electron or an inner shell electron is targeted and when a core electron is removed, the vacancy that is left behind may be filled by an electron from a higher energy level. The energy resulting from this transition may be transferred to another electron, which is ejected from the atom. This second ejected electron from an outer shell is called an Auger electron**.** The sample process equation is for the inner shell photoionization of an atom X leading to the emission of a photoelectron e_p and subsequently an Auger electron e_A. The atom then ends up in a doubly charged ionic state.

$$h\nu + X \rightarrow X^{+} + e_p \rightarrow X^{2+} + e_P + e_A$$

When photon energy comes close to the threshold value for the ejection of an inner-shell electron, the subsequent Auger decay may be influenced by the presence of slowly receding photoelectron. The resulting interaction between the escaping electrons is termed the post collisional interaction (PCI) [3]. In this kind of electron correlation effect between the two outgoing photoelectrons close to the threshold, the slow photoelectron can shield the doubly charged ion such that the faster Auger electron gains energy and the slower photoelectron loses the same amount of energy. This energy exchange can have two consequences. First, the resulting PCI energy distribution for the emitted electrons is no longer described by a Lorentzian line shape. Instead the energy distribution is asymmetric and broadened and shifted in energy. Hence, the Auger electrons that gain energy in a PCI effect, show a shift in energy in an observed Auger-Threshold photoelectron coincidence spectrum. Second the energy exchange may be so large that

the slow photoelectron can be captured in a bound orbital of the remaining ion (called the shake down effect). The former is also true for threshold electrons and the PCI effect in this regard is demonstrated in the next section on threshold photoelectron spectroscopy (TPES) in vicinity of 3d edges of Kr.

Preliminary results obtained to study the effect of PCI in angular distributions of Auger electrons associated with the $3d_{3/2}$ core hole state, show no significant change with position within the characteristic PCI 'tail'. Further experimental work is needed in this area

A.2.3 THRESHOLD PHOTOELECTRON SPECTROSCOPY OF Kr

The smaller toroidal analyzer was tuned to detect threshold electrons (near zero < 5 meV) using the field penetration technique [4]. In order to calibrate the threshold detection efficiency, the toroid was first tuned to detect helium threshold electrons. The measured energy resolution in the threshold channel was 3.8 meV (FWHM) using He^+ (n = 1) at 24.586 eV, (see Fig A c). The photon beam resolution was estimated as 1.8 meV (FWHM) by fitting the rising edge of the He^+ (n = 1) TPES peak to a Lorenzian curve.

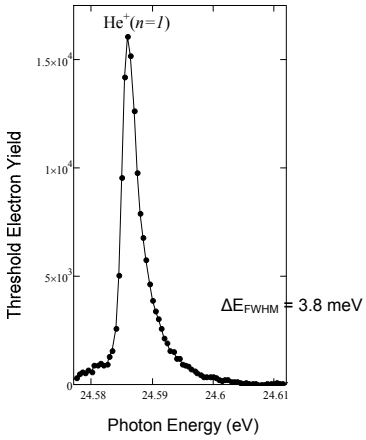

Fig A c: Yield of threshold electrons against photon energy at He^+ (n = 1); Energy resolution at FWHM measured to be 3.8 meV at 0.5 meV/channel.

Hikosaka *et al* [6], in their Auger electron-threshold electron coincidence studies of Kr, have presented results that show the effect of PCI. Their TPES of Kr in the vicinity

of Kr 3d edges shows peaks that are broadened and PCI shifted. Due to the post-collision interaction, the maxima corresponding to the $3d_{3/2}$ and $3d_{5/2}$ threshold electrons appear at higher photon energies than the threshold energies. The binding energies of the $3d_{5/2}$ and $3d_{3/2}$ electrons are given to be 93.788 eV and 95.038 eV from the energy levels of the converging Rydberg states by King *et al* [5], respectively. However it is seen in the TPES shown in Fig A d that the yield of threshold electrons shows the corresponding maxima for $3d_{5/2}$ and $3d_{3/2}$ threshold electrons at $h\nu$ = 94.02 ± 0.03 and 95.29 ± 0.03 eV. Moreover, the tail on each peak on the high energy side is a signature of a PCI effect. Thus, the peak shifts and tails show the presence of PCI effects in this spectrum. Fig A d shows the TPES performed in this study in the vicinity of the Kr 3d edge; $h\nu$ = 90- 96 eV. Our observations are in agreement to those by Hikosaka *et al* and we also observe the PC shifted peaks of the $3d_{5/2}$ and $3d_{3/2}$ threshold electrons at $h\nu$ = 94.02 and 95.29 eV.

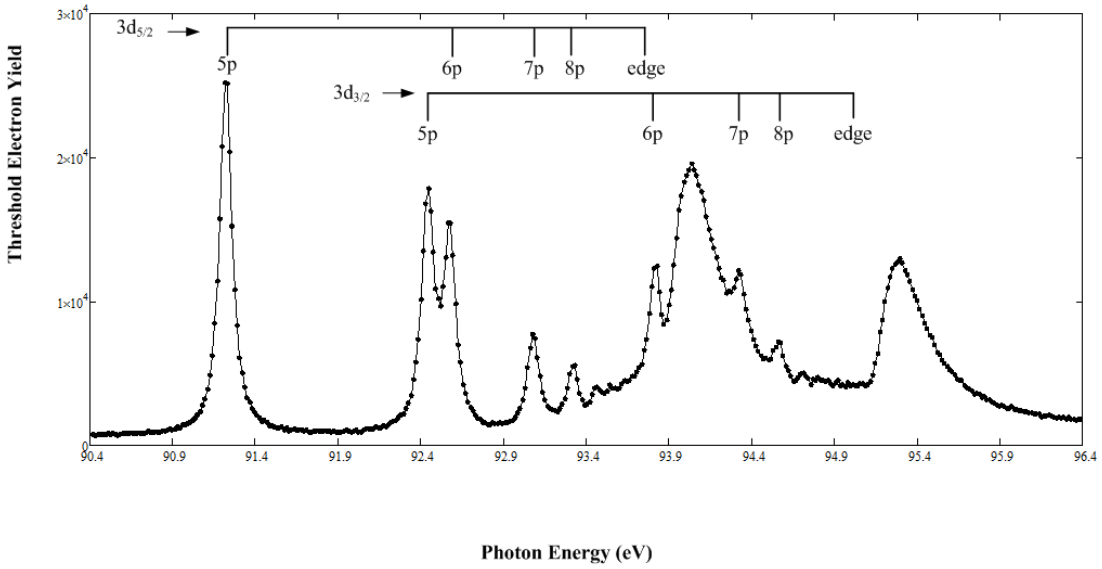

Fig A d: TPES of Kr in the vicinity of the 3d edge. The spectrum shows both the $3d_{3/2}$ and $3d_{5/2}$ core hole states along with the corresponding Rydberg states.

A.2.4 CONSTANT KINETIC ENERGY SPECTRA (CKES) IN THE VICINITY OF Kr 3d EDGES

CKES taken during photoionization studies of Kr are presented in this section. In this mode of data acquisition, the detection energy of Auger electron analyzer was fixed and the photon energy was scanned across the region of interest. Hence, the final electron energy is the same for all photon energies and the yield of Auger electrons of specific energy is measured across the photon energy region. In this case, CKES was taken at Auger lines associated with the $3d_{3/2}$ and $3d_{5/2}$ core hole states. Figs A e, A f and A g shows the accumulated CKES at various Auger energies for these two states, with the TPES in the background. The photon energy was scanned from 90.5 to 96 eV. The table below shows the energies at which CKES was performed and compares the values to previous experimental studies of Aksela *et al* [7] and Jauhiainen *et al*[8].

TABLE A.1: A table comparing the observed Auger energies for $3d_{3/2}$ and $3d_{5/2}$ core hole states with previous experimental studies.

Energy	This work(eV)	Aksela *et al* [16] (eV)	Jauhiainen *et al* [17] *(*eV)
$3d_{3/2}$ Auger Energies	**32.50**	32.35	32.32
	39.08	39.08	39.11
	42.25	42.32	42.33
	52.64	52.58	
$3d_{5/2}$ Auger Energies	**37.78**	37.84	37.74
	51.22	51.33	

CKES taken at Auger electron energies 32.5, 39.08, 42.25 and 52.64 eV has been presented in Fig A e and A f. The CKES is presented on a comparative scale with the TPES in the background. CKES for all the Auger energies belonging to this core hole state, form peaks at the *n*p Rydberg states belonging to the $3d^{-1}{}_{3/2}$ core hole. CKES taken at Auger electron energies 37.78 eV and 51.22 eV that belong to the $3d_{5/2}$ core hole state are presented in Fig A g.

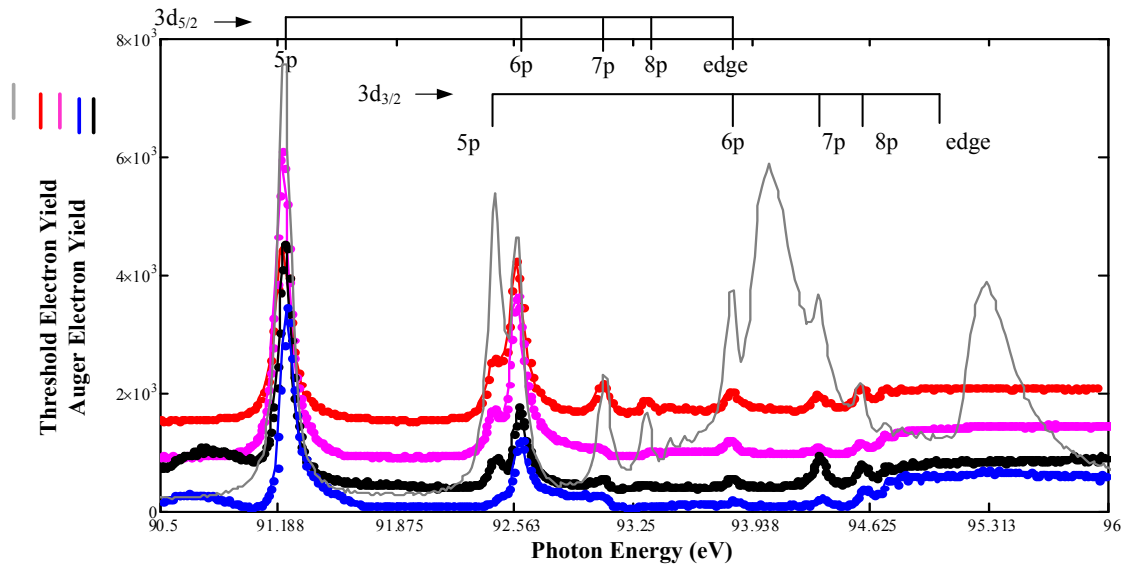

Fig A e: CKES of Auger electron energies 32.5 eV (red), 39.08 eV (pink) ,42.25 eV (black) and 52.64 eV (blue) that belong to the $3d_{3/2}$ core hole TPES with labeled peaks of the *n*p Rydberg states belonging to both $3d_{3/2}$ and $3d_{5/2}$ core hole states is shown in the background.

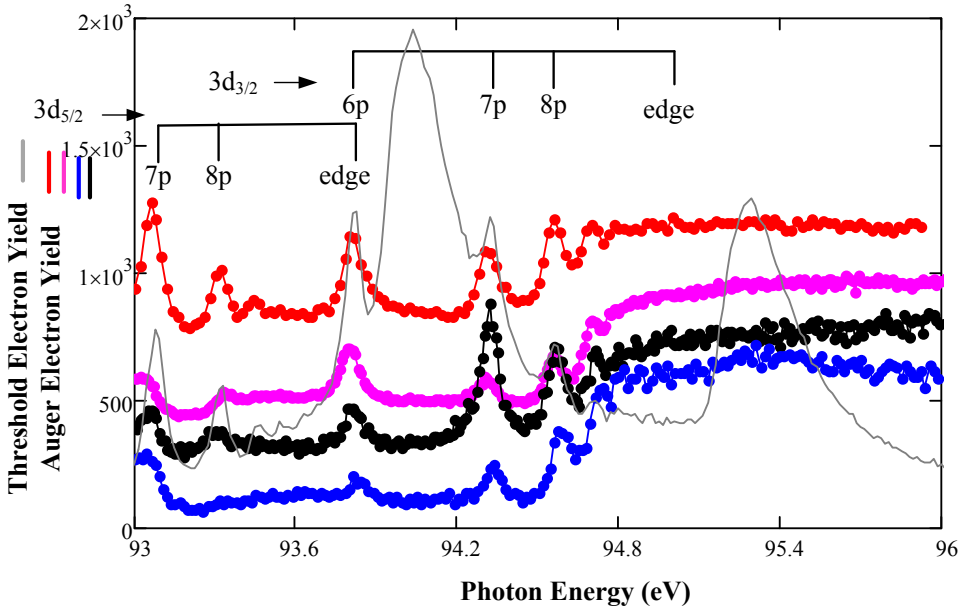

Fig A f: Zoomed in CKES of Auger electron energies 32.5 eV (red), 39.08 eV (pink), 42.25 eV (black) and 52.64 eV (blue) that belong to the $3d_{3/2}$ core hole. TPES with labeled peaks of the *n*p Rydberg states belonging to both $3d_{3/2}$ and $3d_{5/2}$ core hole states is shown in the background.

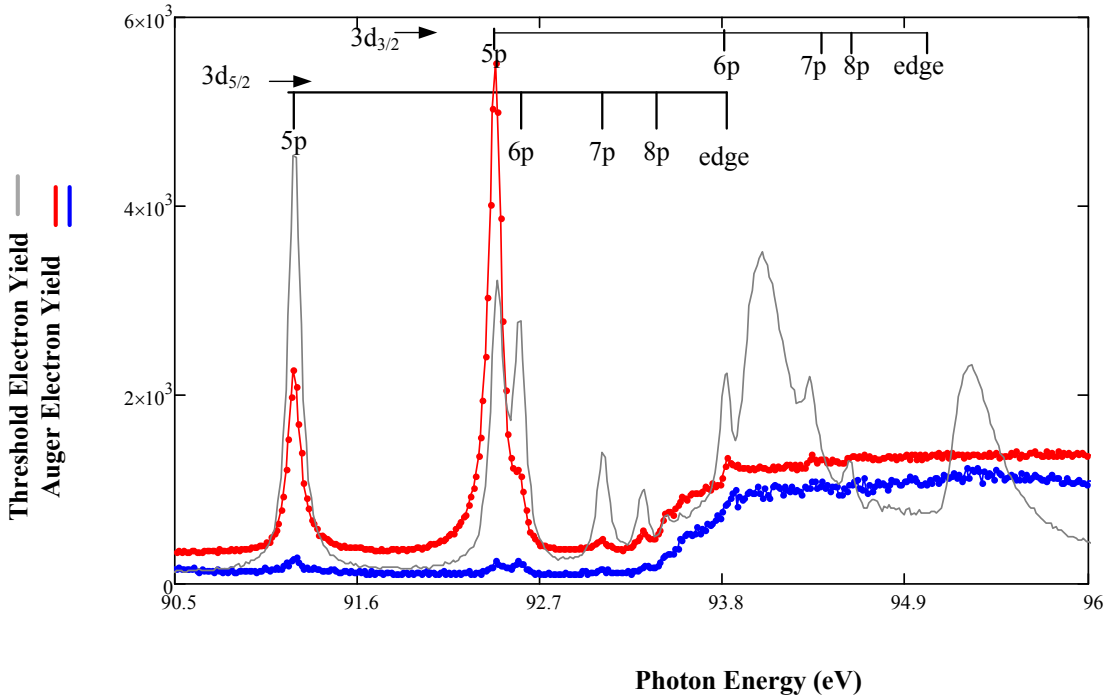

Fig A g: CKES of Auger electron energies 37.78 eV (red) and 51.22 eV (blue) that belong to the $3d_{5/2}$ core hole. TPES with labeled peaks of the *n*p Rydberg states belonging to both $3d_{3/2}$ and $3d_{5/2}$ core hole states is shown in the background.

A.2.5 CONCLUSION:

The angular distributions of Auger electrons in coincidence with threshold photoelectrons in a PCI context have been studied for the first time, to our knowledge. However, no significant PCI effects are observed in the angular distributions. However, due to preliminary nature of our study, further work is needed for a conclusive result to be presented. It is possible that, since the difference in the energy of the outgoing electrons is large, PCI does not play a role in the angular distribution of the Auger electrons measured at these two different points in photon energy. Spectroscopic results undertaken during the photoionization study of Kr are presented in this section. TPES of Kr in the vicinity of Kr 3d edges and CKES of Auger electrons associated with $3d_{3/2}$ and $3d_{5/2}$ core hole states are also presented.

A.3. REFERENCES:

[1] Wightman PhD thesis 2002 The University of Newcastle Upon Tyne

[2] Kuchiev M Yu and Sheinerman S A 1989 *Sov. Phys.—Usp.* **32** 569

[3] Schmidt V 1997Electron Spectrometry of Atoms using Synchrotron Radiation *Cambridge University Press* pp 152

[4] Cvejanović S and Read F H 1974 *J. Phys. B: At. Mol. Phys.* **7** 1180-92

[5] King *et al* J. Phys. B: Atom. Molec. Phys., Vol. 10, No. 12, 1977

[6] Hikosaka *et al Meas. Sci. Technol*. **11** (2000) 1697–1702

[7] Aksela H, Aksela S, and Pulkkinen H 1984 *Phys. Rev. A* **30** 2456-61

[8] J Jauhiainen, Aksela H, Aksela S, A Kivimäki A, Sairanen O-P , Nõmmiste E and Végh J 1995 *J Phys. B: At. Mol. Opt. Phys.* **28** 3831-3843

VITA AUCTORIS

I was born in Bangalore, India during the year of 1979. I graduated from Bangalore University in 2000 with a Bachelors degree in Physics, Math and Electronics. I then pursued a Master's degree in Physics at Pittsburg State University, Pittsburg, Kansas. I graduated in December 2005. I accepted the PhD program in Physics at the University of Windsor, Windsor ON in September 2007. My research emphasis has been on experimental atomic and molecular physics in collaboration with Canadian Light Source (CLS), Saskatoon.